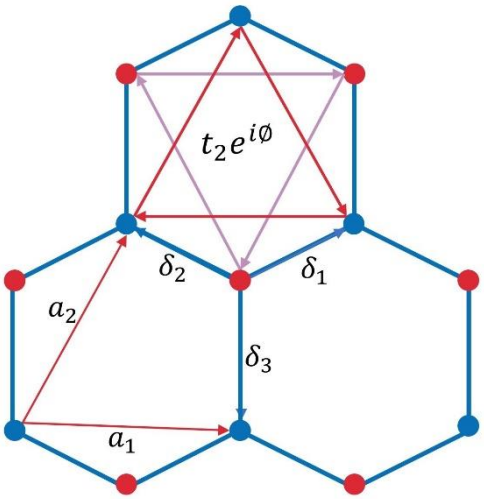

Localization properties across quasi-periodicity induced topological transitions in Chern insulators

Tiago Dias Souto Gonçalves
Mestrado em Física
Departamento de Física e Astronomia
2022

Orientador
Eduardo Filipe Vieira de Castro, FCUP

Coorientador
Pedro José Gonçalves Ribeiro, Instituto Superior Técnico - U. Lisboa


U.PORTO
FACULDADE DE CIÊNCIAS
UNIVERSIDADE DO PORTO

Declaração de Honra

Eu, Tiago Dias Souto Gonçalves, inscrito no Mestrado em Física da Faculdade de Ciências da Universidade do Porto declaro, nos termos do disposto na alínea a) do artigo 14.º do Código Ético de Conduta Académica da U.Porto, que o conteúdo da presente dissertação reflete as perspetivas, o trabalho de investigação e as minhas interpretações no momento da sua entrega.

Ao entregar esta dissertação, declaro, ainda, que a mesma é resultado do meu próprio trabalho de investigação e contém contributos que não foram utilizados previamente noutros trabalhos apresentados a esta ou outra instituição.

Mais declaro que todas as referências a outros autores respeitam escrupulosamente as regras da atribuição, encontrando-se devidamente citadas no corpo do texto e identificadas na secção de referências bibliográficas. Não são divulgados na presente dissertação quaisquer conteúdos cuja reprodução esteja vedada por direitos de autor.

Tenho consciência de que a prática de plágio e auto-plágio constitui um ilícito académico.

Tiago Dias Souto Gonçalves

Porto, 30 de setembro de 2022

Universidade do Porto

Faculdade de Ciências

Mestrado em Física

Localization properties across quasi-periodicity induced topological transitions in Chern insulators

Tiago Dias Souto Gonçalves

Supervisors

Prof. Dr. Eduardo Vieira Castro

Prof. Dr. Pedro José Gonçalves Ribeiro

A thesis submitted in fulfilment of the requirements for the degree of Master of Science

at

Departamento de Física e Astronomia

Porto, September of 2022

[This page was intentionally left blank]

The way that you can follow isn't the true eternal way.
A name that you speak, isn't its true name.
The unnamable is the eternally real.

-Daode Jing

Acknowledgements

This document is the culmination of an academic and scientific journey encompassing the last 5 years of my life that was only made possible by the presence of the people who were a part of it.

Firstly, it is imperative to thank my supervisor, Prof. Eduardo Castro, with whom I have worked over the past 3 years and who has given me the space and opportunities to enlarge my academic curriculum. To my co-supervisor, Prof. Pedro Ribeiro, a heartfelt thank you for the interesting and fruitful conversations. Our weekly meetings, along with Prof. Bruno Amorim and Miguel Gonçalves, were the compass that guided this work to fruition, and thus my most profound gratitude is also extended to them, for all the advice and encouragement.

To all those who have contributed to my work with insightful discussions and helpful explanations, be it in the Summer Schools organized by QM@PT, or in the university hallways, a part of this work is also yours.

A most sincere acknowledgement is to be given to all those with whom I have shared my time outside university work, and who didn't hesitate to enjoy a sunny summer afternoon in good company. In particular, to Manex and David, for always providing laughter, friendship, and for helping me achieve my goals. To Alex, Carlos, Baa, David, and Lemos, for being such fun house-mates. To Ana Cacho and Bruna Torta, for always keeping me grounded in the trying times.

Above all, to my friends from home, who were there before I set foot in this path. To Sueca, who trod it alongside me. And to all of them for being there at the end.

I would also like to thank my family, for being ever present, especially my mother, Piedade, my father, Carlos, and my eternal companion, Afonso. I owe them a debt bigger than life itself.

Last, but definitely no least, a very special thanks to Patrícia, for the unwavering support, care, and love offered unconditionally and without reserves, and for making the past 3 years more joyful and complete.

[This page was intentionally left blank]

Abstract

In this thesis we explored the interplay between quasi-disorder, topology and localization properties. To this effect, we studied two models subject to an incommensurate potential: the Haldane model and the model on a square lattice. We identified a plethora of topological phase transitions and characterized them based on spectral and localization properties, by using a wealth of numerical methods, such as the kernel polynomial method (KPM), level spacing statistics (LSS) and inverse participation ratio (IPR) analysis. These transitions proved to exhibit varying natures, concerning the way these properties change in the vicinity of the topological transitions. Additionally, we found phases that show critical edge gap states. Along these findings, we discovered in these two systems re-entrant behaviour, where a topological phase is induced by increasing the quasi-disorder strength.

[This page was intentionally left blank]

Resumo

Nesta tese exploramos o efeito recíproco entre quase-desordem, topologia e propriedades de localização. Para este efeito, estudámos dois modelos sujeitos a um potencial incomensurável: o modelo de Haldane e o modelo numa rede quadrada. Identificámos uma plétora de transições de fase topológicas que foram caracterizadas com base em propriedades espetrais e de localização, usando um conjunto diverso de métodos númericos, como o kernel polynomial method (KPM), estatística de espaçamento entre níveis, e análise do inverso do rácio de participação. Estas transições mostraram naturezas variadas no que concerne a forma como estas propriedades variam na vizinhança das transições topológicas. Adicionalmente, encontrámos fases que exibem estados críticos nas fronteiras do hiato de energia. Em conjunto com estas descobertas, encontrámos em ambos os sistemas comportamento re-entrante, em que a fase topológica é induzida pelo aumento da amplitude da quase-desordem.

[This page was intentionally left blank]

Contents

List of Figures

[This page was intentionally left blank]

Glossary

QPS	Quantum Periodic Systems
QHE	Quantum Hall Effect
TAI	Topological Anderson Insulator
AI	Anderson Insulator
NI	Normal Insulator
CI	Chern Insulator
CM	Critical Metal
CCI	Critical Chern Insulator
TBLG	Twisted Bilayer Graphene

1. Introduction

1.1. Motivation

Thermodynamic systems can exist in different phases, often with radical macroscopic differences. We call the abrupt change in phase at a particular temperature a *phase transition* [49], and the temperature at which it occurs the *critical temperature*, T_C. This concept of phase transition has long fascinated thinkers throughout the ages, since phase transitions are a part of daily human life in the form of the changing phases of water and other substances: from liquid water to ice, for example. In fact, this particular category of phase transitions is that which most people immediately acknowledge when this topic is mentioned. However, phase transitions are present in a wide range of systems spanning the whole scope of scientific sub-categories, from biology to physics.

As mentioned before, phase transitions are a sudden change in the phase of a system. Typically, these phases are identified by an *order parameter* that vanishes above the critical temperature and is finite below it. As an example we consider the ferromagnet to paramagnet transition, where the order parameter is the total magnetization. When the temperature is very high, higher than T_C, we can perceive the magnetic moments as being randomly oriented. Thus, the sum total of their individual contributions to the total magnetization of the system will be 0. However, as we decrease the temperature we can expect a gradual alignment of the magnetic moments as a result of the interacting forces between them, that are no longer overwhelmed by the thermal disorder of the system. When the temperature dips below T_C the magnetic moments all align in the same direction.

It is worth noting in the previous example another characteristic of phases transitions: namely, that there was a spontaneous symmetry breaking in the transition from the disordered to the ordered state. In the disorder state, the system has full rotational symmetry; in the ordered state that is no longer the case since we introduced a preferencial direction in the system, that with which all the magnetic moments are aligned. This is a critical aspect of the theory of phase transitions.

Landau theory is capable of explaining these phase transition phenomena, and makes a distinction between first and second order phase transitions, the former being characterized by a discontinuous change in the order parameter and the latter by a continuous change.

Another example of phases are metal and insulator. These can be understood using band

theory, however, this method does not hold up in the case where we consider interactions between electrons in our system or even when we introduce disorder, since in these situations the wave vector is no longer a good quantum number. This is evidenced by the fact that we can have insulating phases without a gapped energy spectrum that are disorder-driven, called Anderson insulators. We will see that we can understand this by changing our perspective of analysis to one focused on the localization of states.

Quasi-periodic systems (QPS) have attracted in recent times a great amount of interest, since they show interesting properties [16, 17] without the presence of disorder, because they are entirely deterministic. These systems show extended, localized and critical phases already in 1D systems. This differs from typical uncorrelated disordered systems, where transistions from localized to delocalized states are only possible in 3D.

In this thesis, we study two-dimensional systems subject to an incommensurate potential, which have analogous physics to twisted bilayer graphene (TBLG), since both systems create a Moiré lattice. A Moiré lattice is an emergent lattice formed by the Moiré pattern from two superimposed periodic patterns.

1.2. Objectives

In this thesis, we set out to understand the interplay between quasi-disorder and topology in two-dimensional systems. We focus mainly on two systems, discovering a landscape of phases for each. The first model is the Haldane model, a very-well known topological model with broken time-reversal symmetry and zero net magnetic flux. The second is a model in a square lattice with nearest neighbour hopping elements, exhibiting a more complex topological character. We will analyze these models under increasing incommensurate potential identifying topological phases and transitions.

For this, we employ numerical methods in order to calculate topological invariants, as well as characteristics of our system and properties of its states.

1.3. Thesis outline

This document is divided in 6 chapters whose contents are summarized in the following way:

- In **chapter 1**, we will look at several fundamental ideas that will be utilized throughout this work, as well as provide an outline of the current status of research in the fields of topological systems and quasi-periodicity.
- In **chapter 2**, we present the models that will be the subject of our study, giving an overview of their properties in a clean state. These are the Haldane model and the

model on the square lattice.

- In **chapter 3**, we describe the numerical methods employed throughout this work, namely the Kernel Polynomial Method (KPM) to calculate spectral properties and the Coupling matrix method to compute the topological invariant in these systems.
- In **chapter 4**, we show the results obtained for the Haldane model subject to the incommensurate potential: its phase diagram and localization properties of the states.
- In **chapter 5**, we look at the results for the model on the square lattice.
- In **chapter 6**, we give a summary of the conclusions extracted from this work and present a reflection on the future directions worth exploring.

1.4. Topological phases and the QHE

The notion of a new topological phase for systems with no long-range order was first introduced by Kosterlitz and Thouless [32, 57] in 1973, and the first experimental realization [29] was evidenced in the integer quantum Hall effect (QHE). Before understanding the quantum Hall effect, we must first understand the classical Hall effect [21]. We consider a magnetic field applied perpendicular to the direction of current flow. Classical electromagnetism tells us that the charges will experience a force (called the Lorentz force) in the direction that is perpendiuclar to both the field and the direction of current flow. Subject to this force, the electric charges will accumulate on the side of the material through which the current is flowing, creating a transverse voltage in the material - the Hall voltage V_H. It has been shown, classically, that $\rho_{xy} = \frac{V_H}{I}$ is proportional to B, the magnetic field. However, Von Klitzing showed experimentally that this linear behaviour does not hold for electrons confined in two dimensions subject to very intense magnetic field at low temperatures, and that instead, a series of plateaus in the transverse conductivity were observed, which can be described by

$$\rho_{xy} = \frac{h}{e^2}\frac{1}{n} \quad , \, n \text{ integer}, \tag{1.1}$$

where h is Planck's constant and e is the charge of the electron.

This is a purely quantum effect that cannot be explained through a classical frame of mind. For large magnetic fields, this problem is reduced to the motion of electrons confined to a plane subject to a magnetic field. This problem was already solved by Landau [39] and the density of states is given by what are called the Landau levels described by

$$E_n = \hbar\omega_C \left(n + \frac{1}{2}\right), \tag{1.2}$$

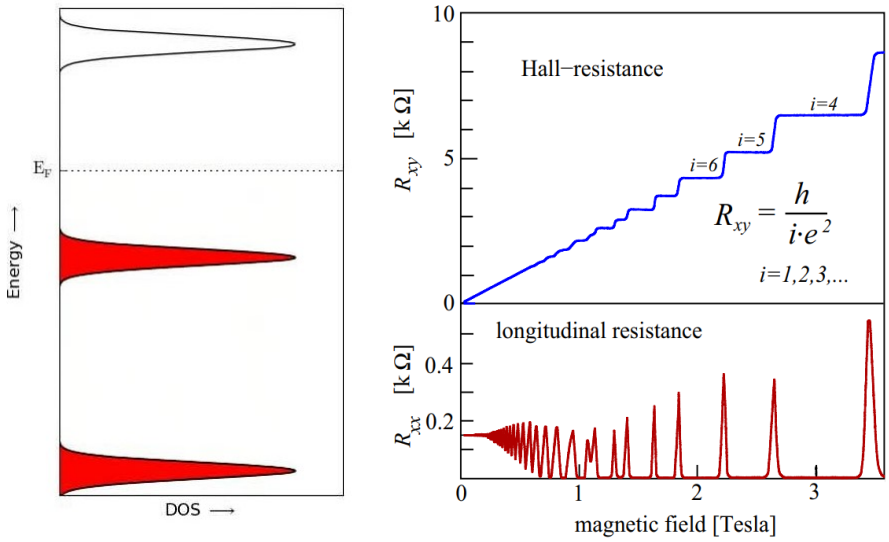

Figure 1.1.: Demonstration of the quantum Hall effect. (left) Landau levels, with E_F standing for the Fermi energy. The levels below the Fermi energy are coloured red to indicate that they are occupied. (right) Hall and longitudinal resistance as a function of applied magnetic field. We very clearly see the plateaus in the Hall resistance.

where $\omega_C = eB/m$ is called the cyclotron frequency. It was also shown that these levels have a degeneracy proportional to B. However, this still does not explain the plateaus. We could imagine having a conductivity given by $\sigma_{xy} = ne^2/h$ if the total number of electrons was a multiple of the number of states per Landau level, but never the plateaus.

The plateaus can only be explained by considering the effect the disorder has on the system. In the first place, it broadens the Landau levels into Lorentzian shaped curves. Furthermore, because the presence of a magnetic field breaks the time-reversal symmetry of the system, extended (current-carrying) states may exist at the Landau levels. Knowing this, it is clear that the sudden jumps in conductivity occur when the Fermi level crosses one of these extended states and remains unchanged when crossing the other states because they are localized.

This example clearly shows us the topological character of these phases, defined by the plateaus in conductivity. They arise, not by the change in a local order parameter (such parameter cannot be constructed) but by the overall characteristics of the states and energies of the system. Additionaly, the Hall conductance is insensitive to continuous changes in the parameters, and depends only on the number of Landau levels crossed.

1.5. Berry phase

The concept of Berry phase is of paramount importance in the understanding of the underlying theory of this work. We will then now go through a brief overview of its key concepts.

The Berry phase was first introduced by Berry [60] and has since had a great impact in many areas of physics. It concerns itself with Hamiltonians that evolve adiabatically according to a set of parameters $\left\{\overrightarrow{\mathbf{R}}(t)\right\}$. We consider a transport around a closed path (circuit) $\mathcal{C}$, between times $t = 0$ and $t = T$. The eigenstates of the system have their time evolution determined by the usual Schrödinger's equation. The basis of eigenstates at a given time t is $\left|n\left(\overrightarrow{\mathbf{R}}(t)\right)\right\rangle$.

Thus, after a time t, under the adiabatic approximaton, a state that started as $\left|n\left(\overrightarrow{\mathbf{R}}(0)\right)\right\rangle$ will be in a state $\left|n\left(\overrightarrow{\mathbf{R}}(t)\right)\right\rangle$. During this time it may acquire a phase $\theta(t)$, therefore we write $|\psi(t)\rangle = e^{-i\theta(t)}\left|n\left(\overrightarrow{\mathbf{R}}(t)\right)\right\rangle$, with the phase given by (see Apendix A)

$$\theta(t) = \frac{1}{\hbar}\int_0^t dt' E_n\left(\overrightarrow{\mathbf{R}}(t')\right) - i\int_0^t \left\langle n\left(\overrightarrow{\mathbf{R}}(t')\right)\right| \frac{d}{dt'}\left|n\left(\overrightarrow{\mathbf{R}}(t')\right)\right\rangle. \tag{1.3}$$

We define $\gamma_n \equiv i\int_0^t dt' \left\langle n\left(\overrightarrow{\mathbf{R}}(t')\right)\right| \frac{d}{dt'}\left|n\left(\overrightarrow{\mathbf{R}}(t')\right)\right\rangle$ as the Berry phase. We can further rewrite it as

$$\gamma_n = i\int_{\mathcal{C}} \left\langle n\left(\overrightarrow{\mathbf{R}}\right)\right| \nabla_{\overrightarrow{\mathbf{R}}}\left|n\left(\overrightarrow{\mathbf{R}}\right)\right\rangle \cdot d\overrightarrow{\mathbf{R}}, \tag{1.4}$$

where now we have an integral over the space of parameters $\left\{\overrightarrow{\mathbf{R}}\right\}$ over the circuit $\mathcal{C}$. We define $\overrightarrow{\mathcal{A}}_n\left(\overrightarrow{\mathbf{R}}\right) = i\left\langle n\left(\overrightarrow{\mathbf{R}}\right)\right| \nabla_{\overrightarrow{\mathbf{R}}}\left|n\left(\overrightarrow{\mathbf{R}}\right)\right\rangle$, the Berry connection which is gauge dependent and real.

In turn, the introduction of a gauge transformation changes the Berry phase in the following way

$$\gamma_n' \to \gamma_n + \alpha\left(\overrightarrow{\mathbf{R}}(T)\right) - \alpha\left(\overrightarrow{\mathbf{R}}(0)\right). \tag{1.5}$$

We see that for a general circuit this Berry phase will be gauge dependent. However, Berry observed that if we instead have a closed loop, then $\overrightarrow{\mathbf{R}}(T) = \overrightarrow{\mathbf{R}}(0)$. In this case, the terms corresponding to values of α will vanish and we are left with a gauge-independent quantity. Being a gauge-independent quantity, it means that this geometrical phase can then be observed and has real physical implications, such as the Aharonov-Bohm effect [2].

Another important quantity for the study of the topological properties of quantum systems is the Berry curvature defined as $\overrightarrow{\mathbf{\Omega}}_n\left(\overrightarrow{\mathbf{R}}\right) = \nabla_{\overrightarrow{\mathbf{R}}} \times \overrightarrow{\mathcal{A}}_n\left(\overrightarrow{\mathbf{R}}\right)$, such that

$$\int_{\mathcal{C}} \overrightarrow{\mathcal{A}}_n\left(\overrightarrow{\mathbf{R}}\right) \cdot d\overrightarrow{\mathbf{R}} = \int_{\mathcal{S}} \overrightarrow{\mathbf{\Omega}}_n\left(\overrightarrow{\mathbf{R}}\right) \cdot \overrightarrow{\mathbf{dS}}, \tag{1.6}$$

where $\mathcal{S}$ is the region enclosed by the circuit $\mathcal{C}$. We can now define a topological invariant that characterizes 2D insulators with broken time-reversal symmetry called the Chern number

$$C_n = \frac{1}{2\pi} \int_{\mathcal{S}} \overrightarrow{\mathbf{\Omega}}_n \left(\overrightarrow{\mathbf{R}} \right) \cdot \overrightarrow{\mathbf{dS}}. \tag{1.7}$$

In a system with multiple bands, the total Chern number will be the sum of the Chern number over all occupied bands $C = \sum_n C_n$. Notice that this quantity is undefined in the case where we have the Fermi level lying inside a band, and thus a closed gap in our system; since the Chern number is a property of the whole band, it would not make sense to calculate the Chern number of a partially filled band.

This Berry curvature and, consequently, the Chern number are gauge-independent as we have seen before, and manifest themselves in physical properties of materials. In particular, it was shown that the Hall conductivity in two dimensions can be associated with the topological invariant C [57].

1.6. Topological Insulators

1.6.1. Insulators in band theory

The first theoretical description of solid states of matter was achieved very early on in the history of quantum mechanics, and is generally called band theory of solids [10, 12]. By exploiting the translation invariance of crystals it was possible to describe the energy levels of this periodic lattice as the eigenvalues $E_{\overrightarrow{\mathbf{k}}}$ of a Bloch Hamiltonian $H_{\overrightarrow{\mathbf{k}}}$, labeled according to the quantum number $\overrightarrow{\mathbf{k}}$ called the Bloch momentum. These eigenvalues define energy bands organized into a band structure. This band structure gives us a very valuable tool to describe a wide range of quantum transport phenomena in solids with a relatively simple language.

In band theory, insulators are simply states of matter whose highest filled energy band is completely filled, opposed to metals, where this band is only partially filled. Thus, in insulators an energy gap separates the conduction band from the valence band, so that a finite amount of energy is required to dislodge an electron from the former to the latter.

However, in the QHE we saw in the previous section, we can also look at the Landau levels as forming a band structure where we have a finite energy gap between Landau levels. Yet, despite this, we see that the application of an electric field leads to a Hall current characterized by 1.1. What then is the difference between these two states?

1.6.2. Topology

The difference hinges on a matter of topology [57]. To understand this we make a little detour through the very basic concepts of the mathematical field of topology. The essence of the study of topology lies on the fact that certain results of geometric problems do not depend

on the exact shape of the objects, but on some other more abstract property. For example, Euler proved that it was impossible to find a route through Königsberg that would cross all of its seven bridges exactly once [13]. Notice that this solution is independent of the size, shape or colour of the bridges or even, on the distances between them. The only variable that goes into the resolution of the problem is the particular way in which the bridges are connected to different parts of the city. Thus, we could construct an equivalence class between all the cities in the world that have seven bridges whose connectivity properties are the same as those of the city of Königsberg in the 18th century, and thus, be sure that, for any of those cities, Euler's proof would apply. We say that these cities are homeomorphic.

Two spaces are homeomorphic if there is a smooth transformation that goes from one to the other. A very famous example is the donut and the coffee mug. It is possible to smoothly deform a coffee mug into a donut, hence they are homeomorphic. We can characterize this topological equivalence by the number of holes (genus) the object has. Both the coffee mug and the donut have a single hole, while a sphere has no holes, and so is not homeomorphic to either of the other objects.

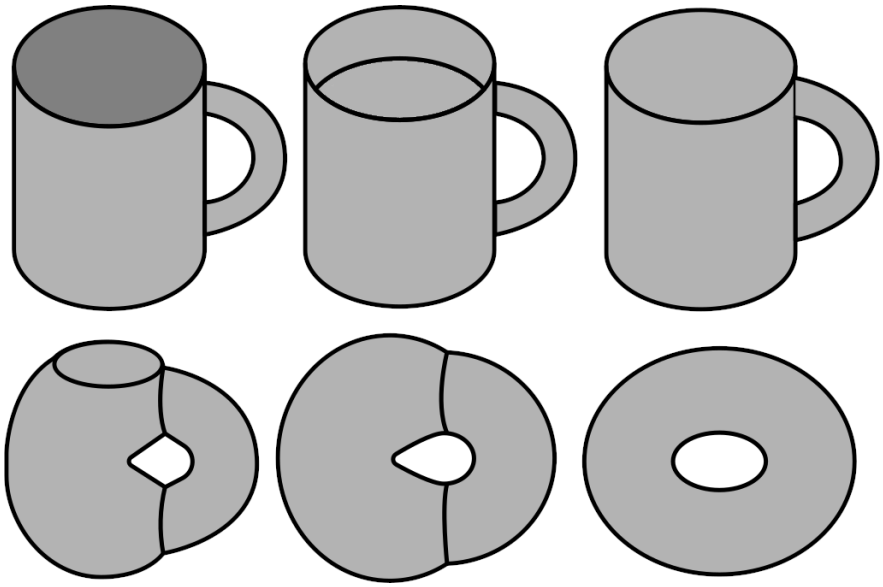

Figure 1.2.: Smooth transformation that takes a coffee mug and turns into a donut. This transformation is only possible because the coffee mug and the donut have the same topological invariant (number of holes) and we say that these two objects are homeomorphic.

Similarly, we can create an equivalence class between Hamiltonians that can be smoothly deformed without closing the gap. These different classes are identified by a topological invariant, analogous to the genus. The Chern number is an example of a topological invariant for bidmiensional systems with broken time-reversal symmetry, which has a physical parallel

with the concept of Berry phase, whose construction was shown in a previous section 1.5.

1.6.3. Topology in condensed matter physics

We may now understand the difference between the usual insulators and the QHE: common insulators belong to an equivalence class characterized by a topological invariant $C = 0$. We say that they are topologically trivial. On the other hand, in the QHE we have a topologically non-trivial system with quantized, non-zero Chern number. In fact, as was mentioned previously, this Chern number has physical consequences, namely, the Hall conductivity σ_{xy} is proportional to the Chern number. Thus, the QHE can now be understood with this new topological language. When we are in a plateau of conductivity $\sigma_{xy} = \frac{e^2 n}{h}$ our Hamiltonian belongs to an equivalence class with topological invariant n. By increasing the Fermi level, we are making a smooth transformation of our Hamiltonian that does not close the gap. However, we now know that the topological invariant is unaffected by those transformations. Nevertheless, once the Fermi energy reaches a Landau level we are closing the gap of our system and the Chern number is undefined. The reopening of the gap, that is, the crossing of the Landau level, changes our system into another class of equivalence, with another topological invariant, yielding experimentally another plateau in the conductivity.

A crucial aspect of these topological states of matter is the bulk-boundary correspondance. This simply means that there will be gapless conducting states at interfaces where the topological invariant changes [22, 24, 46]. This has been observed at interfaces between quantum Hall states and the vacuum. An intuitive picture to understand the presence of these edge states is to consider a slab of a material that exhibits the topological properties hitherto described, in contact with the vacuum. Now, we may imagine ourselves travelling from the topological phase of matter in the slab into the vacuum (which is topologically trivial), passing through the interface between them. In both sides there is an energy gap, however characterized by distinct topological invariants. We know that smooth transitions of the Hamiltonian that do not close the gap cannot change the Chern number, and so we must have a point of vanishing gap at the interface to accomodate this topological change. Ergo, we will have conducting gapless states at the interface between the topological material and the vacuum, or other materials with different Chern number. Another property of these edge states is that they are chiral, which means they propagate only in one direction along the interface. As we will se in the next section, this chirality makes them very robust to the presence of disorder, since events of backpropagation are very improbable.

Even though the QHE is topological only due to the application of an external magnetic potential, it is possible to conceive models with no net magnetic flux that show a quantum Hall effect. The first theoretical example of one such model was first idealized by Haldane [20], and thus bears his name. The Haldane model is central to most of the work done throughout this thesis and has a dedicated Section further along in this document 2.1.

1.7. Localization

The study of localization properties of states is essential for the understanding of many physical phenomena in condensed matter physics, such as, for example, the metal-insulator transition [33]. The history of localization starts with Anderson which first described this phenomenon in the presence of a random potential, as a way to explain the absence of diffusion in certain lattices, proposing that for strong disorder there would be a strong spatial localization of states [3].

Anderson proposed the following tight-binding model

$$H = \sum_{\vec{\mathbf{R}}} \epsilon_{\vec{\mathbf{R}}} a^{\dagger}_{\vec{\mathbf{R}}} a_{\vec{\mathbf{R}}} + V \sum_{\vec{\mathbf{R}},\vec{\mathbf{R}'}} a^{\dagger}_{\vec{\mathbf{R}}} a_{\vec{\mathbf{R}'}}. \tag{1.8}$$

We will consider the case where we only have hoppings between nearest-neighbours and write

$$H = \sum_{\vec{\mathbf{R}}} \epsilon_{\vec{\mathbf{R}}} a^{\dagger}_{\vec{\mathbf{R}}} a_{\vec{\mathbf{R}}} + \nu \left(a^{\dagger}_{\vec{\mathbf{R}}} a_{\vec{\mathbf{R}}+\hat{\mathbf{x}}} + a^{\dagger}_{\vec{\mathbf{R}}} a_{\vec{\mathbf{R}}+\hat{\mathbf{y}}} + a^{\dagger}_{\vec{\mathbf{R}}} a_{\vec{\mathbf{R}}+\hat{\mathbf{z}}} + h.c. \right), \tag{1.9}$$

where $\epsilon_{\vec{\mathbf{R}}}$ is an on-site energy at site $\vec{\mathbf{R}}$ taken at random from a probability distribution chracterized by a width W which we call the disorder strength. One may wonder how a given state $|\Psi\rangle$ will evolve in this disordered system and, in particular, how the amplitude of $|\Psi\rangle$ at a given site j, $|\langle j \mid \psi \rangle|^2$ will decay as $t \to \infty$.

In the disorder-free case we can use Bloch's theorem and write the eigenstates of our Hamiltonian as $\psi_k\left(\vec{\mathbf{r}}_j\right) = \frac{1}{\sqrt{L^d}} e^{i\vec{\mathbf{k}}\cdot\vec{\mathbf{r}}_j}$, where $k_i = \frac{2\pi}{L} n$. The eigenvalues can be calculated and read $E_k = 2\nu \sum_{i=1}^{d} \cos\left(k_i\right)$.

If we consider an initial state localized at site j, $\Psi\left(t=0, j\right) = \frac{1}{L^d} \sum_{\vec{\mathbf{k}}} e^{i\vec{\mathbf{k}}\cdot\vec{\mathbf{r}}_j}$,From Schrödinger's equation, our state at time t can be written as

$$\Psi\left(t, j\right) = \frac{1}{L^d} \sum_{\vec{\mathbf{k}}} e^{i\vec{\mathbf{k}}\cdot\vec{\mathbf{r}}_j - 2it\nu\sum_{i=1}^{d}\cos(k_i)}. \tag{1.10}$$

It can be shown that in the thermodynamic limit our wavefunction has the form $\Psi\left(t, j\right) = \prod_{l=1}^{d} i^{r_l^{(j)}} J_{r_l^{(j)}}\left(-2t\nu\right)$ (see B). Now we may use an approximation for the Bessel function for large argument and write the probability of returning to site j as

$$p\left(t\right) = \left|\Psi\left(t, j\right)\right|^2 \sim \left| \prod_{l=1}^{d} t^{-1/2} \right|^2 = t^{-d}. \tag{1.11}$$

We can see that as time evolves to infinity the return probability goes to zero. This is to be expected intuitively, since Bloch states can be seen to extend over the entirety of our system.

The infinitely disordered case is much simpler. We may consider our Hamiltonian to be simply the diagonal term, since we are assuming that disorder is the dominating term of our

system. In this case, an initial state localized at a site j will remain at that same site since the time evolution operator is diagonal in the lattice site basis and the return probability will be, naturally, 1.

After this analysis, we would assume that there would be a smooth transition between the extended and the localized state. However, Anderson [3] showed that for $d = 1, 2$ any amount of disorder will completely localize the system [1].

In fact, these localized states are exponentially localized and their wavefunction can be written as

$$\psi \sim e^{-r/\xi}, \tag{1.12}$$

where ξ is called the *localization length* and can be seen as a characteristic length of localized states.

This localization of states has important consequences, for example, in the conductivity of materials enabling the possibility to drive materials into an insulating phase by the presence of disorder. As mentioned previously, in one dimension any amount of disorder drives a system into this state [3]. However, metallic states in 2D with strong spin-orbit coupling or interactions experience a metalic-insulator transition at a non-zero critical disorder [4, 23, 36, 41, 47].

It is of interest to us to consider what are the effects of incommensurability on the localization of states. The simplest model was introduced by Aubry and André [8] and is simply a unidimensional tight-binding chain with nearest-neighbour hoppings and on-site energies modulated by a cosine whose periodicity is incommensurate with the periodicity of the underlying crystaline lattice. This model is known to have a metal-to-insulator transition for a finite value of quasi-disorder strength, localizing the single-particle states of the system simultaneously for all eigenstates [8, 55].

Incommensurability also plays an important role in these two-dimensional heterostructures with Ref. [45] predicting localization in the "dodecagonal graphene quasicrystal" [62], linking this phenomenon with the quasi-periodic nature of this structure. In Ref. [14] it was shown that the effect of an incommensurate twist could be emulated by the presence of a quasi-periodic potential. This ushered in the inception of a new class of models, called magic angle semimetals, which exhibit similar properties to those of twisted bilayer graphene.

Recently, Fu, Wilson, and Pixley [15] showed that for a simple two-dimensional model of a topological insulator the presence of quasi-periodicity induced critical eigenstates, flat bands and several Anderson-like transitions.

1.8. Disordered Chern insulators

1.8.1. Disorder and topology

After the discovery of the quantum Hall effect, it was realized that two-dimensional Chern insulator require a finte amount of disorder to localize [18]. Bands with non-zero Chern number, despite almost all eigenstates being localized, have extended states at isolated energies. These states are said to carry the Chern number. Laughlin [40] showed that these Chern carrying states would "levitate" in energy to one another, with increasing disorder. Eventually, they would merge and "annihilate" each other, ensuing Anderson localization.

Besides disorder, interactions and correlations at finite temperature [65] have been shown to drive systems into novel topological phases, such as the topological Mott insulator [48].

1.8.2. The Topological Anderson Insulator

We have seen that the QHE is the quintessential example of a topological state of matter, where the breaking of time-reversal symmetry plays a crucial role in the appearence of unidirectional edge states. However, recently an analogous effect was predicted in systems where time-reversal symmetry is preserved. Such is the case of graphene with strong spin-orbit coupling [26], being realized experimentally in HgTe quantum wells [31, 37]. These systems possess a single pair of helical edge states per edge, propagating in opposite directions, what we call the quantum spin Hall effect (QSH).

In an article studying the effect of disorder in these helical edge states, Li, Chu, Jain and Shen [41] surprisingly found, in computer simulations, a transition from an ordinary insulating state to a state with quantized conductance. They called this new phase topological Anderson insulator (TAI).

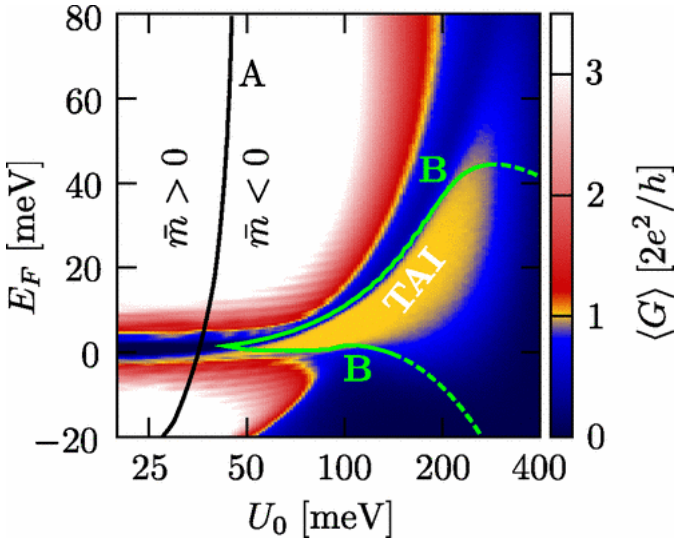

Figure 1.3.: Simulation of a HgTe quantum well showing the average conductance $\langle G \rangle$ as a function of disorder strength U_0 and Fermi energy E_F.

The mechanism that induces this new state is described by Groth et al. [19]. By modeling the HgTe quantum well with a low-energy effective Hamiltonian of the form [9]

$$H = \alpha \left(p_x \sigma_x - p_y \sigma_y \right) + \left(m + \beta p^2 \right) \sigma_z + \left[\gamma p^2 + U \left(\vec{\mathbf{r}} \right) \right] \sigma_0, \tag{1.13}$$

we see that it is a Dirac Hamiltonian with additional terms quadratic in p. It is indeed the relative sign of the parameters β and m that determines if our quantum well is a topological insulator or an ordinary insulator. If we take $\beta > 0$, the system is topological for $m < 0$.

Groth et al. argued that elastic scattering due to the presence of a disorder potential will localize states, which will then have the form $e^{-x/\lambda}$. The action of the term $\beta p^2 = -\hbar^2 \beta \nabla^2$ acting on these states will add a negative correction to the topological mass, making it so this new topological mass can have the opposite sign as the bare mass, making the system a topological insulator.

1.8.3. Topology and quasi-disorder

The discovery of topological insulators has also lead to an interest in the study of topological properties in QPS. Quasicrystals have been shown to exhibit nontrivial topology [34,35,59], as well as other exotic phenomena [52]. These properties have been attributed to the higher dimensional character of QPS, since they can be seen as originating from periodic constructions of a higher dimension [53].

The study of the interplay between topology and strong correlations has also yielded very interesting results, such as the fractional quantum Hall effect [54]. This interest has lead recent research in the direction of discovering new platforms to study strongly correlated systems,

the main example being the twisted graphene heterostructures.

These systems have been shown to exhibit very narrow, flat bands at low energies, when the relative angle between the two layers approaches the *magic angle* $\theta = 1.1^{\circ}$ [11,42,43,50,56,58]. In this regime, the physics is dominated by correlations and we see the formation of exotic many-body states. At odds with uncorrelated disorder, a systematic study of the interplay between non-trivial topology, quasi-disorder, and localization properties is still missing.

2. Models

2.1. Haldane Model

2.1.1. Hamiltonian and topological properties

As we have seen previously, we observe topological effects on systems that are subject to some external magnetic field that is able to split the Landau levels, such is the case of the QHE. However, in 1988 [20] Haldane showed that it is possible to obtain these topological effects in systems where there is broken time-reversal symmetry but no net magnetic flux. To demonstrate this, he introduced a model that was afterwards named after him. It is upon this model that most of the work in this document is done. It is therefore quite essential that we give a clear overview of the basics of the Haldane model and its properties.

We consider the honeycomb structure, which has two interpenetrating triangular sublattices labeled A and B [51]. If we consider only nearest-neighbour hopping elements t_1, we have a tight-binding model for graphene, which has been subject to extensive study. We now consider next-to-nearest neighbour hopping elements with a complex phase $t_2 e^{i\phi}$. We can understand this as the application of an external magnetic field. We can now choose these phases in such a way that the net flux within a unit cell is zero. This arrangement is simple and can be seen in the figure 2.1.

The real space Hamiltonian can then be written as

$$H = t \sum_{\langle i,j \rangle} c^{\dagger}_{\overrightarrow{\mathbf{R}}_i A} c_{\overrightarrow{\mathbf{R}}_j B} + h.c. + \sum_{\sigma} \left[t_2 \sum_{\langle\langle i,j \rangle\rangle} e^{-i\phi_{ij}} c^{\dagger}_{\overrightarrow{\mathbf{R}}_i \sigma} c_{\overrightarrow{\mathbf{R}}_j \sigma} + h.c. + m\eta_\sigma \sum_i c^{\dagger}_{\overrightarrow{\mathbf{R}}_i \sigma} c_{\overrightarrow{\mathbf{R}}_i \sigma} \right] \quad (2.1)$$

where $c^{(\dagger)}_{\overrightarrow{\mathbf{R}}_i \sigma}$ destroys (creates) a fermionic state at site $\overrightarrow{\mathbf{R}}_i$ in sublattice σ with $\sigma = A, B$. Additionally, a mass term is included that is positive in one sublattice and negative in the other ($\eta_A = -\eta_B = 1$).

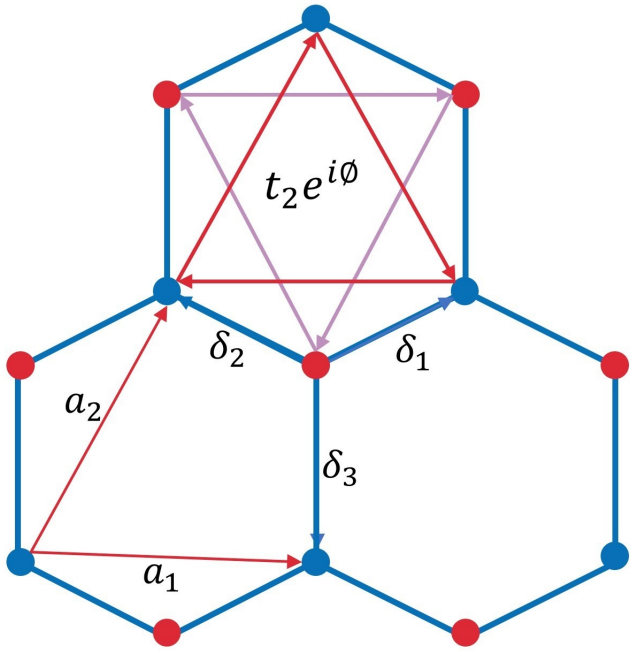

Figure 2.1.: Unit cell of the Haldane model. The arrows show the positive flow of fluxes. The vectors $\vec{\mathbf{a_1}} = a\,(1,0)$ and $\vec{\mathbf{a_2}} = a\left(\frac{1}{2}, \frac{\sqrt{3}}{2}\right)$, with a being the carbon-carbon distance, are the primitive vectors of this lattice.

We can write this Hamiltonian in reciprocal space by defining

$$\begin{aligned} c^{\dagger}_{\vec{\mathbf{R}}\sigma} &= \tfrac{1}{\sqrt{N}} \textstyle\sum_{\vec{\mathbf{k}}} e^{-i\vec{\mathbf{k}}\cdot\vec{\mathbf{R}}} c^{\dagger}_{\vec{\mathbf{k}}\sigma} \\ c_{\vec{\mathbf{R}}\sigma} &= \tfrac{1}{\sqrt{N}} \textstyle\sum_{\vec{\mathbf{k}}} e^{i\vec{\mathbf{k}}\cdot\vec{\mathbf{R}}} c_{\vec{\mathbf{k}}\sigma} \end{aligned} \quad . \tag{2.2}$$

For the first term in equation 2.1, we always have hoppings between sites in different sublattices, and the elements are given by

$$\begin{aligned} & t\frac{1}{N} \sum_{\langle i,j\rangle} \sum_{\vec{\mathbf{k}}\vec{\mathbf{k}'}} e^{-i\vec{\mathbf{k}}\cdot\vec{\mathbf{R}_\mathbf{i}}} e^{i\vec{\mathbf{k}'}\cdot\vec{\mathbf{R}_\mathbf{j}}} c^{\dagger}_{\vec{\mathbf{k}}B} c_{\vec{\mathbf{k}'}A} \\ &= t \sum_{\vec{\mathbf{k}}} \left(e^{i\vec{\mathbf{k}}\cdot\vec{\mathbf{a}}_1} + e^{i\vec{\mathbf{k}}\cdot\vec{\mathbf{a}}_2} + 1 \right) c^{\dagger}_{\vec{\mathbf{k}}B} c_{\vec{\mathbf{k}}A} \end{aligned} \quad . \tag{2.3}$$

Where we used $\sum_i e^{-i\left(\vec{\mathbf{k}}-\vec{\mathbf{k}'}\right)\cdot\vec{\mathbf{R}_\mathbf{i}}} = N\delta\left(\vec{\mathbf{k}} - \vec{\mathbf{k}'}\right)$.

For the second term we only have hoppings within the same sublattice given by

$$\begin{aligned} & t_2 \frac{1}{N} \sum_{\langle\langle i,j \rangle\rangle} \sum_{\vec{\mathbf{k}}\vec{\mathbf{k}'}} e^{-i\phi_{ij}} e^{-i\vec{\mathbf{k}}\cdot\vec{\mathbf{R}_\mathbf{i}}} e^{i\vec{\mathbf{k}'}\cdot\vec{\mathbf{R}_\mathbf{j}}} c^\dagger_{\vec{\mathbf{k}}B} c_{\vec{\mathbf{k}'}B} \\ = t_2 \sum_{\vec{\mathbf{k}}} (e^{i\left(\vec{\mathbf{k}}\cdot\vec{\mathbf{a}}_1+\phi\right)} + e^{i\left(\vec{\mathbf{k}}\cdot\vec{\mathbf{a}}_2-\phi\right)} + e^{i\left(\vec{\mathbf{k}}\cdot(\vec{\mathbf{a}}_1-\vec{\mathbf{a}}_2)-\phi\right)} + h.c) c^\dagger_{\vec{\mathbf{k}}B} c_{\vec{\mathbf{k}}B} \end{aligned} . \tag{2.4}$$

The last term is simply an on-site energy that differentiates between sublattices

$$\begin{aligned} & m \textstyle\sum_{i\in\sigma} \eta_i \sum_{\vec{\mathbf{k}}\vec{\mathbf{k}'}} e^{-i\vec{\mathbf{k}}\cdot\vec{\mathbf{R}_\mathbf{i}}} e^{i\vec{\mathbf{k}'}\cdot\vec{\mathbf{R}_\mathbf{i}}} c^\dagger_{\vec{\mathbf{k}}\sigma} c_{\vec{\mathbf{k}'}\sigma} \\ & = \textstyle\sum_{\vec{\mathbf{k}}} m\eta_\sigma \end{aligned} \tag{2.5}$$

This Hamiltonian can be written now in the momentum basis as

$$H = \sum_{\vec{\mathbf{k}}} c^\dagger_{\vec{\mathbf{k}}} \left(\vec{\mathbf{h}} \left(\vec{\mathbf{k}} \right) \cdot \vec{\sigma} + h_0 \mathcal{I} \right) c_{\vec{\mathbf{k}}}, \tag{2.6}$$

where $c_{\vec{\mathbf{k}}} = \left(c_{\vec{\mathbf{k}},A}, c_{\vec{\mathbf{k}},B} \right)$, $\vec{\sigma} = (\sigma_x, \sigma_y, \sigma_z)$ and

$$\vec{\mathbf{h}} \left(\vec{\mathbf{k}} \right) = (h_x, h_y, h_z) \tag{2.7}$$

with

$$\begin{aligned} h_0 &= 2t_2 \cos(\phi) \textstyle\sum_i \cos\left(\vec{\mathbf{k}} \cdot \vec{\mathbf{a}}_i \right) \\ h_x &= t \left(1 + \cos\left(\vec{\mathbf{k}} \cdot \vec{\mathbf{a}}_1 \right) + \cos\left(\vec{\mathbf{k}} \cdot \vec{\mathbf{a}}_2 \right) \right) \\ h_y &= -t \left(\sin\left(\vec{\mathbf{k}} \cdot \vec{\mathbf{a}}_1 \right) + \sin\left(\vec{\mathbf{k}} \cdot \vec{\mathbf{a}}_2 \right) \right) \\ h_z &= m + 2t_2 \sin(\phi) \left[\sin\left(\vec{\mathbf{k}} \cdot \vec{\mathbf{a}}_1 \right) - \sin\left(\vec{\mathbf{k}} \cdot \vec{\mathbf{a}}_2 \right) - \sin\left(\vec{\mathbf{k}} \cdot \vec{\mathbf{a}}_3 \right) \right] \end{aligned} , \tag{2.8}$$

where $\vec{\mathbf{a_1}} = a(1,0)$ and $\vec{\mathbf{a_2}} = a\left(\frac{1}{2}, \frac{\sqrt{3}}{2} \right)$.

We can now diagonalize this new Hamiltonian (Appendix C) and obtain the two energy bands as a function of $\vec{\mathbf{k}}$. They can be simply identified with the norm of $\vec{\mathbf{h}} \left(\vec{\mathbf{k}} \right)$:

$$E_\pm \left(\vec{\mathbf{k}} \right) = \pm \left| \vec{\mathbf{h}} \left(\vec{\mathbf{k}} \right) \right| + h_0 \left(\vec{\mathbf{k}} \right) \tag{2.9}$$

In Figure 4.7 we represent an example of energy bands of this system.

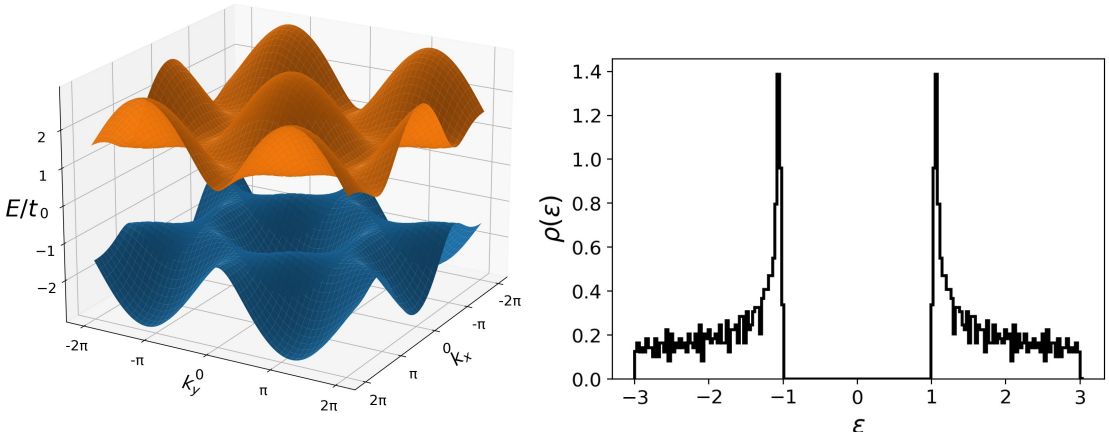

Figure 2.2.: (left) Bands of the Haldane model with parameters: $t_2 = 0.2$, $m = 0$ and $\phi = \pi/2$. (right) Density of states of the Haldane model for the same parameters of subfigure (a). As we can see, there is a gap.

We find that we have an energy gap around $\varepsilon = 0$ given by

$$\Delta = 2\left|\overrightarrow{\mathbf{h}}\left(\overrightarrow{\mathbf{k}}\right)\right| \tag{2.10}$$

As in the case of simple graphene, the points of highest symmetry are the points $\overrightarrow{\mathbf{K}} = \frac{2\pi}{3}\left(1, \sqrt{3}\right)$ and $\overrightarrow{\mathbf{K}'} = \frac{2\pi}{3}\left(-1, \sqrt{3}\right)$ and it is at these point that we will see gap closings. Indeed, we have gap closing at point $\overrightarrow{\mathbf{K}}$ for $m = -3\sqrt{3}t_2 \sin(\phi)$, and at $\overrightarrow{\mathbf{K}'}$ for $m = 3\sqrt{3}\sin(\phi)$.

We can now expand the Hamiltonian of our system around these high symmetry points. This will be useful since close to the topological transitions we have a very high concentration of Berry curvature precisely around these points:

$$\begin{aligned} H\left(\overrightarrow{\mathbf{K}} + \overrightarrow{\mathbf{q}}\right) &= -3t_2\cos(\phi)\mathcal{I} + \tfrac{\sqrt{3}}{2}t\left(q_x\sigma_x - q_y\sigma_y\right) + \left(m + 3\sqrt{3}t_2\sin(\phi)\right)\sigma_z \\ H\left(\overrightarrow{\mathbf{K}'} + \overrightarrow{\mathbf{q}}\right) &= -3t_2\cos(\phi)\mathcal{I} + \tfrac{\sqrt{3}}{2}t\left(-q_x\sigma_x - q_y\sigma_y\right) + \left(m - 3\sqrt{3}t_2\sin(\phi)\right)\sigma_z \end{aligned} . \tag{2.11}$$

We can summarize these two expressions by introducing a parameter ν that has value $+1$ in the vicinity of $\overrightarrow{\mathbf{K}}$ and -1 in the vicinity of $\overrightarrow{\mathbf{K}'}$.

$$\mathcal{H}\left(\overrightarrow{\mathbf{q}}\right) = -3t_2\cos(\phi)\mathcal{I} + \frac{\sqrt{3}}{2}t\left(\nu q_x\sigma_x - q_y\sigma_y\right) + \left(m + 3\sqrt{3}t_2\nu\sin(\phi)\right)\sigma_z. \tag{2.12}$$

We can now calculate the wavefunctions, which in this approximation yield

$$\left|\psi_{\nu}^{\pm}\left(\overrightarrow{\mathbf{q}}\right)\right\rangle = \frac{1}{\sqrt{2\left|h_{\nu}\right|\left(\left|h_{\nu}\right| \pm \left(m+\Sigma_{\nu}\right)\right)}} \begin{pmatrix} m+\Sigma_{\nu} \pm \left|h_{\nu}\right| \\ \hbar v_F\left(\nu q_x - i q_y\right) \end{pmatrix}, \tag{2.13}$$

defining $\Sigma_{\nu} = 3\sqrt{3}t_2\nu\sin\left(\phi\right)$, $\hbar v_F = \frac{\sqrt{3}}{2}t$ and $h_{\nu}\left(\overrightarrow{\mathbf{q}}\right) = \pm\sqrt{\left(\hbar v_F\right)^2\left|\overrightarrow{\mathbf{q}}\right|^2 + m + \Sigma_{\nu}} = \pm\left|h_{\nu}\right|$. In the following steps we will only consider the eigenfunctions with eigenvalue $-\left|h_{\nu}\right|$, $\left|\psi_{\nu}^{-}\left(\overrightarrow{\mathbf{q}}\right)\right\rangle$.

We may now notice that if we take the solution with eigenvalue $-\left|h\right|$ and evaluate it at $\overrightarrow{\mathbf{K}}'$, that is, set $\overrightarrow{\mathbf{q}} = \overrightarrow{\mathbf{0}}$ and $\nu = -1$, the eigenfunction will have a singularity for $m > 3\sqrt{3}t_2\sin\left(\phi\right)$. However, if we evaluate it in the vicinity of $\overrightarrow{\mathbf{K}}$ ($\nu = 1$) we will have a singularity for $m > -3\sqrt{3}t_2\sin\left(\phi\right)$. We arrive at the conclusion that it is impossible to define a single wavefunction that covers the entire Brillouin zone for $-3\sqrt{3}t_2\sin\left(\phi\right) < m < 3\sqrt{3}t_2\sin\left(\phi\right)$. Fortunately, we can redefine the wavefunction by using a gauge transformation [6, 30]

$$\left|\psi^{-}\left(\overrightarrow{\mathbf{q}}\right)\right\rangle \rightarrow e^{i\theta\left(\overrightarrow{\mathbf{q}}\right)}\left|\psi^{-}\left(\overrightarrow{\mathbf{q}}\right)\right\rangle. \tag{2.14}$$

Thus, we divide our Brillouin zone into two sectors, one including the $\overrightarrow{\mathbf{K}'}$ point, where the wavefunction is the one given in equation 2.13, which we will call $\left|\psi^{(K')}\left(\overrightarrow{\mathbf{q}}\right)\right\rangle$; and another sector containing the $\overrightarrow{\mathbf{K}}$ point, where the wavefunction is given by $\left|\psi^{(K)}\left(\overrightarrow{\mathbf{q}}\right)\right\rangle = e^{i\theta\left(\overrightarrow{\mathbf{q}}\right)}\left|\psi^{(K')}\left(\overrightarrow{\mathbf{q}}\right)\right\rangle$.

Making the appropriate phase choice we obtain an expression for $\left|\psi^{(K)}\left(\overrightarrow{\mathbf{q}}\right)\right\rangle$ that reads

$$\left|\psi^{(K)}\left(\overrightarrow{\mathbf{q}}\right)\right\rangle = \frac{1}{\sqrt{2\left|h_{\nu}\right|\left(\left|h_{\nu}\right| + \left(m+\Sigma_{\nu}\right)\right)}} \begin{pmatrix} -\hbar v_F\left(\nu q_x - i q_y\right) \\ m+\Sigma_{\nu}+\left|h_{\nu}\right| \end{pmatrix}. \tag{2.15}$$

In the vicinity of K this wavefunction will only be singular for $m < -3\sqrt{3}t_2\sin\left(\phi\right)$, which is precisely what we wanted. The phase we chose for this transformation is given by

$$e^{i\theta\left(\overrightarrow{\mathbf{q}}\right)} = \frac{\hbar v_F\left(m+\Sigma_{\nu}+\left|h_{\nu}\right|\right)\left|\left(\nu q_x - i q_y\right)\right|}{\left|m+\Sigma_{\nu}+\left|h_{\nu}\right|\right|\hbar v_F\left(\nu q_x - i q_y\right)}. \tag{2.16}$$

If we now wish to compute the topological invariant for this Hamiltonian we would use 1.7, thus being required to first calculate the Berry connection $\overrightarrow{\mathcal{A}}\left(\overrightarrow{\mathbf{q}}\right)$. By virtue of the construction we did previously, we would be left with two Berry connections $\overrightarrow{\mathcal{A}}^{(K')}\left(\overrightarrow{\mathbf{q}}\right), \overrightarrow{\mathcal{A}}^{(K)}\left(\overrightarrow{\mathbf{q}}\right)$, one for each sector. Our topological invariant would then read

$$C = \frac{1}{2\pi}\int_{S(K)}\left[\nabla_{\overrightarrow{\mathbf{q}}} \times \overrightarrow{\mathcal{A}}^{(K)}\left(\mathbf{q}\right)\right]\cdot d\overrightarrow{\mathbf{S}} + \frac{1}{2\pi}\int_{S(K')}\left[\nabla_{\overrightarrow{\mathbf{q}}} \times \overrightarrow{\mathcal{A}}^{(K')}\left(\mathbf{q}\right)\right]\cdot d\overrightarrow{\mathbf{S}}. \tag{2.17}$$

The difference between $\overrightarrow{\mathcal{A}}^{(K)}\left(\overrightarrow{\mathbf{q}}\right)$ and $\overrightarrow{\mathcal{A}}^{(K')}\left(\overrightarrow{\mathbf{q}}\right)$ is simply a gauge transformation, hence we can write

$$\overrightarrow{\mathcal{A}}^{(K)}\left(\overrightarrow{\mathbf{q}}\right) = \overrightarrow{\mathcal{A}}^{(K')}\left(\overrightarrow{\mathbf{q}}\right) - \nabla_{\overrightarrow{\mathbf{q}}}\theta\left(\overrightarrow{\mathbf{q}}\right). \tag{2.18}$$

We can then rewrite 2.17 as

$$C = \frac{1}{2\pi}\int_{\partial S}\left[\vec{\mathcal{A}}^{(K)}(\vec{\mathbf{q}}) - \vec{\mathcal{A}}^{(K')}(\vec{\mathbf{q}})\right]\cdot d\vec{\mathbf{q}} = -\frac{1}{2\pi}\int_{\partial S}\nabla_{\vec{\mathbf{q}}}\theta(\vec{\mathbf{q}})\cdot d\vec{\mathbf{q}}, \tag{2.19}$$

where ∂S is the intersection between the two sections of the Brillouin zone.

We can now finally obtain the result for the Chern number (see C.3)

$$C = 1. \tag{2.20}$$

From similar manipulations in other regions of the phase diagram, we can create the complete phase diagram for the Haldane model, shown below in Figure 2.3.

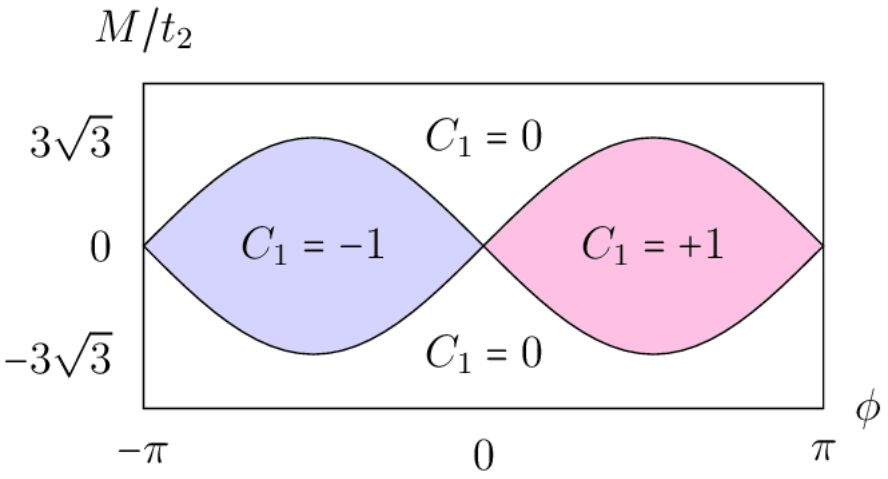

Figure 2.3.: Topological phase diagram for the Haldane model in the space of parameters (m, ϕ). We see that we have two non-trivial topological regions with Chern number $+1$ and -1. The curve that limits these phases is precisely the same curve described by equations 2.10, since it is only at points where the gap closes that we can have an alteration of the topological invaraint.

We can see in Figure 2.3 that there are 3 distinct phases in our system, identified with Chern number 1,0, and -1. The curve that limits these topological phases is the same curve where we have zero gap, defined previously by equations 2.10, since it is only at these points that we can have an alteration of the topological invariant.

We can verify that this system is indeed topological in nature by verifying the presence of gapless edge states that we mentioned are characteristic of this type of materials. For this we simulate a ribbon of the Haldane model as shown in Figure 2.4.

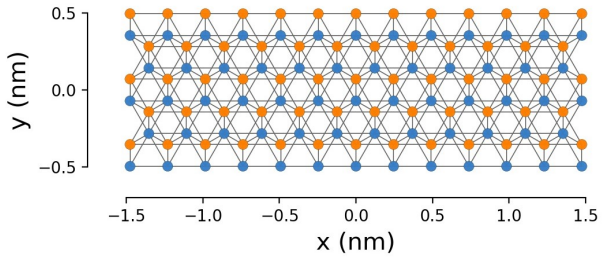

Figure 2.4.: Nano-ribbon of Haldane model obtained using the Python package *pybinding*

We impose translational invariance in one direction, in this case the y-direction, so that the wavefunctions become separable by Bloch's theorem

$$u(x, y) = e^{ik_y y} u(x) . \tag{2.21}$$

The spectrum in Figure 2.5 is obtained by imposing open boundary conditions in the x-direction.

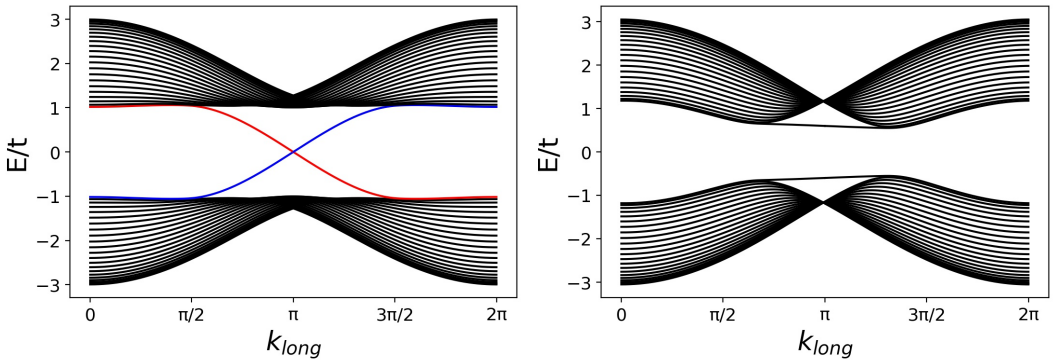

Figure 2.5.: Band strucutre of a nano-ribbon of the Haldane model. (left) Set of parameters for which the system is topological. (right) Set of parameters for which the system is topologically trivial. Both the results are obtained for a ribbon with length 40 sites and periodic boundary conditions in the y-direction.

It is clear that in the topological phase there are exactly two states that cross the zero energy level, while in the topologically trivial phase no states are present at the Fermi level. Representing the amplitude of the wavefunction at each site in our lattice for the two gapless states we obtain the following figure:

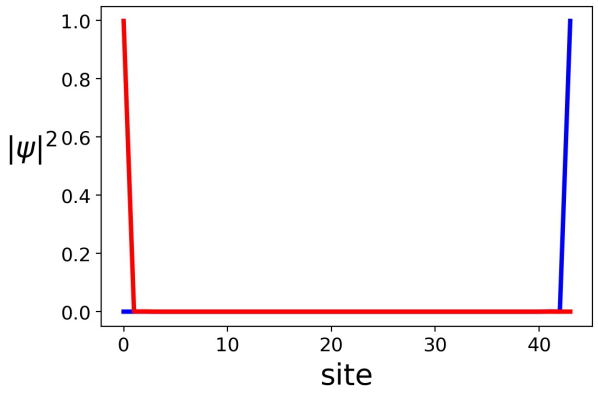

Figure 2.6.: Value of $|\psi|^2$ in each site of the lattice for the gapless edge states in the topological phase

Indeed, these states are localized at the edges of our ribbon, as was expected.

2.2. Square lattice model

In addition to the Haldane model we also studied the impact of a quasi-periodic potential on another topological model on a square lattice.

2.2.1. Hamiltonian and topological properties

The Hamiltonian in momentum space is written as

$$H(\overrightarrow{\mathbf{k}}) = \overrightarrow{\mathbf{h}}(k) \cdot \overrightarrow{\sigma}, \tag{2.22}$$

where $\overrightarrow{\sigma}$ is the Pauli matrices vector $\overrightarrow{\sigma} = (\sigma_x, \sigma_y, \sigma_z)$ and

$$\overrightarrow{\mathbf{h}}(k) = (sin(k_x), sin(k_y), M - tcos(k_x) - tcos(k_y)) \,. \tag{2.23}$$

For Hamiltonians of this type, the wavefunctions are given by C.5.

The system is gapped for every value of M except $M = \{0, -2, 2\}$. We can verify this by knowing that our system is gapless when $\overrightarrow{\mathbf{h}}(k) = 0$ and working out for which values of M this condition can be met. Associated with the gap closings we will see that there is a topological phase transition by computing the Chern number for each region. We also see that as we approach the topological phase transition value of M the Berry curvature becomes more and more concentrated around the wave vector $\overrightarrow{\mathbf{k}}_0 = \left(k_x^0, k_y^0\right)$ at which the gap closes. This really comes in handy when calculating the Chern number analytically, since we are able to make an approximation around these closing points, as we did previously for the Haldane model.

Below, we summarize the expansions around the relevant gap closings:

$\overrightarrow{\mathbf{k}}_0 = \left(k_x^0, k_y^0\right)$	Expansion	Phase transition point
$(0,0)$	$H \approx \kappa_x\sigma_x + \kappa_y\sigma_y + (M-2)\,\sigma_z$	$M = 2$
$(0,\pi)$	$H \approx \kappa_x\sigma_x - \kappa_y\sigma_y + M\sigma_z$	$M = 0$
$(\pi,0)$	$H \approx -\kappa_x\sigma_x + \kappa_y\sigma_y + M\sigma_z$	$M = 0$
(π,π)	$H \approx -\kappa_x\sigma_x - \kappa_y\sigma_y + (M+2)\,\sigma_z$	$M = -2$

where $\kappa_x = k_x - k_x^0$ and $\kappa_y = k_y - k_y^0$. We can write these expansions in the same form as 2.22 by noting that they all have similar forms and that the term multiplying σ_z is the band gap Δ.

$$\tilde{H} \approx s_x\kappa_x\sigma_x + s_y\kappa_y\sigma_y + \Delta\sigma_z, \tag{2.24}$$

where $s_x, s_y = \pm 1$, and so

$$\tilde{h}\left(k_x, k_y\right) \approx \left(s_x\kappa_x, s_y\kappa_y, \Delta\right). \tag{2.25}$$

As is shown in Appendix C.2, for two band Hamiltonians of the type $\overrightarrow{\mathbf{h}}\cdot\sigma$ the Chern number can be computed through [24]

$$C = \frac{1}{4\pi}\int_{BZ}\frac{1}{h^3}\left(\frac{\partial\overrightarrow{\mathbf{h}}}{\partial k_x}\times\frac{\partial\overrightarrow{\mathbf{h}}}{\partial k_y}\right)\cdot\overrightarrow{\mathbf{h}}\,dk_x dk_y. \tag{2.26}$$

In our case this becomes

$$\begin{gathered} C = \tfrac{1}{4\pi}\int\frac{\Delta s_x s_y}{\left(\kappa_x^2+\kappa_y^2+\Delta^2\right)^{3/2}}d\kappa_x d\kappa_y \\ = \tfrac{\Delta s_x s_y}{4\pi}\int\frac{\kappa}{\left(\kappa^2+\Delta^2\right)^{3/2}}d\kappa d\theta, \quad \kappa = \sqrt{\kappa_x^2+\kappa_y^2}, \theta = \arctan\left(\tfrac{\kappa_y}{\kappa_x}\right) \\ = \tfrac{\Delta s_x s_y}{2}\int\frac{\kappa}{\left(\kappa^2+\Delta^2\right)^{3/2}}d\kappa \end{gathered}. \tag{2.27}$$

If we now integrate this up to a radius η we consider small in order for our approximation to be valid we obtain

$$\begin{gathered} C = \tfrac{\Delta s_x s_y}{4}\int_0^{\eta^2}\frac{1}{\left(u+\Delta^2\right)^{3/2}}du \\ C = -\tfrac{\Delta s_x s_y}{2}\left(u+\Delta^2\right)^{-1/2}\Big|_0^{\eta^2} = \tfrac{s_x s_y}{2}\left(-\frac{\Delta}{\sqrt{\Delta^2+\eta^2}}+\frac{\Delta}{|\Delta|}\right) \end{gathered}. \tag{2.28}$$

The first term vanishes as $\Delta/\eta \to 0$. Then, we are left only with

$$C = \frac{s_x s_y}{2}\mathrm{sign}\left(\Delta\right). \tag{2.29}$$

We can now calculate the values of the Chern number in each phase of the system.

- In the limit $M \to \pm\infty$ we are in a trivial insulator phase, since $\overrightarrow{\mathbf{h}} = (0, 0, \pm 1)$ and 2.26 yields 0 in this case.

- The first phase transition, coming from $M = -\infty$ is at $M = -2$. Here we just have to compute the difference between the Chern numbers for $M < -2$ and $M > -2$. For $M = -2$ we have the contribution of Dirac point (π, π), for which $\Delta = M + 2$, and $s_x = s_y = -1$. Using that

$$\operatorname{sgn}(\Delta) = \begin{cases} -1 & , M < -2 \\ 1 & , M > -2 \end{cases}, \tag{2.30}$$

we have

$$\begin{cases} C_- = -\frac{1}{2} & , M < -2 \\ C_+ = \frac{1}{2} & , M > -2 \end{cases}. \tag{2.31}$$

This implies that the Chern number in the region $-2 < M < 0$ (phase I) will be given by

$$C_I = C_{-\infty} + \Delta C = 1 \tag{2.32}$$

where $\Delta C = C_+ - C_- = 1$ and $C_{-\infty} = 0$ is the Chern number for $M = -\infty$.

- After this, we have a transition at $M = 0$. In this case we will have two contributions from the points $(0, \pi)$ and $(\pi, 0)$. For both these points $M = 0$ and $s_x s_y = -1$, meaning they will yield the same values for C_- and C_+:

$$\begin{cases} C_-^{(0,\pi)} = C_-^{(\pi,0)} = \frac{1}{2} & , M < 0 \\ C_+^{(0,\pi)} = C_+^{(\pi,0)} = -\frac{1}{2} & , M > 0 \end{cases}. \tag{2.33}$$

$$C_{II} = C_I + \Delta C^{(0,\pi)} + \Delta C^{(\pi,0)} = 1 - 2 = -1, \tag{2.34}$$

where we used $\Delta C^{(0,\pi)} = \Delta C^{(\pi,0)} = -1$.

And so, the topological invariant in the region $0 < M < 2$ (phase II) will be:

$$C_{II} = C_I + 2(C_+ - C_-) = 1 - 2 = -1. \tag{2.35}$$

The next transition would be at $M = 2$, so we could apply the same procedure as before to determine the Chern number for $M > 2$, however, we have already concluded that the system must be a trivial insulator ($C = 0$).

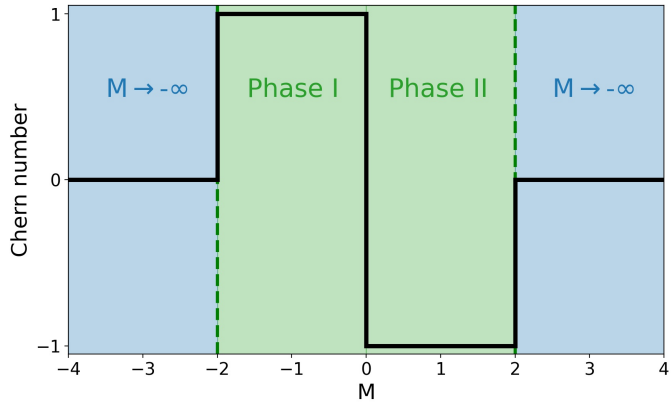

Figure 2.7.: Diagram of the topological phases for the square model. In green we represent the two topological phases and in blue we represent the values of M for which our system is a trivial insulator.

As we have mentioned previously, we will need to work with an Hamiltonian written in real space for the purposes of computing quantities of interest when our system is subject to an incommensurate potential. In the following lines we obtain the matrix elements of our Hamiltonian in real space.

We can write the Hamiltonian as

$$\begin{aligned} H = \sum_{\vec{\mathbf{k}}} & \left[M - t\cos(k_x) - t\cos(k_y)\right] c^{\dagger}_{\vec{\mathbf{k}}\,A} c_{\vec{\mathbf{k}}\,A} - \left[M - t\cos(k_x) - t\cos(k_y)\right] c^{\dagger}_{\vec{\mathbf{k}}\,B} c_{\vec{\mathbf{k}}\,B} \\ & + \left[\sin(k_x) - i\sin(k_y)\right] c^{\dagger}_{\vec{\mathbf{k}}\,B} c_{\vec{\mathbf{k}}\,A} + \left[\sin(k_x) + i\sin(k_y)\right] c^{\dagger}_{\vec{\mathbf{k}}\,A} c_{\vec{\mathbf{k}}\,B} \end{aligned} . \tag{2.36}$$

We can calculate the Berry curvature and obtain the expected results in Figure 2.8

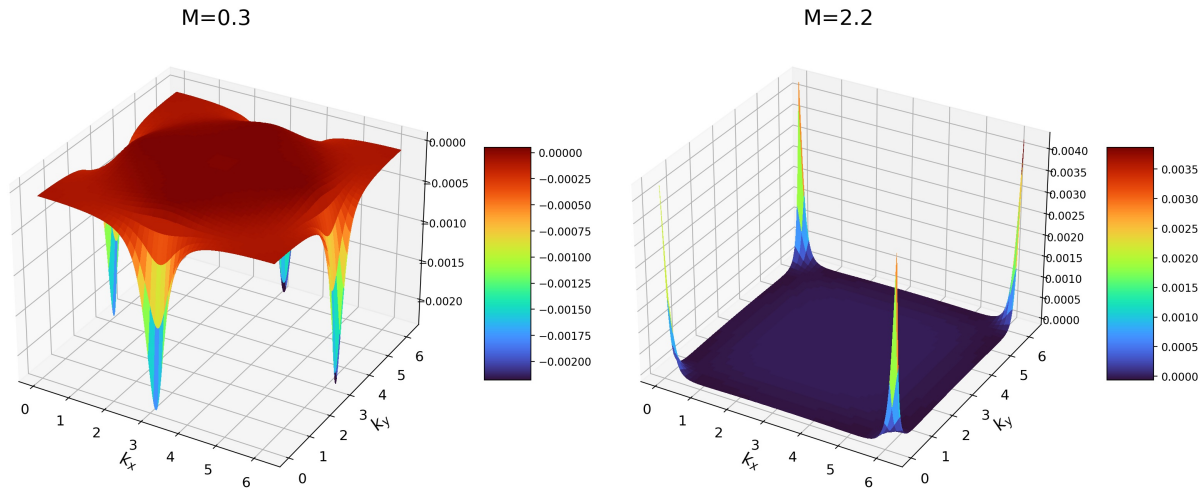

Figure 2.8.: Berry curvature of the Square model for values of M in the vicinity of two distinct transitions. Note the concentration of Berry curvature at the Dirac points as one approaches the transition point.

Now we can calculate the Fourier transform of this expression by writing

$$\begin{aligned} c^\dagger_{\vec{\mathbf{k}}\sigma} &= \frac{1}{\sqrt{N}} \sum_{\vec{\mathbf{R}}} e^{i\vec{\mathbf{k}}\cdot\vec{\mathbf{R}}} c^\dagger_{\vec{\mathbf{R}}\sigma} \\ c_{\vec{\mathbf{k}}\sigma} &= \frac{1}{\sqrt{N}} \sum_{\vec{\mathbf{R}}} e^{-i\vec{\mathbf{k}}\cdot\vec{\mathbf{R}}} c_{\vec{\mathbf{R}}\sigma} \end{aligned} . \tag{2.37}$$

We obtain for the first term

$$\begin{aligned} &\sum_{\vec{\mathbf{k}}} [M - t\cos(k_x) - t\cos(k_y)] \frac{1}{N} \sum_{\vec{\mathbf{R}}\vec{\mathbf{R}}'} e^{i\vec{\mathbf{k}}\cdot\vec{\mathbf{R}}} e^{-i\vec{\mathbf{k}}\cdot\vec{\mathbf{R}}'} c^\dagger_{RA} c_{R'A} \\ &= \frac{1}{N} \sum_{\vec{\mathbf{k}}} \sum_{\vec{\mathbf{R}}\vec{\mathbf{R}}'} [M e^{i\vec{\mathbf{k}}\cdot(\vec{\mathbf{R}}-\vec{\mathbf{R}}')} - t\cos(k_x) e^{i\vec{\mathbf{k}}\cdot(\vec{\mathbf{R}}-\vec{\mathbf{R}}')} - t\cos(k_y) e^{i\vec{\mathbf{k}}\cdot(\vec{\mathbf{R}}-\vec{\mathbf{R}}')}] c^\dagger_{RA} c_{R'A} \\ &= \frac{1}{N} \sum_{\vec{\mathbf{k}}} \sum_{\vec{\mathbf{R}}\vec{\mathbf{R}}'} [M e^{i\vec{\mathbf{k}}\cdot(\vec{\mathbf{R}}-\vec{\mathbf{R}}')} - t\left(\frac{e^{i\vec{\mathbf{k}}\cdot\hat{\boldsymbol{x}}} + e^{-i\vec{\mathbf{k}}\cdot\hat{\boldsymbol{x}}}}{2}\right) e^{i\vec{\mathbf{k}}\cdot(\vec{\mathbf{R}}-\vec{\mathbf{R}}')} - t\left(\frac{e^{i\vec{\mathbf{k}}\cdot\hat{\boldsymbol{y}}} + e^{-i\vec{\mathbf{k}}\cdot\hat{\boldsymbol{y}}}}{2}\right) e^{i\vec{\mathbf{k}}\cdot(\vec{\mathbf{R}}-\vec{\mathbf{R}}')}] c^\dagger_{RA} c_{R'A} \end{aligned} . \tag{2.38}$$

We now use $\frac{1}{N}\sum_{\vec{\mathbf{k}}}\sum_{\vec{\mathbf{R}}} e^{i\vec{\mathbf{k}}\cdot\vec{\mathbf{R}}} = \delta(\vec{\mathbf{R}})$, and obtain

$$\sum_{\vec{\mathbf{R}}} \left[M c^\dagger_{\vec{\mathbf{R}}A} c_{RA} - \frac{t}{2} \left(c^\dagger_{\vec{\mathbf{R}}A} c_{\vec{\mathbf{R}}-\hat{\boldsymbol{x}}A} + c^\dagger_{\vec{\mathbf{R}}A} c_{\vec{\mathbf{R}}+\hat{\boldsymbol{x}}A} + c^\dagger_{\vec{\mathbf{R}}A} c_{\vec{\mathbf{R}}-\hat{\boldsymbol{y}}A} + c^\dagger_{\vec{\mathbf{R}}A} c_{\vec{\mathbf{R}}+\hat{\boldsymbol{y}}A} \right) \right] . \tag{2.39}$$

The same calculation yields for the BB term

$$-\sum_{\vec{\mathbf{R}}}\left[Mc^{\dagger}_{\vec{\mathbf{R}}B}c_{\vec{\mathbf{R}}B}-\frac{t}{2}\left(c^{\dagger}_{\vec{\mathbf{R}}B}c_{\vec{\mathbf{R}}-\hat{\boldsymbol{x}}B}+c^{\dagger}_{\vec{\mathbf{R}}B}c_{\vec{\mathbf{R}}+\hat{\boldsymbol{x}}B}+c^{\dagger}_{\vec{\mathbf{R}}B}c_{\vec{\mathbf{R}}-\hat{\boldsymbol{y}}B}+c^{\dagger}_{\vec{\mathbf{R}}B}c_{\vec{\mathbf{R}}+\hat{\boldsymbol{y}}B}\right)\right]. \tag{2.40}$$

The cross-term AB is given by

$$\begin{aligned}
&\frac{1}{N}\sum_{\vec{\mathbf{k}}}\left[\sin(k_x)-i\sin(k_y)\right]\sum_{\vec{\mathbf{R}}\vec{\mathbf{R}'}}e^{i\vec{\mathbf{k}}\cdot\vec{\mathbf{R}}}e^{-i\vec{\mathbf{k}}\cdot\vec{\mathbf{R}}'}c^{\dagger}_{\vec{\mathbf{R}}A}c_{\vec{\mathbf{R}'}B}\\
&=\frac{1}{N}\sum_{\vec{\mathbf{k}}}\sum_{\vec{\mathbf{R}}\vec{\mathbf{R}'}}\left[\frac{1}{2i}\left(e^{ik_x}-e^{ik_x}\right)-\frac{1}{2}\left(e^{ik_y}-e^{ik_y}\right)\right]e^{i\vec{\mathbf{k}}\cdot\vec{\mathbf{R}}}e^{-i\vec{\mathbf{k}}\cdot\vec{\mathbf{R}}'}c^{\dagger}_{\vec{\mathbf{R}}A}c_{\vec{\mathbf{R}'}B} \qquad .\\
&=\sum_{\vec{\mathbf{R}}}\frac{1}{2i}\left(c^{\dagger}_{\vec{\mathbf{R}}A}c_{\vec{\mathbf{R}}-\hat{\boldsymbol{x}}B}-c^{\dagger}_{\vec{\mathbf{R}}A}c_{\vec{\mathbf{R}}+\hat{\boldsymbol{x}}B}\right)-\frac{1}{2}\left(c^{\dagger}_{\vec{\mathbf{R}}A}c_{\vec{\mathbf{R}}-\hat{\boldsymbol{y}}B}-c^{\dagger}_{\vec{\mathbf{R}}A}c_{\vec{\mathbf{R}}+\hat{\boldsymbol{y}}B}\right)
\end{aligned} \tag{2.41}$$

Combining all the terms we obtain the following Hamiltonian

$$\begin{aligned}
H=\sum_{\vec{\mathbf{R}}}\{&\frac{1}{2i}\left(c^{\dagger}_{\vec{\mathbf{R}}A}c_{\vec{\mathbf{R}}-\hat{\boldsymbol{x}}B}-c^{\dagger}_{\vec{\mathbf{R}}A}c_{\vec{\mathbf{R}}+\hat{\boldsymbol{x}}B}\right)-\frac{1}{2}\left(c^{\dagger}_{\vec{\mathbf{R}}A}c_{\vec{\mathbf{R}}-\hat{\boldsymbol{y}}B}-c^{\dagger}_{\vec{\mathbf{R}}A}c_{\vec{\mathbf{R}}+\hat{\boldsymbol{y}}B}\right)+h.c.+\\
+\sum_{\sigma}\xi_{\sigma}&\left[Mc^{\dagger}_{\vec{\mathbf{R}}\sigma}c_{\vec{\mathbf{R}}\sigma}-\frac{t}{2}\left(c^{\dagger}_{\vec{\mathbf{R}}\sigma}c_{\vec{\mathbf{R}}-\hat{\boldsymbol{x}}\sigma}+c^{\dagger}_{\vec{\mathbf{R}}\sigma}c_{\vec{\mathbf{R}}+\hat{\boldsymbol{x}}\sigma}+c^{\dagger}_{\vec{\mathbf{R}}\sigma}c_{\vec{\mathbf{R}}-\hat{\boldsymbol{y}}\sigma}+c^{\dagger}_{\vec{\mathbf{R}}\sigma}c_{\vec{\mathbf{R}}+\hat{\boldsymbol{y}}\sigma}\right)\right]\}
\end{aligned} \tag{2.42}$$

where $\xi_A=-\xi_B=1$.

We can see that in real space this is quite a complicated Hamiltonian with broken time-reversal symmetry. The unit cell in real-space is schematticaly represented below:

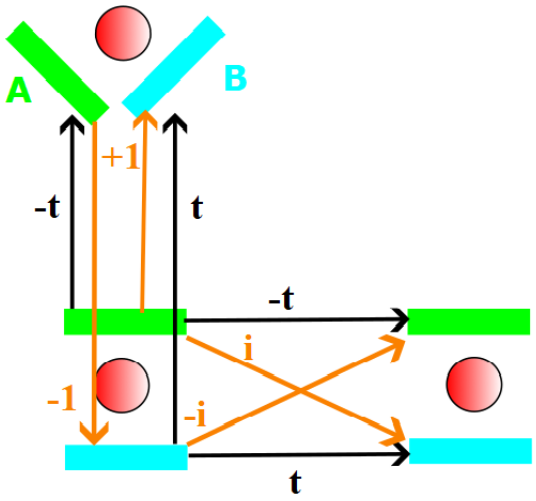

Figure 2.9.: Schematic representation of the unit lattice of the model on the square lattice.

2.3. Incommensurate potential and approximants

The goal of this thesis is to study the effects of quasi-periodic potentials in two-dimensional systems. To achieve this we will here introduce and detail the incommensurate potentials studied throughout this work.

2.3.1. Incommensurate potential

We have mentioned before, in the Motivation section of this document, that these systems we study can be used to study TBLG [42,43] since they are both described by a Moiré pattern, that is, a pattern formed by the superimposition of two patterns. We can see in Figure 2.10 examples of these Moiré patterns

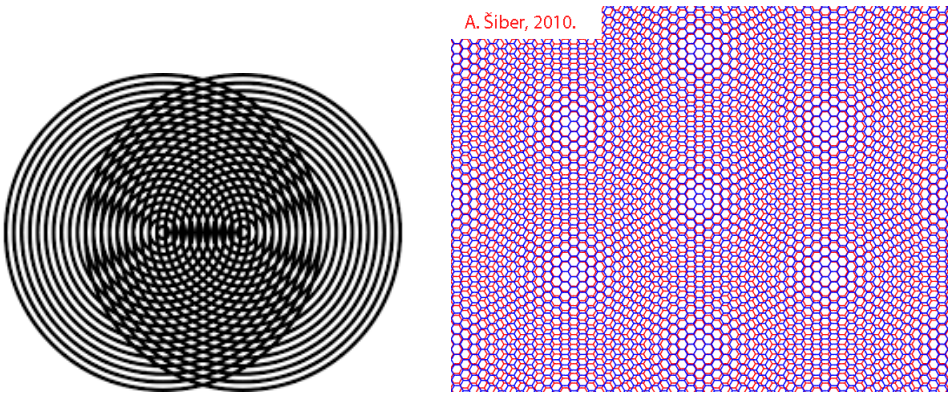

Figure 2.10.: (left) Moiré pattern emergent from the superposition of two sets of concentric circles. (right) Moiré pattern resulting from the superposition of two honeycomb lattices. It is obvious that this emergent pattern has an inherent periodicity.

We see in a) that from the overlay of two patterns in the center, a new one emerges with its own features. In Figure b) we see how this is conceived in the case of TBLG, through relative rotation of two layers of graphene. Another possible way in which a Moiré pattern can emerge is when a given lattice experiences a potential whose wavelength is different from the lattice constant. The case we are interested in is the case in which the periodicity of this Moiré pattern is infinite, and the two patterns are said to be incommensurate with one another. We can achieve this by making it so the periodicity of the potential is an irrational mutiple of the periodicity of our lattice.

2.3.2. Implementation of quasi-periodic potential in 2D systems

As was mentioned previously, our Moiré structure will arise from the superposition of a quasi-periodic potential on the underlying lattice. This will lead to a new Hamiltonian of the form

$$H = H_0 + V_{\text{qp}}. \tag{2.43}$$

Where H_0 is the Hamiltonian that describes our system in the absence of any quasi-disorder. The quasi-periodic potential V_{qp} will have the form

$$V_{\text{qp}}\left(\vec{\mathbf{r}}\right) = V_0 \sum_{\vec{\mathbf{b}}_i} \cos\left(\beta\left(\vec{\mathbf{r}} - \vec{\mathbf{r}}_0\right) \cdot \vec{\mathbf{b}}_i\right), \tag{2.44}$$

with $\vec{\mathbf{b}}_i = \left\{\vec{\mathbf{b_1}}, \vec{\mathbf{b_2}}\right\}$, with $\vec{\mathbf{b}}_1$ and $\vec{\mathbf{b}}_2$ being the primitive vectors of the reciprocal lattice in real space, and $\vec{\mathbf{r}}_0$ is a shift in the center of the incommensurate potential.

2.3.3. The golden ratio and approximants

The chosen irrational number was the golden ratio $\varphi = \frac{1+\sqrt{5}}{2} \approx 1.618....$

In order to actually perform numerical calculations in these incommensurate systems we need a way to cope with the infinte unit cell. What we do is to consider a so-called supercell that is simply the lattice we are studying with a periodic potential superimposed, such that the periodicity of this potential is equal to the size of the supercell.

To perform this we must be able to approximate our golden ratio by an rational number p/q and q will be the periodicity of this potential. Fortunately, there is a well-known approximation of this number using the Fibonacci sequence which goes like

$$1, 1, 2, 3, 5, 8, 13, 21, 34, 55, 89, \ldots \tag{2.45}$$

where the nth number of the sequence is obtained by the relation $f_n = f_{n-2} + f_{n-1}$. The golden ratio is then approximated by the ratio between consecutive Fibonacci numbers.

We can therefore do calculations with increasing size of the system and increasing convergence to φ.

3. Methods

The object of this work includes the calculation of quite complex quantities in systems that are further complicated by the introduction of disorder. We employ, for example, spectral methods in order to compute the density of states, and the coupling matrix method in order to obtain the topological invariant. Our hope was to perform these operations in the swiftest and most efficient way, and of great assistance in this endeavour were the various Python packages such as *numpy* and *scipy*.

3.1. Coupling matrix method

As aforementioned, in systems where we have broken translation symmetry we can no longer use the wave vector as a good quantum number. We must consequently develop alternative methods to calculate the Chern number for such systems. One of these methods is described in Ref. [63], and is used throughout the entirety of this work.

We consider a system with a Hamiltonian H with eigenstates $|\phi_n\rangle$ where n is the band index. If the system depends on a set of parameters $\overrightarrow{\mathbf{R}}$ we can write the usual expression for the Chern number as:

$$C_n = \frac{1}{2\pi} \int_{\mathcal{S}} d\overrightarrow{\mathbf{S}} \cdot \Omega^{(n)} \left(\overrightarrow{\mathbf{R}} \right). \tag{3.1}$$

For a system that is periodic in $\overrightarrow{\mathbf{R}}$, $\mathcal{S}$ can be identified with the unit cell of the system.

We must begin by considering a two-dimensional lattice with $N = L_x \times L_y$ unit cells. We can define twisted boundary conditions as

$$\begin{aligned} \phi_n^\theta \left(x + L_x, y \right) &\equiv \left\langle x + L_x, y \mid \phi_n^\theta \right\rangle = \phi_n^\theta \left(x, y \right) e^{i\theta_x} \\ \phi_n^\theta \left(x, y + L_y \right) &\equiv \left\langle L_x, y + L_y \mid \phi_n^\theta \right\rangle = \phi_n^\theta \left(x, y \right) e^{i\theta_y} \end{aligned}, \tag{3.2}$$

with $0 \leq \theta_x, \theta_y \leq 2\pi$.

We wish to calculate the Chern number using the many-body wavefunction $\Psi_\theta \left(\{ \overrightarrow{\mathbf{r}}_i \} \right)$, where $\overrightarrow{\mathbf{r}}_i$ is the coordinate of the i-th electron. This wave function can be written as the Slater determinant of the single-particle wavefunctions $\phi_\theta^n \left(\overrightarrow{\mathbf{r}}_i \right)$

$$\left|\Psi^{\theta}\right\rangle = \prod_{n=1}^{M} \phi_n^{\dagger}(\theta)\left|0\right\rangle, \tag{3.3}$$

where M is the number of occupied states and we define $\left|\phi_n^{\theta}\right\rangle = \phi_n^{\dagger}(\theta)\left|0\right\rangle$. What we now want to calculate is the Berry connection (1.5) with θ being the parameter $\vec{\mathbf{R}}$ that varies our Hamiltonian. Thus, we write

$$C = \frac{1}{2\pi}\int_{\partial S} d\vec{\mathbf{l}}_{\theta} \cdot \left\langle \Psi^{\theta} \mid i\nabla_{\theta}\Psi^{\theta}\right\rangle. \tag{3.4}$$

where $\vec{\mathbf{l}}_{\theta}$ is the displacement in θ-space. We can now write a discrete and numerically suitable expression for the integrand in the above expression. First we consider a path $\gamma(\theta)$ that parametrizes the boundary of the surface $\mathcal{S}_{\theta}$. Then we create a discretization of this path, transforming the continuum of states into a grid of states separated by vectors $\Delta\vec{\mathbf{l}}$, as shown in Figure 3.1.

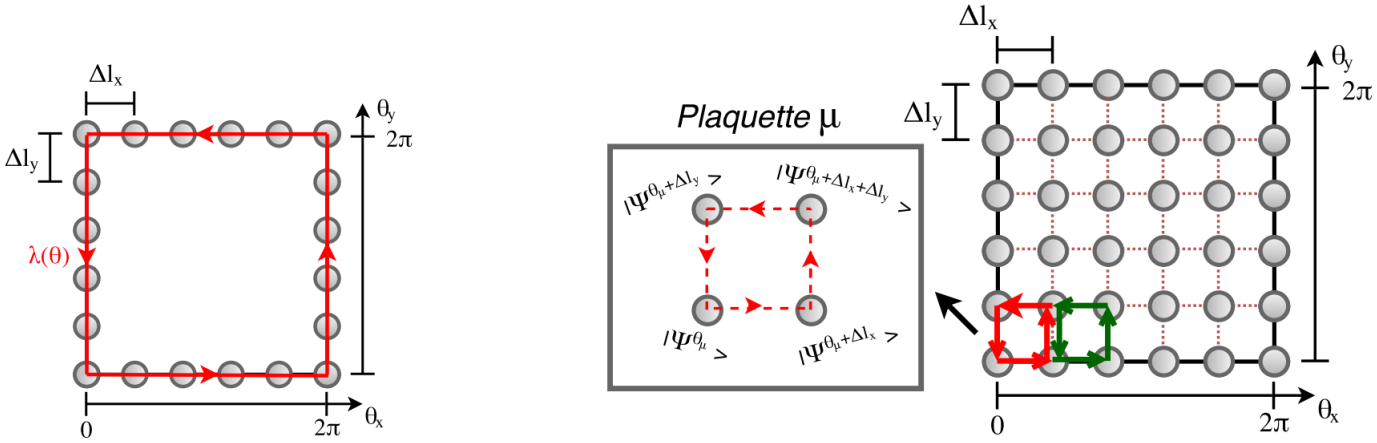

Figure 3.1.: (left) Discretization of the boundary of surface $\mathcal{S}$ into points separated by distances Δl_x and Δl_y. (right) Discretization of surface $\mathcal{S}$ into small plaquettes. The sum of the flux over this plaquettes yields only the flux along the boundary.

We now note that, up to first order in the separation $\Delta\vec{\mathbf{l}}$

$$\Delta\vec{\mathbf{l}}_{\theta} \cdot \left\langle \Psi^{\theta} \mid i\nabla_{\theta}\Psi^{\theta}\right\rangle \approx \ln\left[1 + \Delta\vec{\mathbf{l}}_{\theta} \cdot \left\langle \Psi^{\theta} \mid i\nabla_{\theta}\Psi^{\theta}\right\rangle\right] = \ln\left[\left\langle \Psi^{\theta}\right| \left(\left|\Psi^{\theta}\right\rangle + i\Delta\vec{\mathbf{l}}_{\theta} \cdot \left|\nabla_{\theta}\Psi^{\theta}\right\rangle\right)\right]. \tag{3.5}$$

Again up to first order in $\Delta\vec{\mathbf{l}}$ we can write $\left|\Psi^{\theta}\right\rangle + i\Delta\vec{\mathbf{l}}_{\theta} \cdot \left|\nabla_{\theta}\Psi^{\theta}\right\rangle \approx \left|\Psi^{\theta+\Delta\vec{\mathbf{l}}}\right\rangle$.

Hence, we have written a succint expression for the quantity we wish to compute in terms of overlaps between many-body wavefunctions separated by a vector $\Delta\overrightarrow{\mathbf{l}}$ in the θ parameter space $\left\langle \Psi^{\theta} \mid \Psi^{\theta+\Delta\overrightarrow{\mathbf{l}}} \right\rangle$. In Appendix A we showed that the quantity $\left\langle n_{\overrightarrow{\mathbf{R}}} \mid \nabla_{\overrightarrow{\mathbf{R}}} n_{\overrightarrow{\mathbf{R}}} \right\rangle$ is pure imaginary and we need only consider its imaginary part. If we write the so-called link variable as $z = |z|\, e^{i \arg(z)}$ we obtain

$$\Delta\overrightarrow{\mathbf{l}}_{\theta} \cdot \left\langle \Psi^{\theta} \mid \nabla_{\theta} \Psi^{\theta} \right\rangle = i\Im\left[\ln\left[\left\langle \Psi^{\theta} \mid \Psi^{\theta+\Delta\overrightarrow{\mathbf{l}}} \right\rangle\right]\right] = \arg\left(\left\langle \Psi^{\theta} \mid \Psi^{\theta+\Delta\overrightarrow{\mathbf{l}}} \right\rangle\right). \tag{3.6}$$

For small enough $\Delta\overrightarrow{\mathbf{l}}$ we can calculate C by calculating these successive overlaps around the path $\gamma(\theta)$. The now discrete expression becomes

$$C = \frac{1}{2\pi}\int_{\partial S} d\overrightarrow{\mathbf{l}}_{\theta} \cdot \left\langle \Psi^{\theta} \mid i\nabla_{\theta} \Psi^{\theta} \right\rangle \rightarrow C = -\frac{1}{2\pi}\sum_{n} \arg\left(\left\langle \Psi^{\theta_n} \mid \Psi^{\theta_{n+1}} \right\rangle\right) = -\frac{1}{2\pi}\arg\left(\prod_{n}\left\langle \Psi^{\theta_n} \mid \Psi^{\theta_{n+1}} \right\rangle\right). \tag{3.7}$$

Where $\theta_{n+1} = \theta_n + \Delta\overrightarrow{\mathbf{l}}_n$. In order to calculate the link variables $\left\langle \Psi^{\theta_n} \mid \nabla_{\theta} \Psi^{\theta_{n+1}} \right\rangle$ we write the eigenstates $\left\{\left|\phi_n^{\theta}\right\rangle\right\}$ in the basis of positions $\{|\overrightarrow{\mathbf{r}}_i\rangle\}$

$$\left|\phi_n^{\theta}\right\rangle = \sum_{\overrightarrow{\mathbf{r}}_i} \eta^{n,\theta}_{\overrightarrow{\mathbf{r}}_i} |\overrightarrow{\mathbf{r}}_i\rangle\,. \tag{3.8}$$

The link variables are given by the Slater determinant

$$\left\langle \Psi^{\theta_n} \mid \nabla_{\theta} \Psi^{\theta_{n+1}} \right\rangle = \det\left[\Phi^{\dagger}_{\theta_n} \Phi_{\theta_{n+1}}\right], \tag{3.9}$$

with

$$\Phi_{\theta_n} = \begin{pmatrix} \eta^{1,\theta}_{\overrightarrow{\mathbf{r}}_1} & \eta^{2,\theta}_{\overrightarrow{\mathbf{r}}_1} & \cdots & \eta^{M,\theta}_{\overrightarrow{\mathbf{r}}_1} \\ \eta^{1,\theta}_{\overrightarrow{\mathbf{r}}_2} & \eta^{2,\theta}_{\overrightarrow{\mathbf{r}}_2} & \cdots & \eta^{M,\theta}_{\overrightarrow{\mathbf{r}}_2} \\ \vdots & \vdots & \ddots & \vdots \\ \eta^{1,\theta}_{\overrightarrow{\mathbf{r}}_M} & \eta^{2,\theta}_{\overrightarrow{\mathbf{r}}_M} & \cdots & \eta^{M,\theta}_{\overrightarrow{\mathbf{r}}_M} \end{pmatrix}. \tag{3.10}$$

This being determined, we have all the ingredients required to perform the computation of the Chern number. If we divide the surface $\mathcal{S}_{\theta}$ into $N_x N_y$ plaquettes we can calculate the contribution to the total Chern number of each plaquette and then add them all up. This method also has the advantage that the contribution from each plaquette is manifestly gauge invariant. The contribution of one plaquette is given by

$$C_\mu = -\frac{1}{2\pi}\arg\left(\left\langle \Psi^{\theta_\mu} \mid \Psi^{\theta_\mu+\Delta l_x}\right\rangle\left\langle \Psi^{\theta_\mu+\Delta l_x} \mid \Psi^{\theta_\mu+\Delta l_x+\Delta l_y}\right\rangle\left\langle \Psi^{\theta_\mu+\Delta l_x+\Delta l_y} \mid \Psi^{\theta_\mu+\Delta l_y}\right\rangle\left\langle \Psi^{\theta_\mu+\Delta l_y} \mid \Psi^{\theta_\mu}\right\rangle\right)$$
$$= -\frac{1}{2\pi}\arg\det\left(\Phi^\dagger_{\theta_\mu}\Phi_{\theta_\mu+\Delta l_x}\Phi^\dagger_{\theta_\mu+\Delta l_x}\Phi_{\theta_\mu+\Delta l_x+\Delta l_y}\Phi^\dagger_{\theta_\mu+\Delta l_x+\Delta l_y}\Phi_{\theta_\mu+\Delta l_y}\Phi^\dagger_{\theta_\mu+\Delta l_y}\Phi_{\theta_\mu}\right) = -\frac{1}{2\pi}\arg\det\left(\Phi^\mu_{pl}\right). \tag{3.11}$$

The simplest way to evaluate this would be to diagonalize Φ^μ_{pl} and calculate its determinant as the sum of its eigenvalues. Thus,

$$C_\mu = -\frac{1}{2\pi}\sum_{p=1}^{M}\arg\left(\lambda_p\right). \tag{3.12}$$

Withal, the accuracy of this method is shadowed by the rather cumbersome calculations needed to perform. We would need to diagonalize $M \times M$ matrices $N_x N_y$ times. There is, nevertheless, an alternative method that requires only one diagonalization.

We can now do a Fourier transform from real space to momentum space in order to obtain

$$\eta^{n,\theta}_{\overrightarrow{\mathbf{r}}_i} = \frac{1}{\sqrt{N}}\sum_{\overrightarrow{\mathbf{k}}_i} F^n\left(\overrightarrow{\mathbf{k}}_i\right) e^{i\overrightarrow{\mathbf{k}}_i\cdot\overrightarrow{\mathbf{r}}_i}. \tag{3.13}$$

Twisted boundary conditions require that

$$\begin{aligned}\overrightarrow{\mathbf{k}}_i\cdot(\overrightarrow{\mathbf{r}}_i + L_x\hat{x}) &= \overrightarrow{\mathbf{k}}_i\cdot\overrightarrow{\mathbf{r}}_i + \theta_x\\ \overrightarrow{\mathbf{k}}_i\cdot(\overrightarrow{\mathbf{r}}_i + L_y\hat{y}) &= \overrightarrow{\mathbf{k}}_i\cdot\overrightarrow{\mathbf{r}}_i + \theta_y\end{aligned}. \tag{3.14}$$

This gives us a condition for $\overrightarrow{\mathbf{k}}_i$

$$\overrightarrow{\mathbf{k}}_i = \overrightarrow{\mathbf{k}}^{(0)}_i + \overrightarrow{\mathbf{q}}, \tag{3.15}$$

where $\overrightarrow{\mathbf{k}}^{(0)}_i = \left(\frac{2n\pi}{L_x}, \frac{2m\pi}{L_y}\right)$ is the usual discrete momenta of periodic boundary conditions, and

$$\overrightarrow{\mathbf{q}} = \left(\frac{\theta_x}{L_x}, \frac{\theta_y}{L_y}\right). \tag{3.16}$$

Now we can write $F^n\left(\overrightarrow{\mathbf{k}}_i\right) = F^n_{\overrightarrow{\mathbf{q}}}\left(\overrightarrow{\mathbf{k}}^{(0)}_i\right)$. The overlaps can be written in terms of $\overrightarrow{\mathbf{q}}$ as

$$\left\langle \Psi^{\overrightarrow{\mathbf{q}}} \mid \Psi^{\overrightarrow{\mathbf{q}'}}\right\rangle = \det\left[\Phi^\dagger_{\overrightarrow{\mathbf{q}}}\Phi_{\overrightarrow{\mathbf{q}'}}\right], \tag{3.17}$$

with

$$\Phi_{\overrightarrow{\mathbf{q}}} = \begin{pmatrix} F^1_{\overrightarrow{\mathbf{q}}}\left(\overrightarrow{\mathbf{k}}^{(0)}_1\right) & F^2_{\overrightarrow{\mathbf{q}}}\left(\overrightarrow{\mathbf{k}}^{(0)}_1\right) & \cdots & F^M_{\overrightarrow{\mathbf{q}}}\left(\overrightarrow{\mathbf{k}}^{(0)}_1\right) \\ F^1_{\overrightarrow{\mathbf{q}}}\left(\overrightarrow{\mathbf{k}}^{(0)}_2\right) & F^2_{\overrightarrow{\mathbf{q}}}\left(\overrightarrow{\mathbf{k}}^{(0)}_2\right) & \cdots & F^M_{\overrightarrow{\mathbf{q}}}\left(\overrightarrow{\mathbf{k}}^{(0)}_2\right) \\ \vdots & \vdots & \ddots & \vdots \\ F^1_{\overrightarrow{\mathbf{q}}}\left(\overrightarrow{\mathbf{k}}^{(0)}_M\right) & F^2_{\overrightarrow{\mathbf{q}}}\left(\overrightarrow{\mathbf{k}}^{(0)}_M\right) & \cdots & F^M_{\overrightarrow{\mathbf{q}}}\left(\overrightarrow{\mathbf{k}}^{(0)}_M\right) \end{pmatrix}. \tag{3.18}$$

In a similar fashion as to what was performed previously, we can discretize the $\mathcal{S}_{\overrightarrow{\mathbf{q}}}$ surface into $N_x N_y$ plaquettes over the rectangle $\overrightarrow{\mathbf{q}} \in \left[0, \frac{2\pi}{L_x}\right] \times \left[0, \frac{2\pi}{L_y}\right]$. The Chern number contribution of each plaquette is, once again

$$\begin{aligned} C_\mu &= -\frac{1}{2\pi} \arg\left(\left\langle \Psi^{\overrightarrow{\mathbf{q}}_\mu} \mid \Psi^{\overrightarrow{\mathbf{q}}_\mu + \Delta l_x}\right\rangle \left\langle \Psi^{\overrightarrow{\mathbf{q}}_\mu + \Delta l_x} \mid \Psi^{\overrightarrow{\mathbf{q}}_\mu + \Delta l_x + \Delta l_y}\right\rangle \left\langle \Psi^{\overrightarrow{\mathbf{q}}_\mu + \Delta l_x + \Delta l_y} \mid \Psi^{\overrightarrow{\mathbf{q}}_\mu + \Delta l_y}\right\rangle \left\langle \Psi^{\overrightarrow{\mathbf{q}}_\mu + \Delta l_y} \mid \Psi^{\overrightarrow{\mathbf{q}}_\mu}\right\rangle\right) \\ &= -\frac{1}{2\pi} \arg\det\left(\Phi^\dagger_{\overrightarrow{\mathbf{q}}_\mu} \Phi_{\overrightarrow{\mathbf{q}} + \Delta l_x} \Phi^\dagger_{\overrightarrow{\mathbf{q}}_\mu + \Delta l_x} \Phi_{\overrightarrow{\mathbf{q}}_\mu + \Delta l_x + \Delta l_y} \Phi^\dagger_{\overrightarrow{\mathbf{q}}_\mu + \Delta l_x + \Delta l_y} \Phi_{\overrightarrow{\mathbf{q}}_\mu + \Delta l_y} \Phi^\dagger_{\overrightarrow{\mathbf{q}}_\mu + \Delta l_y} \Phi_{\overrightarrow{\mathbf{q}}_\mu}\right) \end{aligned} \tag{3.19}$$

At first glance this does not seem like much of an improvement, however, a more careful examination will show that for sufficiently large system sizes, considering a single plaquette will be a good approximation, since the distance between its corners decreases with $1/L$. Furthermore, the corners of this single plaquette belong to the set of allowed momenta for periodic boundary conditions. We now define

$$C^{mn}_{\overrightarrow{\mathbf{q}},\overrightarrow{\mathbf{q}'}} \equiv \Phi^\dagger_{\overrightarrow{\mathbf{q}}} \Phi_{\overrightarrow{\mathbf{q}'}}, \tag{3.20}$$

with matrix elements given by

$$C^{mn}_{\overrightarrow{\mathbf{q}},\overrightarrow{\mathbf{q}'}} = \sum_{\overrightarrow{\mathbf{k}}^{(0)}_i} \left[F^{m,\overrightarrow{\mathbf{q}}}_{\overrightarrow{\mathbf{k}}^{(0)}_i}\right]^* F^{n,\overrightarrow{\mathbf{q}'}}_{\overrightarrow{\mathbf{k}}^{(0)}_i}. \tag{3.21}$$

We can show that, since $F^{n,\overrightarrow{\mathbf{q}}}\left(\overrightarrow{\mathbf{k}}^{(0)}_i\right) = \frac{1}{\sqrt{N}} \sum_{\overrightarrow{\mathbf{r}}_i} \eta^{n,\theta}_{\overrightarrow{\mathbf{r}}_i} e^{-i\overrightarrow{\mathbf{k}}^{(0)}_i \cdot \overrightarrow{\mathbf{r}}_i}$,

$$\begin{aligned} C^{mn}_{\overrightarrow{\mathbf{q}},\overrightarrow{\mathbf{q}'}} &= \frac{1}{N} \sum_{\overrightarrow{\mathbf{k}}^{(0)}_i} \sum_{\overrightarrow{\mathbf{r}}_i} \left[\eta^{n,\theta=0}_{\overrightarrow{\mathbf{r}}_i}\right]^* e^{i\overrightarrow{\mathbf{k}}_i \cdot \overrightarrow{\mathbf{r}}_i} \sum_{\overrightarrow{\mathbf{r}'}_i} \eta^{m,\theta=0}_{\overrightarrow{\mathbf{r}'}_i} e^{-i\overrightarrow{\mathbf{k}}_i \cdot \overrightarrow{\mathbf{r}'}_i} \\ C^{mn}_{\overrightarrow{\mathbf{q}},\overrightarrow{\mathbf{q}'}} &= \frac{1}{N} \sum_{\overrightarrow{\mathbf{k}}^{(0)}_i} \sum_{\overrightarrow{\mathbf{r}}_i} \sum_{\overrightarrow{\mathbf{r}'}_i} \left[\eta^{n,\theta=0}_{\overrightarrow{\mathbf{r}}_i}\right]^* e^{i\left(\overrightarrow{\mathbf{k}}^{(0)}_i + \overrightarrow{\mathbf{q}} - \overrightarrow{\mathbf{q}'}\right) \cdot \left(\overrightarrow{\mathbf{r}}_i - \overrightarrow{\mathbf{r}'}_i\right)} \eta^{m,\theta=0}_{\overrightarrow{\mathbf{r}'}_i}, \\ C^{mn}_{\overrightarrow{\mathbf{q}},\overrightarrow{\mathbf{q}'}} &= \sum_{\overrightarrow{\mathbf{r}}_i} \left[\eta^{n,\theta=0}_{\overrightarrow{\mathbf{r}}_i}\right]^* e^{i\left(\overrightarrow{\mathbf{q}} - \overrightarrow{\mathbf{q}'}\right) \cdot \overrightarrow{\mathbf{r}}_i} \eta^{m,\theta=0}_{\overrightarrow{\mathbf{r}}_i} \end{aligned} \tag{3.22}$$

where $\left\{\eta^{n,\theta=0}_{\overrightarrow{\mathbf{r}}_i}\right\}$ is defined in equation 3.13. Thus, it is only necessary to compute the matrix elements of the coupling matrix using equation 3.22 for the corner momenta given by

$$\begin{aligned}\overrightarrow{\mathbf{q}}_0 &= (0,0)\\ \overrightarrow{\mathbf{q}}_1 &= (2\pi/L_x,0)\\ \overrightarrow{\mathbf{q}}_2 &= (2\pi/L_x,2\pi/L_y)\\ \overrightarrow{\mathbf{q}}_3 &= (0,2\pi/L_y)\end{aligned}. \tag{3.23}$$

After having calculated the matrix elements for the 4 matrices we define

$$\mathcal{F} = C_{\overrightarrow{\mathbf{q}}_0,\overrightarrow{\mathbf{q}}_1} C_{\overrightarrow{\mathbf{q}}_1,\overrightarrow{\mathbf{q}}_2} C_{\overrightarrow{\mathbf{q}}_2,\overrightarrow{\mathbf{q}}_3} C_{\overrightarrow{\mathbf{q}}_3,\overrightarrow{\mathbf{q}}_0}, \tag{3.24}$$

And our desired Chern number is given by

$$C = -\frac{1}{2\pi}\sum_{p}^{M} \arg\left(\lambda_p\right), \tag{3.25}$$

where $\{\lambda_p\}$ is the set of eigenvalues of matrix $\mathcal{F}$.

As an application, we can verify that the real-space Hamiltonian 2.2, calcualted for the square lattice model in section 2.2 is correct by using the coupling matrix method to calculate the topological invariant as a function of M and see if it reproduces the diagram shown in Figure 2.7. Indeed, we represent the results in Figure 3.2 and confirm that the results are coincident.

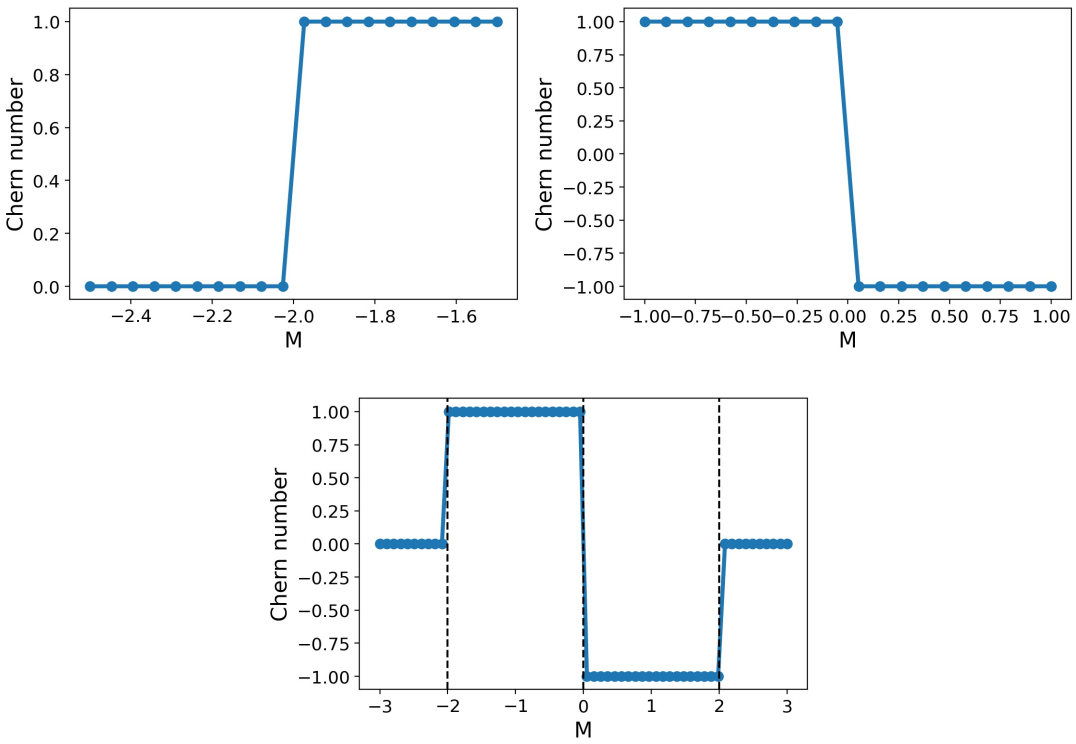

Figure 3.2.: Topological phase diagram for the model on the square lattice with $t = 1$ with varying value of M obtained using the coupling matrix method for the Hamiltonian in real space for a system with 120 sites.

3.2. The Kernel Polynomial Method

Throughout the work presented in this document it was necessary to calculate spectral properties of our systems, which have broken translational invariance. Of great importance to this end were spectral methods, specifically the Kernel Polynomial Method (KPM) [61]. Even though this method was independently implemented with success, the results presented in this document were obtained using KITE [25], an extremely powerful tool for real-space simulations electronic structure and quantum transport properties.

Consider the density of states (DoS). It is given by the following expression:

$$\rho(\varepsilon) = \frac{1}{N} \sum_n \delta(\varepsilon - \varepsilon_n), \tag{3.26}$$

where ε_n is the eigenvalue associated with the eigenvector $|n\rangle$ of the Hamiltonian that describes our system, and N is the dimension of the Hilbert space. In a situation where we have translation invariance we can calculate this DoS by diagonalizing our Hamiltonian. However,

when this is not the case we must employ alternative methods. First, we rewrite the previous expression as the trace of a matrix.

$$\rho(\varepsilon) = \frac{1}{N} Tr\left[\delta(\varepsilon - H)\right]. \tag{3.27}$$

What we now want to do is to expand $\delta(\varepsilon - H)$ in terms of Chebyshev polynomials as such

$$\delta(\varepsilon - H) = \sum_{n=0}^{\infty} \Delta_n(\varepsilon) T_n(H), \tag{3.28}$$

where $T_n(\varepsilon)$ is the Chebyshev polynomial of order n (see Appendix D.1). The reason for this is because these polynomials obey a simple recursion relation and are proved to be extremely useful due to their convergence properties. As was mentioned in Appendix D.1, these polynomials are only defined in the interval $]-1, 1[$. We must therefore rescale our energy spectrum in order to comply with this condition. We do this by performing these transformations

$$\tilde{H} = \frac{H - b}{a}, \quad \tilde{\varepsilon} = \frac{\varepsilon - b}{a}, \tag{3.29}$$

with

$$a = \frac{\varepsilon_{max} - \varepsilon_{min}}{2}, \quad b = \frac{\varepsilon_{max} + \varepsilon_{min}}{2}. \tag{3.30}$$

The calculation of the expansion coefficients $\Delta_n(\varepsilon)$ is done in Appendix D.2 yielding

$$\Delta_n(\varepsilon) = \frac{2}{\pi\sqrt{1-\varepsilon^2}} \frac{T_n(\varepsilon)}{1 + \delta_{n,0}}. \tag{3.31}$$

Therefore, our density of states can be expressed in the following terms:

$$\begin{aligned} \rho(\tilde{\varepsilon}) &= \frac{1}{N} Tr\left[\sum_{n=0}^{\infty} \Delta_n(\tilde{\varepsilon}) T_n\left(\tilde{H}\right)\right] \\ \rho(\tilde{\varepsilon}) &= \frac{2}{N\pi\sqrt{1-\varepsilon^2}} \sum_{n=0}^{\infty} \frac{T_n(\tilde{\varepsilon})}{1 + \delta_{n,0}} Tr\left[T_n\left(\tilde{H}\right)\right] \end{aligned}. \tag{3.32}$$

Since we are unfortunately limited by the finite quality of our computational resources, we cannot perform this calculation up to an infinte number of Chebyshev polynomials. We must therefore choose a finite cutoff N_{cheb} that will determine the precision of our approximation to the desired DoS. If one doesn't pay at the entrance, one must pay at the exit, and so our increased computational efficiency will be rewardad with what are called Gibbs oscillations which undermine the quality of our results. With the objective of mitigating these oscillations we can use so-called *kernels* in the expansion. There are a variety of kernels, each with its advantages and disadvantages, however the most commonly used throughout this work was the Jackson kernel, defined as

$$g_n^J = \frac{(N_{cheb} - n + 1)\cos\left(\frac{n\pi}{N_{cheb}+1}\right) + \sin\left(\frac{n\pi}{N_{cheb}+1}\right)\cot\left(\frac{\pi}{N_{cheb}+1}\right)}{N_{cheb}+1}. \tag{3.33}$$

This way, the expression to be evaluated becomes

$$\tilde{\rho}(\tilde{\varepsilon}) = \frac{2}{N\pi\sqrt{1-\varepsilon^2}} \sum_{n=0}^{N_{cheb}} \frac{T_n(\tilde{\varepsilon})\, g_n^J}{1+\delta_{n,0}} Tr\left[T_n\left(\tilde{H}\right)\right]. \tag{3.34}$$

This still is a rather cumbersome array of operations, the bottleneck being the evaluation of the traces of the $T_n\left(\tilde{H}\right)$ matrices. However, we can use what is called stochastic trace evaluation. For this we consider a random vector $|\xi\rangle$ defined in the entire Hilbert space with independent entries. What we can show is that

$$Tr[\mathcal{O}] = \langle\langle \xi | \mathcal{O} | \xi \rangle\rangle, \tag{3.35}$$

where $\langle\langle \xi | \mathcal{O} | \xi \rangle\rangle$ denotes the average of $\langle \xi | \mathcal{O} | \xi \rangle$ over random vectors. If we apply this to our expression for the DoS we obtain

$$\tilde{\rho}(\tilde{\varepsilon}) = \frac{2}{N\pi\sqrt{1-\varepsilon^2}} \sum_{n=0}^{N_{cheb}} \frac{T_n(\tilde{\varepsilon})\, g_n^J}{1+\delta_{n,0}} \left\langle\left\langle \xi \middle| T_n\left(\tilde{H}\right) \middle| \xi \right\rangle\right\rangle. \tag{3.36}$$

We call the quantity $\left\langle\left\langle \xi \middle| T_n\left(\tilde{H}\right) \middle| \xi \right\rangle\right\rangle \equiv \mu_n$. We can now adjust the number of random vectors N_R we use to perform the stochastic evaluation, however, we will see that in practice, for sufficiently large system sizes, this number will be very small in order to obtain a statistically significant result.

The computation of these moments μ_n is done by using the recurrence relations obeyed by the Chebyshev polynomials D.1. The algorithm follows:

$$\begin{aligned} |0\rangle &= |\xi\rangle \\ |1\rangle &= \tilde{H}|0\rangle \\ |n+1\rangle &= 2\tilde{H}|n\rangle - |n-1\rangle \end{aligned} \quad . \tag{3.37}$$

We now have all the ingredients to write the simple expression

$$\tilde{\rho}(\tilde{\varepsilon}) = \frac{1}{N} \sum_{n=0}^{N_{cheb}} p_n(\tilde{\varepsilon})\, \mu_n. \tag{3.38}$$

where $p_n(\tilde{\varepsilon})$ are the energy dependent coefficients of the expansion of $\tilde{\rho}(\tilde{\varepsilon})$. We now see the power of KPM. The greatest computational load is contained in the moments μ_n for which we have to apply the Hamiltonian N_{cheb} times. If our Hamiltonian is sparse each of these operations is of order $\mathcal{O}(N)$ which means an overall complexity of $\mathcal{O}(N_{Cheb} N N_R)$. Once these moments are defined, since they do not depend on the energy, it is a straightforward set

of operations to determine the DoS for a grid of energies.

3.3. Inverse Participation Ratio (IPR)

A large part of this work deals with the localization properties of states, in particular what interests us is how these properties are affected by quasi-periodicity across topological phase transitions. The inverse participation ratio (IPR) is a quantity that helps us assess if a particular state is localized or extended.

We suppose we can write our state $|\phi_n\rangle$ in the local state basis $|\phi_n\rangle = \sum_i \phi_i^n \, |\vec{\mathbf{r}}_i\rangle$. The IPR is defined as follows

$$\mathrm{IPR}_n = \sum_i |\phi_i^n|^4 \,. \tag{3.39}$$

Since our wavefunctions are normalized to 1 when integrating over the volume (V) of our system we can intuitively understand that, if a state is delocalized, then $\phi_i^n \propto V^{-1/2}$, having equal contribution from every site. This mean that

$$\mathrm{IPR}_n \sim \sum_i V^{-2} \sim V^{-1}. \tag{3.40}$$

On the other hand, if the state is localized, it will only be confined to a small volume V_L and thus will scale to a constant value $\sim V_L^{-1}$ that is an estimate of the localization length. Therefore, through an analysis of the scaling of this quantity, the IPR, we are able to extract localization properties of our states.

We can construct a quantity that is precisely analogous to the IPR but now for the wavefunction written in the momentum basis. We denote this quantity IPR_k.

Another useful quantity we also analysed was the way the IPR and IPR_k decayed with increasing system size, obtaining the *fractal dimension*, γ (γ_k), defined as

$$\mathrm{IPR} \sim \frac{1}{N_{\mathrm{sites}}^{\gamma}} \quad \mathrm{IPR}_k \sim \frac{1}{N_{\mathrm{sites}}^{\gamma_k}}. \tag{3.41}$$

We know that for extended states the IPR will have a behaviour $\sim N_{\mathrm{sites}}^{-1}$, and so the fractal dimension is 1. As for localized states, IPR = const. and so $\gamma = 0$. For critical states, we know that the fractal dimension lies somewhere between 0 and 1. We see the usefulness of this quantity in determining the localization properties of states.

3.4. Level Spacing Statistics (LSS)

Random Matrix Theory (RMT) [27] is very useful when one wishes to study systems in the presence of disorder. One important quantity that stems from this area of mathematics is the

statistics of the separation between eigenvalues.

We can imagine that we have an Hamiltonian that may be represented by a matrix with entries H_{ij} in a certain basis. Naturally, it will have a set of eigenvalues $\{E_i\}$ which we will assume to be in ascending order, and call $\Delta E_i = E_{i+1} - E_i$ the spacing between levels. We can now look at the eigenstates that fall inside a given interval around an energy value ϵ $I \in]\epsilon - \delta\epsilon, \epsilon + \delta\epsilon[$ with $\delta\epsilon$ much smaller than the bandwidth of our system. If we now compute the spacing between levels inside this interval I we will have a probability distribution $p(\epsilon, s)$ for the spacing between levels at energy ϵ. If the eigenstates in I are entirely localized, then the eigenergies will be independent and the probability distribution for the spacing between levels wll be the Poisson distribution,

$$p(\epsilon, s) = e^{-s}. \tag{3.42}$$

If, on the other hand, the states are extended, there is correlation between eigenstates, and we expect level repulsion to occur, so $p(s)$ will no longer be a Poisson distribution and will depend upon the symmetries of the Hamiltonian. For the case where we have broken time-reversal symmetry, as is the case in the Haldane model, our Hamiltonian will belong to the Gaussian unitary ensemble (GUE) and will have a probability distribution for the spacing between levels that is very well approximated by:

$$p(\epsilon, s) = \frac{32}{\pi^2} s^2 e^{-\frac{4s^2}{\pi}}. \tag{3.43}$$

In practice, we will be interested in the variance of these distributions. For the distribution of level spacing of the GUE we have a variance $\sigma^2 / \langle s \rangle^2 \approx 0.178$. On the other hand, if our states are localized and the spacing between levels follows a Poisson distribution, its variance will be simply $\sigma^2 / \langle s \rangle^2 = 1$.

Another way of doing statistics on the spacing between levels is to study the ratio between consecutive levels, instead of their difference [7]. This alternative method was also implemented alongside the more common consecutive differences throughout this work. In the case where we study the ratios we do not look at the variance of our resulting probability distribution for the ratios $p(E, r)$, but instead at its mean. For this variant we take the reference analytical values $\langle r \rangle = 0.39$ for localized states (Poisson distribution) and $\langle r \rangle = 0.6$ for extended states, if the Hamiltonian belongs to the GUE.

Most often this method was used in conjunction with the Lanczos algorithm [38] to obtain the most useful eigenvalues and eigenvectors close to the Fermi level.

4. Results for the Haldane Model

In this section we look at the results obtained for the Haldane model subject to an incommensurate potential, modeled in the fashion described in the previous section.We alter the Hamiltonian by adding an on-site energy of $V_{\text{qp}}\left(\overrightarrow{\mathbf{r}}\right)$, our quasi-periodic potential defined in 2.2:

$$\left\langle \overrightarrow{\mathbf{R}}, \sigma \right| H \left| \overrightarrow{\mathbf{R}}, \sigma \right\rangle = \xi_\sigma m + V_{\text{qp}}\left(\overrightarrow{\mathbf{R}}\right), \tag{4.1}$$

where $\sigma = A, B$ indicates the sublattice and $\xi_A = -\xi_B = 1$.

We draw interesting conclusions related both to its topological and localization characteristics, as well as the interplay between both these properties. We make full use of the methods described in 3 in order to numerically compute these properties of interest. In order to obtain statistically significant results the majority of the results are obtained by making an average over different configurations of potential shift (2.3.1) and twisted boundary conditions.

Using the coupling matrix method 3.1 we obtain the Chern number for different parameters of the Haldane model shown in Figure 4.1.

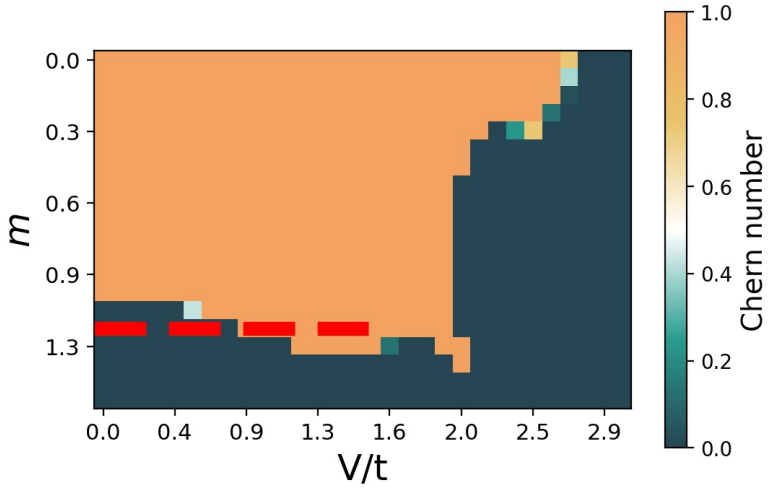

Figure 4.1.: Diagram of the topological phases for the Haldane model with $t_2 = 0.2$. These results were obtained for a system of size $N_{\text{sites}} = 34 \times 34$ with an average over 50 parameter configurations.

Naturally, for very high quasi-disorder values, the topology of the system is killed above a certain V_C that depends upon the staggered mass m. Also, if we are too deep in a topologically trivial phase (big staggered mass m) the incommensurate potential does not affect the topology of the system. Additionally, we see the emergence of a topological phase with $C = 1$ starting from a trivial phase for m close to $3\sqrt{3}t_2$ (shown by the dashed red line).

In the following sections, we will study two cases: the quasi-disorder-driven phase transition (i) from a topological to a trivial phase and (ii) from a trivial to a topological phase (TAI).

We are going to describe the phases of our system by taking into account three main characteristics: the spectral energy gap, the topological invariant, and the localization of states near the gap edge. The techniques used for this study are described in section 3, to wit, the KPM and Lanczos for the spectral gap, the coupling matrix method to compute the Chern number and the analysis of IPR and LSS for the localization of states. In the case of the IPR and the determination of the spectral gap using Lanczos, we also performed finite size scaling. We were able to obtain an estimate of the spectral gap in the thermodynamic limit, $N_{\text{sites}} \to \infty$, by making a linear regression of the value of the gap as a function of $1/N_{\text{sites}}$ and extracting the predicted gap size for $1/N_{\text{sites}} = 0$.

4.1. From topological to trivial

Fixing the value of $m = 0$ we obtain the following results for the topological phase as a function of incommensurate potential.

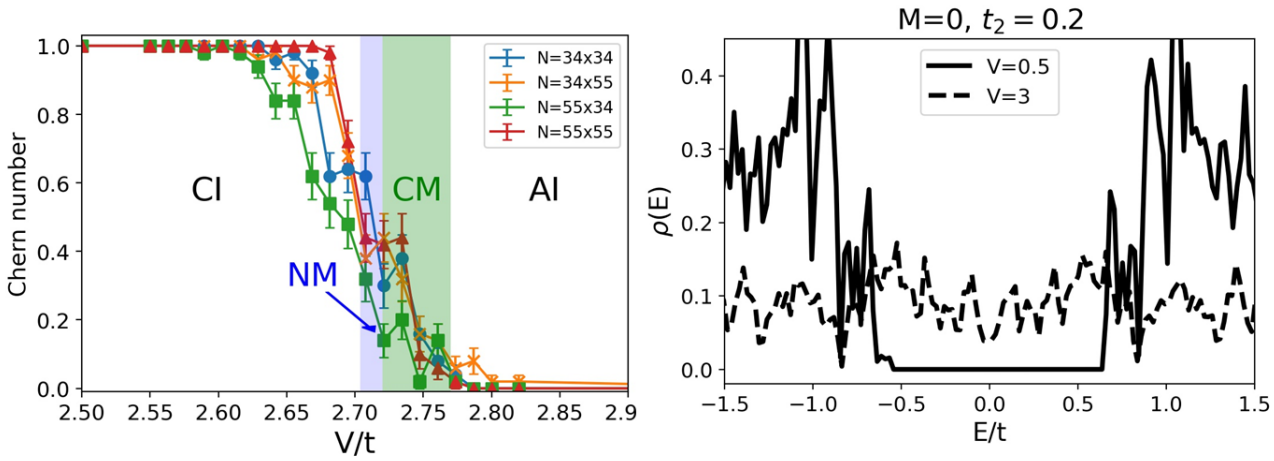

Figure 4.2.: (left) Chern number as a function of incommensurate potential strength V/t for various system sizes averaged over 50 configurations. (right) DoS of the Haldane model for $V = 0.5t$ (CI phase) and $V = 3t$ (AI phase).

We identify 3 distinct phases of our system regulated by the strength of the quasi-disorder imposed on our system, namely a Chern insulator phase with $C = 1$, a gapless phase with critical states at the Fermi level which we refer to as Critical Metal (CM), and an Anderson Insulator-like phase.

4.1.1. Chern Insulator (CI)

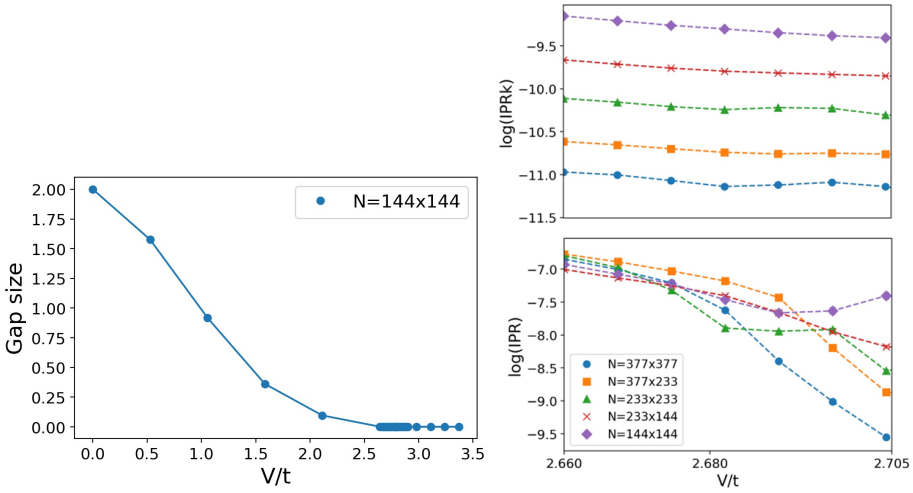

Figure 4.3.: (left) Evolution of the spectral gap for a system of size $N_{\text{sites}} = 144 \times 144$. The Lanczos method was used to select the closest energies to the Fermi level and then we calculated the difference between the largest negative and the smallest positive eigenvalues. We see that in the region where the system is a topological insulator with $C = 1$ the system has non-zero gap. (right) In the upper panel we show the $\log(\text{IPR}_k)$ as a function of quasi-disorder strength, and in the lower panel we represent the $\log(\text{IPR})$, also as a function of V/t for different system sizes. These results were obtained using the Lanczos algorithm, selecting the 20 most relevant states around zero energy.

The first phase is a Chern insulator with non-zero energy gap around the Fermi level and quantized, non-zero Chern number. We see that the results both from the KPM as well as the calculation of the spectral gap using the Lanczos algorithm show a finite gap in this region, as evidenced by the left panel in Figure 4.3. As for the topological invariant, it is apparent from figure 4.2 that the Chern number remains quantized and is robust to the presence of quasi-disorder until a critical value V_C which will be analysed in the following subsection. In the right panel of Figure 4.3 we show the evolution of IPR and IPRk with increasing V/t for different system sizes. In the upper panel we represent the $\log(\text{IPR}_k)$ and see an evident scaling of its value with increasing system size. The IPR (represented in the bottom panel),

on the other hand, starts off with little variation with size in the region which we identified as a CI. Eventually, this state of affairs changes as we get close to the transition which we will investigate in the next subsection.

4.1.2. Chern Insulator - Critical Metal

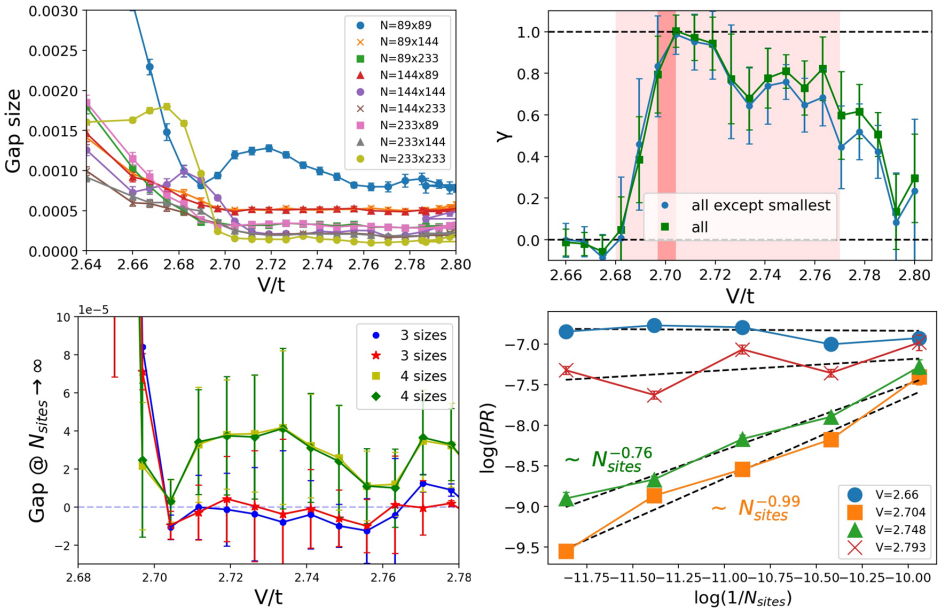

Figure 4.4.: (left) In the upper panel we represent the value of the spectral gap as a function of V/t for different system sizes averaged over 242 configurations. For V/t larger than ≈ 2.7 we have a very nice scaling of the gap size with increasing system size, leading us to perform a linear regression and obtain its value in the limit $N_{\text{sites}} \to \infty$. The results of this extrapolation are represented in the panel immediately below. The different lines represent different sets of sizes used to perform the linear fit. (right) In the upper panel we show the fractal dimension for two different regressions. The light red area represents the values of V/t where the Chern number is non-quantized for the biggest system considered in Figure 4.2, and the dark red shows the area where we see the gap closing for $N_{\text{sites}} \to \infty$. In the lower panel are represented a few select values of $\log(\text{IPR})$ *vs* $\log(N_{\text{sites}})$ for different values of V/t. We see the two values for which the states are localized exhibiting a nearly constant behaviour (blue and red), the critical state (green) which scales with $\sim N_{\text{sites}}^{-0.76}$ and the extended state (orange), which scales as expected with the inverse of system volume.

Inspecting Figure 4.4 we see the evident scaling of the gap size with increasing system size for $V \gtrapprox 2.7t$. This compels us to make a linear regression of these values and infer the value of the gap in the thermodynamic limit, $N_{\text{sites}} \to \infty$. This is precisely what we do and

represent in the panel immediately below. This finite size scaling analysis of the spectral gap yields a gap closing for $V = (2.7005 \pm 0.0037)\, t$ which remains closed thenceforth. The different lines represent different sets of points used to make the linear regession. Since we have data for uneven length systems in either direction with the same number of sites (for example $N_{\text{sites}} = 144 \times 89$ and $N_{\text{sites}} = 89 \times 144$) we performed two sets of linear regressions only changing which of these we chose. This gives us an idea of the error in our estimate of the gap. As we see, this doesn't cause much variation in the results, since both curves for 3 sizes (and 4 sizes) remain very close to each other. What truly impacts the results is how many sizes we use to make the linear regression. By using the values corresponding to the 3 largest sizes we obtain a very definite zero gap result that wasn't achieved with the 4 sizes.

Looking at Figure 4.2 we see that the region where the Chern number starts having a non-quantized value begins at a value of V/t increasingly higher with increasing system dimension. Even though the results for the largest system size we considered do not show a coincidence between the gap closing and the inception of the non-quantized Chern number region, we can attribute this to finite-size effects, and that in the thermodynamic limit these two events would coincide.

The panels on the right in Figure 4.4 show the results pertaining to the localization of states around zero energy. These evidence a transition from localized states, with fractal dimension very close to zero, to critical states in the region $V \in [2.726, 2.770]\, t$ which exhibit a scaling of the IPR as $\sim N_{\text{sites}}^{-0.7}$. Coinciding with the gap closing (dark red area), the states are ballistic with fractal dimension 1.We call this gapless phase with critical states, a critical metal (CM). In this critical metal region we naturally have non-quantized Chern number, since our system is gapless and the states around the gap edge are not localized. In the inferior panel we explicitly represent the scaling of the IPR with the number of sites in the system for four relevant values of V/t. Of interest to the CI-CM transition are the blue plot, showing a localized state (no scaling) before V_C, the orange plot, showing the extended state present for a value of quasi-periodic potential very close to V_C, showing exactly the expected scaling behaviour with $\sim N_{\text{sites}}^{-1}$, and, finally, the green plot shows the scaling of states in the critical region, which present a very precise scaling, like the extended states, albeit with a different power law $\sim N_{\text{sites}}^{-0.76}$.

4.1.3. Trivial Anderson Insulator

For $V \gtrapprox 2.78t$ we see in Figure 4.2 that the Chern number is once again quantized but this time with value 0, meaning we are in the presence of a phase analogous to the Anderson insulator, induced by quasi-disorder instead of uncorrelated disorder. Since for these values of potential strength the system is gapless, we expect the states around the gap to be localized in order to allow the Chern number to be defined. Indeed, we observe a gradual approximation of the fractal dimension to 0 as we increase V/t.

4.1.4. Level-spacing statistics

These results can be cross-checked with the results from the analysis of the level-spacing statistics described in 3.4.

We obtain these results by performing the algorithm defined previously for each set of eigenvalues obtained from distinct parameter values and then calculating the average of the ratios. The results are shown in Figure 2.2.

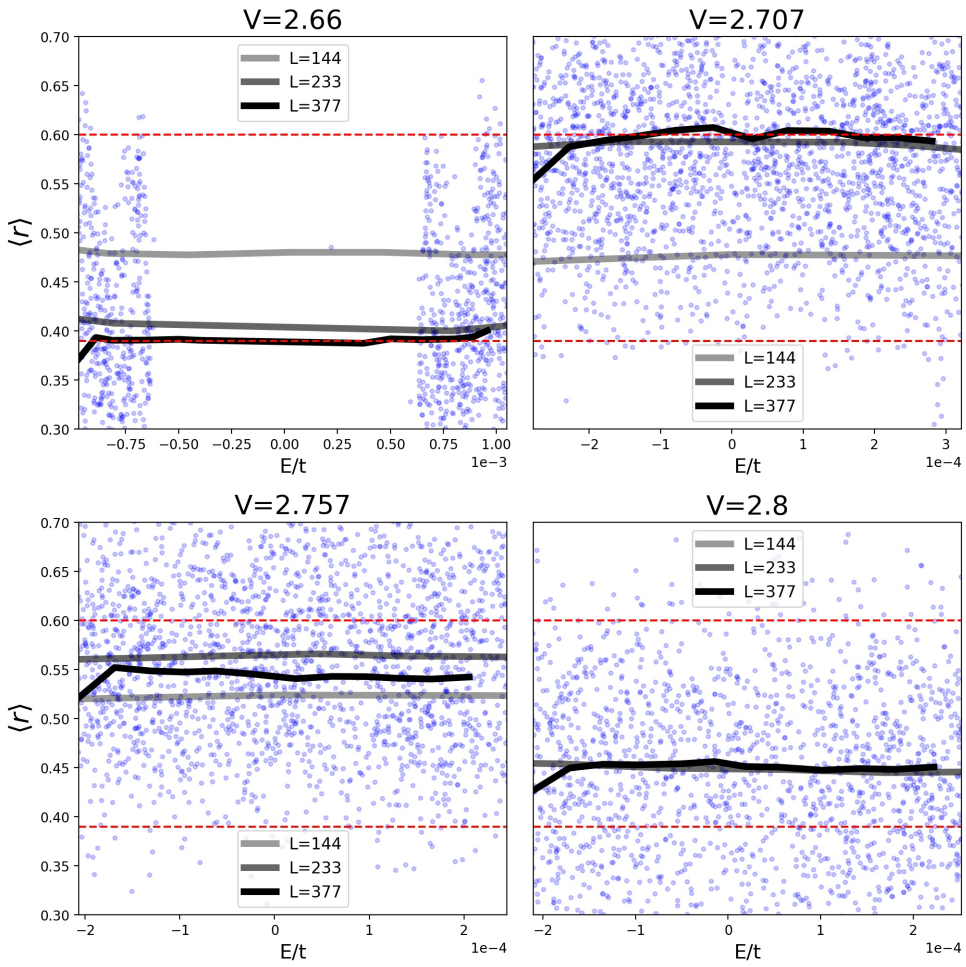

Figure 4.5.: LSS of the Haldane model with $m = 0$ for four different values of quasi-disorder in different areas of interest. The first ($V = 2.66t$) is in a region where our system is a CI. The IPR analysis and fractal dimension indicate that the states around the gap edge are localized. This analysis of the ratios between consecutive energy levels supports that claim, since $\langle r \rangle = 0.39$ is the expected value for states without level repulsion. The second ($V = 2.707t$) is right where the gap closes and the topological phase transition to a critical metal happens. In the second row, we represent the $\langle r \rangle$ for $V = 2.75t$ and $2.8t$.

Our earlier results are cemented by the convergence of the value of the ratios to 0.39 (the value corresponding to Poisson distribution, i.e. localized states) for $V = 2.66t$ in Figure 4.5. For a value that stands very close to $V = 2.7t$ (top right panel) we see a very clear convergence of our results, with increasing size of the system, to 0.6, meaning that there is level-repulsion and that our states are most likely extended. In the critical region (bottom left) the results are not very well defined and do not show any conclusive behaviour with increasing system size. It is, however, evident that $\langle r \rangle$ is closer to the GUE result, indicating level repulsion as expected for non-localized states. In the expected localized phase (bottom right) we do not see a clear convergence of $\langle r \rangle$ to 0.39 as would be expected, since in this regime the Chern number is quantized and the system is gapless, the eigenstates at the Fermi level should be localized. Therefore, we attribute this result to severe finite size effects.

4.2. From trivial to topological... to trivial

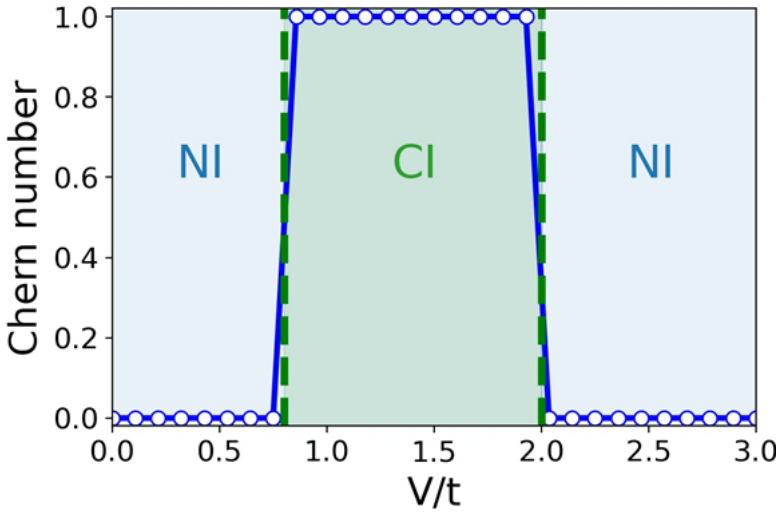

Figure 4.6.: (left) Chern results for the Haldane model with a staggered mass $m = 1.2$. We identify three distinct phases of our system controlled by the amplitude of the quasi-periodic potential: a normal insulator phase, a Chern insulator phase, and, finally, an Anderson insulator-like phase. These results were obtained for a system with dimensions 34×34 averaged over 30 configurations.

This case is represented in Figure 4.1 by the dashed red line.

In this situtation, we start in a topologically trivial phase. With increasing quasi-disorder a topological phase is induced. This situation is analogous to the TAI we saw in subsection 1.8.2. Increasing even further the quasi-disorder strength induces again an insulating phase with Chern number 0. However, contrary to the situation analysed in the previous section,

this trivial phase due to the presence of very high quasi-disorder is not gapless and instead has a finite spectral gap. This means that it is not an AI but a NI. Looking at Figure 4.7, we see that the results from Lanczos and finite size scaling show very distinctly that we only have spectral closing of the energy gap at the Fermi level whenever a topological phase transition occurs.

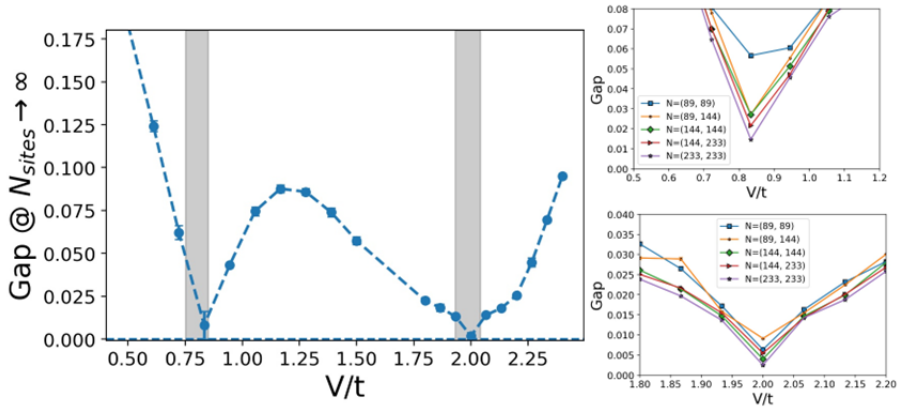

Figure 4.7.: (top) Gap size in the limit $N_{sites} \to \infty$ obtained through linear regression. The shaded grey areas represent the regions where we expect to find the topological phase transitions (left) Zoom around the first gap closing with different system sizes represented. (right) Zoom around the second gap closing with different system sizes represented.

Indeed, we already see a qualitative difference between the transition at $m = 0$ and these transitions we have just now seen, since, albeit being also accompanied by a gap closing, the previous topological phase transition had no reopening.

We again studied the localization of states around the gap edge for this case. We see the results in Figure 4.8

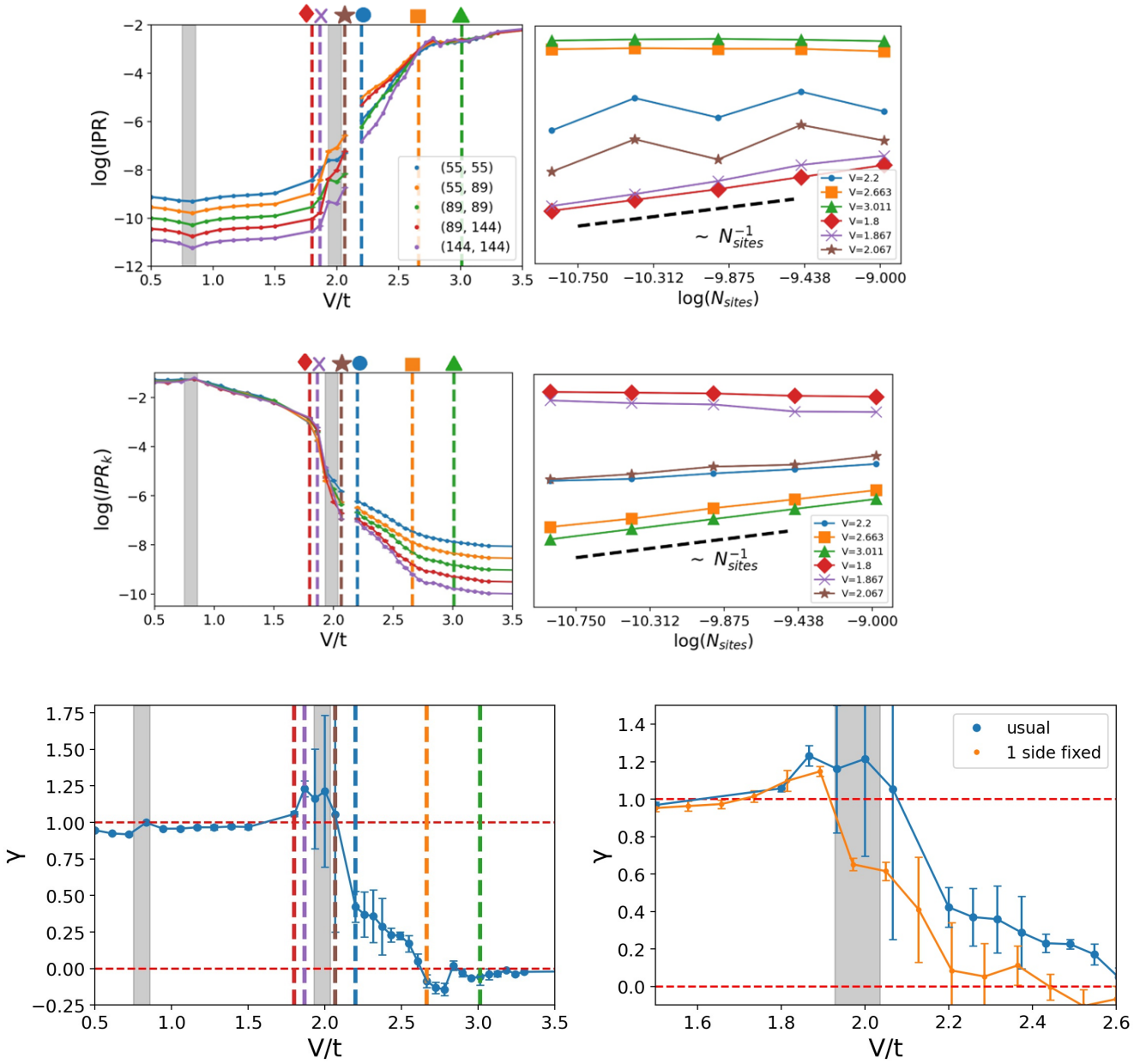

Figure 4.8.: (top) On the left side we represent the value of log (IPR) as a function of quasi-periodic strength V/t for different system sizes. The shaded regions indicate where we saw the topological phase transitions in Figure 4.6. On the right we represent the values of log (IPR) $vs 1/N_{\text{sites}}$ for a few values of potential. (middle) These figures show the same as the figures on top but for the values of the IPR_k. (bottom) Fractal dimension as a function of V/t. On the left panel we see the values obtained the using the usual method and on the right panel we see a comparison between these results and the ones obtained from the data extracted from systems of increasing size maintaining one of them fixed (in this case, we fixed one of the sides of the system to $L = 89$)

4.2.1. Normal Insulator - Chern Insulator

As stated previously, the first transition is from a NI to a CI with $C = 1$. This means that before the transition we have a finite spectral gap, which is verified with finite size scaling analysis, presented in Figure 4.7. Looking at the IPR results in Figure 4.8 around the first transition we see they are not affected. On both sides we have a very good scaling of the IPR with $1/N_{\text{sites}}$. On the other hand, the IPR_k shows a localized wavefunction in momentum-space, evidencing the presence of ballistic states, this is shown in the middle panel of Figure 4.8. Thus, the mechanism inducing this phase transition is simply the closing and reopening of the gap with ballistic states on both sides, just as we have seen happens in the clean, translation-invariant case.

4.2.2. Chern Insulator - Normal Insulator

For the second transition, from a CI to a NI, around the region of the phase transition $V = (2.00 \pm 0.07)\, t$ our results for the fractal dimension (shown in the last row of Figure 4.8) present very big error bars, inciting us to look at the values of IPR themselves in order to assess the validity of this linear fit.

It is obvious that, starting around $V \approx 1.9$ the values of IPR corresponding to the systems with different lengths in each direction (curves with orange and red points in the right top panel of Figure 4.8) start to deviate from a linear relation with the other systems with equal lengths in both directions, as evidenced by the blue and brown plots in the top panels of Figure 4.8. This peculiar behaviour is due to the fact that, if the states are localized and have a very big localization length, the way with which the IPR scales might be different depending on the direction we are varying[1]. By making a linear regression of $\log(\text{IPR})$ vs$1/N_{\text{sites}}$ we are assuming that the scaling is the same for each direction. If the eigenstates were truly extended, this assumption would be justified. The derivations from the linear regression when the sizes chosen along x and y are different is, therefore, a hint that the eigenstates are not truly extended.

To indeed verify this we once again calculated the fractal dimension for different system sizes but fixing the length of one of the sides for all systems (in our case $L = 89$). This way, we are only truly evaluating the scaling in one direction. We see in the last row of panels of Figure 4.8 that this yielded results that decayed to $\gamma = 0$ after the topological phase transition much faster than the results shown previously, thus confirming our suspicions both with respect to the behaviour of the cross-size systems and the localized nature of the states after the

[1] This is why in the region $V \in [0.5, 1.5]\, t$ we see an accurate linear relation between the IPR and $1/N_{\text{sites}}$,since the states surrounding the gap edge are delocalized in this case, the direction we alter should have no effect.

topological transition. Therefore we are able to conclude that the topological transition is in this case accompanied by ballistic states before $V < V_C$ and localized states after $V > V_C$.

5. Results for the Square Lattice Model

For the square lattice we implemented the incommensurate potential in a different way to the Haldane model. Instead of adding an on-site energy that is equal in both sublattices, we added an on-site energy with symmetric value in each sublattice of the same unit cell. This means that

$$\left\langle \vec{\mathbf{R}}, \sigma \right| H \left| \vec{\mathbf{R}}, \sigma \right\rangle = \xi_\sigma \left(m + V_{\text{qp}} \left(\vec{\mathbf{R}} \right) \right). \tag{5.1}$$

This model differs from the one studied by Fu, et al. [15] precisely in the fact that they do not change the sign of the incommensurate potential according to the sub-lattice.

The phase diagram for the model on the square lattice in the presence of a quasi-periodic potential is more diverse than the one for the Haldane model, as can be seen in Figure 5.1. We have 3 distinct phases for $m > 0$, with Chern number -1, 1, and 0. The diagram for $m < 0$ we have the same phases with symmetric topological invariant. Some features are common to the Haldane model, such as the reentrant behaviour for $m \in [2.0, 3.5]$.

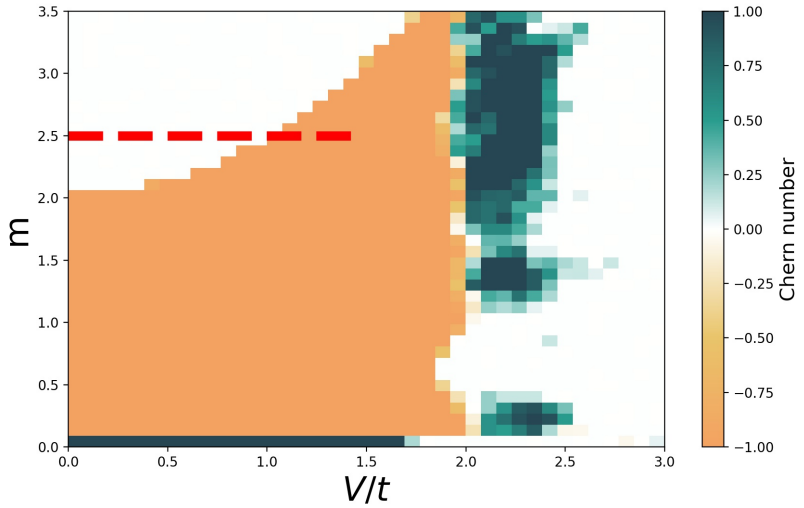

Figure 5.1.: Phase diagram for the Square lattice model obtained for a system with dimensions 21×21 averaged over 100 configurations

We will now focus on a value of m for which we see three topological transitions happen,

e.g. $m = 2.5$, marked as an horizontal dashed line in Figure 5.1, and describe them with the same methods we used for the Haldane model in 4.

5.1. From normal, to Chern, to Anderson

For this case we see the results shown in Figure 5.2 top for the Chern number as a function of quasi-disorder strength. We identify four distinct phases. Three are already familiar to us: NI, TI, and AI, and the other, CCI, stands for critical Chern insulator and will be described below.

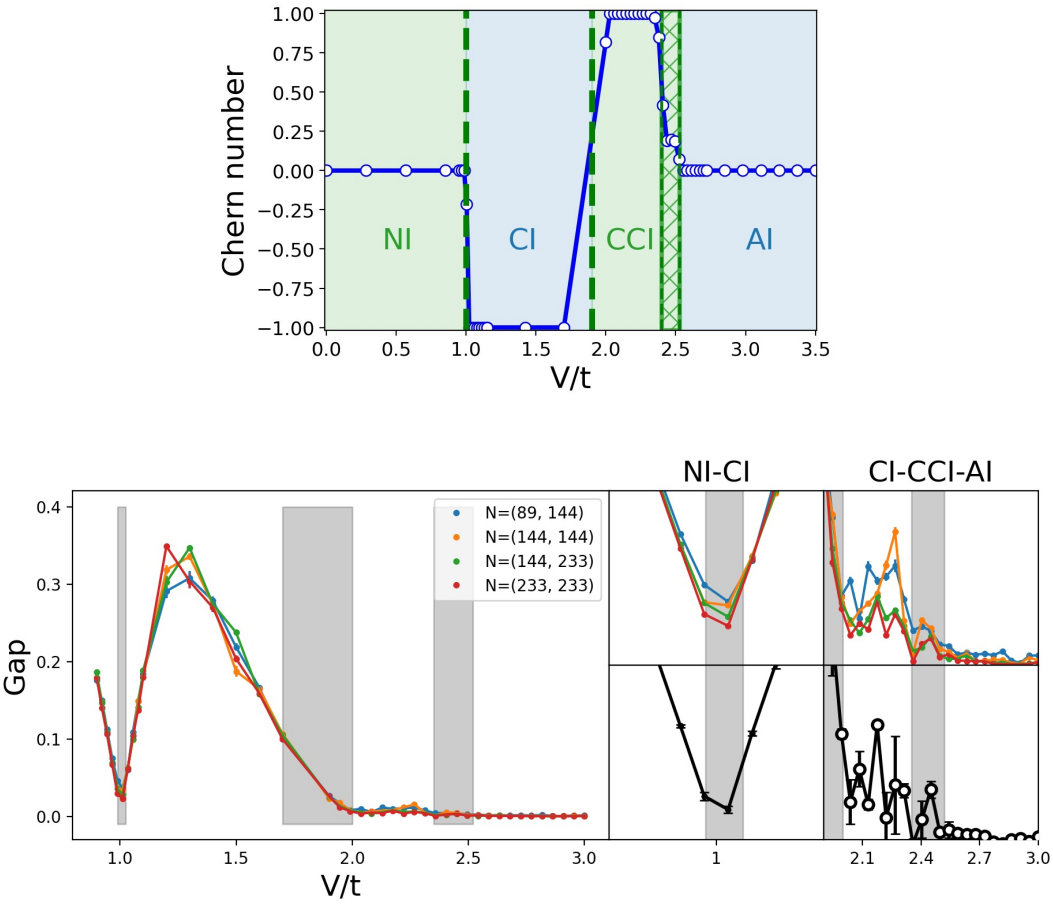

Figure 5.2.: (top) Topological invariant as a function of quasi-periodic potential strength. We observe three topological transitions at $V = (1.007 \pm 0.017)\, t$,$V = (1.95 \pm 0.15)\, t$, and $V = (2.435 \pm 0.170)\, t$. The criss-crossed green region denotes a range of value of V/t where our results are not yet conclusive, and is discussed in more detail in the body of the text. These results are obtained for a system with size $N_{\text{sites}} = 34 \times 34$ averaged over 200 configurations. (bottom) In the top right panels we see the values of the gap for different system sizes and on the bottom panels we represent the gap extrapolated at the thermodynamic limit by linear regression as a function of V/t. The three topological transitions are indicated by the grey areas, drawn according to the estimated error bars for the different critical points.

5.1.1. Normal Insulator - Chern Insulator

We see that the first transition, from a topologically trivial gapped state to a Chern insulator, is very sharp, and happens for a value of $V = (1.007 \pm 0.017)\, t$. It is also accompanied by a just as sharp closing and subsequent reopening of the spectral gap, as seen in Figure 5.2.

Again, we studied the IPR of the states around the gap edge for this system.

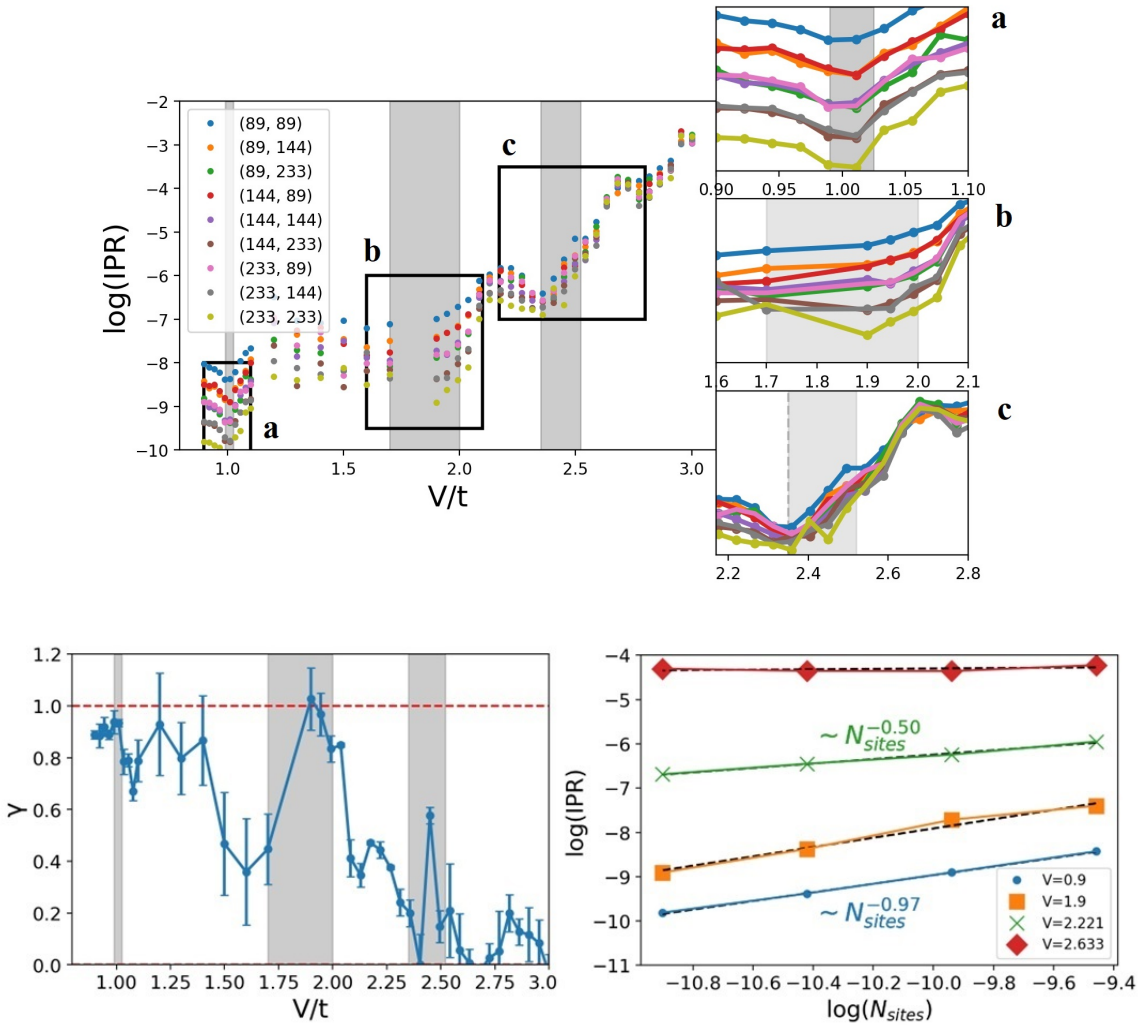

Figure 5.3.: (top) log(IPR) as a function of quasi-disorder strength for different system sizes. In the inset axes are magnified areas of interest to our study of the localization properties close to the topological phase transitions (represented by the shaded regions). (bottom) On the left is represented the fractal dimension (γ) as a function of V/t. On the right we show the scaling of the IPR for a few selected values of quasi-disorder.

In the vicinity of this transition, we see in Figure 5.3 that the scaling of the IPR with system size is not much affected by the presence of the topological transition, evidencing on both sides ballistic states, since they are also localized in momentum-space as shown in Figure 5.4. Looking at the bottom right panel of Figure 5.3 we can see that the scaling of the states

before this transition (blue plot) is very precise, with a power law $\sim N_{\text{sites}}^{-0.97}$, signaling the presence of extended states.

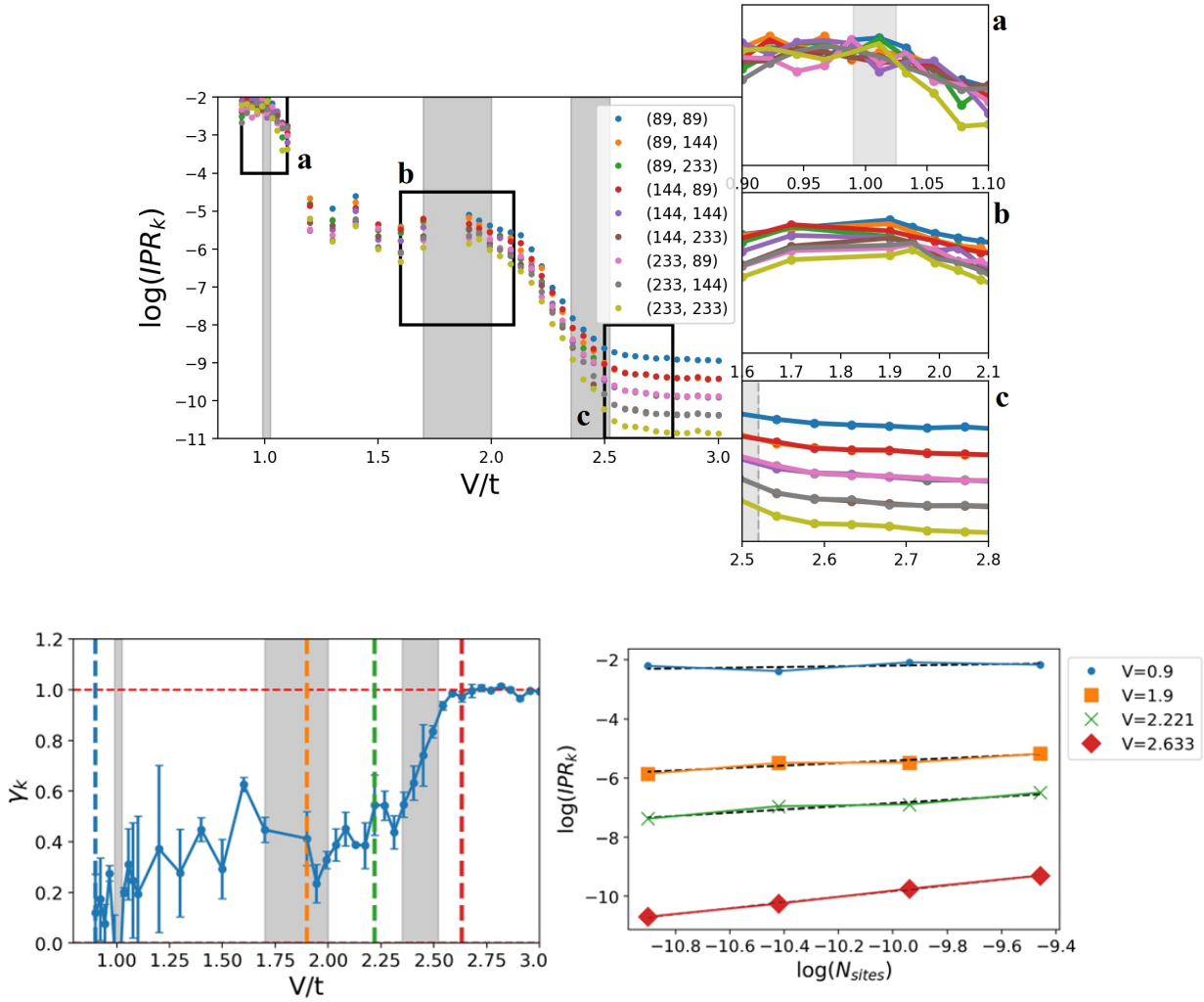

Figure 5.4.: (top) $\log(\text{IPR}_k)$ as a function of quasi-disorder strength. In the inset axes are magnified regions of interest in our analysis of the localization properties of states around the gap edge and how they are altered in the topological transitions. (bottom) On the left is represented the fractal dimension in reciprocal space (γ_k) as a function of V/t. On the right we show the scaling of IPR_k for a few selected values of quasi-disorder.

5.1.2. Chern Insulator - Critical Chern Insulator

The second transition is from a Chern insulator to a Chern insulator with different topological invariant which exhibits critical states around the gap edge, which we call critical Chern

insulator. We can look at Figure 5.2 to conclude that there is no conclusive gap closing in this phase, however we can infer that it must be the case since we have change in the topological invariant and that necessarily entails, in this case, a closing of the spectral gap at some point. The critical nature of the states is shown in the bottom left panel of Figure 5.3 where we see a very robust fractal dimension $\gamma \approx 0.4$ for values of $V \in [2.0, 2.3]\, t$. Verifying the values in the bottom right panel of Figure 5.3 for this region (green plot) we ascertain that the linear regression is extremely precise, hence the small error bars in the fractal dimension, and so our assessment that this is a robust region of critical states near the gap edge is trustworthy.

We distinguish this critical phase from the one seen in subsection 4.1.2 for the Haldane model with $m = 0$, since in that case we were in the presence of a gapless system, a so-called critical metal, and the Chern number was non-quantized.

5.1.3. Critical Chern Insulator - Anderson Insulator

Increasing the incommensurate potential even further has evident effects both in the spectral gap and in the localization of states. We can see in Figure 5.2 that the data for the spectral gap is very noisy presenting big fluctuations for all sizes, which manifests itself in the big error bars in the values obtained through linear regression for the value of the gap in the thermodynamic limit. Nevertheless, we are fairly certain that before the last topological phase transition we have a, albeit very small, non-vanishing spectral gap. The reason being that, since in that region we have, undoubtedly, quantized Chern number, and the localization data in Figure 5.3 leads us to believe that the states are critical around the gap edge, the only way to conciliate these two facts is to have finite spectral gap.

In the region where we see the topological phase transition, that is, the last shaded area in both figures, things start to become less clear. Right at the onset of this region, we see that there is a very plausible closing of the spectral gap that then seems to reopen, assuming approximately the same value observed before this closing. At the end of the region, we once again see the gap closing and remain closed thenceforth. As for the fractal dimension, we see a gradual reduction of γ from the critical value to 0, signaling the localization of the states around the gap edge. After this, we have a single point that stands out from the rest by having $\gamma \approx 0.6$, and then the data evidences, again, a localization of states after the topological phase transition.

The nature of this transition is, therefore, very confusing, since many events occur in a short range of incommensurate potential strength and the data is, for now, quite uncertain in some regions. If the small gapped region lying within the area where we see the topological transition happening did not exist, we could conceivably explain the mechanism governing this transition using the concept of levitation and annihilation of states 1.8.1, where we would have a closing of the gap with localized states at the Fermi level. Subsequently, levitation of the extended/critical states would occur for increasing quasi-disorder, eventually merging and

annihilating, causing the topological change and the localization of all states, at least around the Fermi level.

Unfortunately, this may not be the case, since at least one of the values of the gap in this region seems to be quite robust, presenting a small error bar and a value comparable to the ones seen immediately prior to the gap closing.

6. Conclusion

Throughout this work we took a detailed look at the interplay between quasi-periodicity, topology and localization in models of Chern insulators which have broken time-reversal symmetry.

Contrary to the case where we have uncorrelated disorder, where we only have gapless transitions from localized to localized states 1.8.1, we have found a myriad of transitions, exhibiting nearly every combination of localization and topological properties. These findings are summarized in the tables below:

Haldane model		
M=0	M=1.2	
$1 \to CM \to 0$	$0 \to 1$	$1 \to 0$
closing and no reopening	gap closing and reopening	gap closing and reopening
localized to critical region and back to localized after transition	ballistic to ballistic	ballistic to localized

Square model		
M=2.5		
$0 \to -1$	$-1 \to 1$	$1 \to 0$
closing and opening	gap closing and reopening	closing and no reopening
ballistic to ballistic	critical to critical	critical to localized

The physics presented throughout this paper goes beyond the models explored here and can be emulated by cold atom and metamaterial labs [28, 44, 64].

Bibliography

[1] E. Abrahams, P. W. Anderson, D. C. Licciardello, and T. V. Ramakrishnan. Scaling theory of localization: Absence of quantum diffusion in two dimensions. *Phys. Rev. Lett.*, 42:673–676, Mar 1979.

[2] Y. Aharonov and D. Bohm. Significance of electromagnetic potentials in the quantum theory. *Phys. Rev.*, 115:485–491, Aug 1959.

[3] P. W. Anderson. Absence of diffusion in certain random lattices. *Phys. Rev.*, 109:1492–1505, Mar 1958.

[4] T. Ando. Numerical study of symmetry effects on localization in two dimensions. *Phys. Rev. B*, 40:5325–5339, Sep 1989.

[5] Miguel A.N. Araújo and Pedro D. Sacramento. *Topologia em Matéria Condensada - uma Introdução*. IST Press, 2020.

[6] LMC Armas. Revisiting the quantum hall effect inthe haldane model, msc thesis. 2017.

[7] Y. Y. Atas, E. Bogomolny, O. Giraud, and G. Roux. Distribution of the ratio of consecutive level spacings in random matrix ensembles. *Phys. Rev. Lett.*, 110:084101, Feb 2013.

[8] S. Aubry and G. André. Analyticity breaking and anderson localization in incommensurate lattices. *Ann. Israel Phys. Soc*, 1980.

[9] B. Andrei Bernevig, Taylor L. Hughes, and Shou-Cheng Zhang. Quantum spin hall effect and topological phase transition in hgte quantum wells. *Science*, 314(5806):1757–1761, 2006.

[10] H. Bethe. Theorie der beugung von elektronen an kristallen. *Annalen der Physik, Volume392, Issue17*, 1928.

[11] Rafi Bistritzer and Allan H. MacDonald. Moiré bands in twisted double-layer graphene. *Proceedings of the National Academy of Sciences*, 108(30):12233–12237, 2011.

[12] Felix Bloch. Über die quantenmechanik der elektronen in kristallgittern. *Zeitschrift Für Physik 52, no. 7*, July 1, 1929.

[13] Leonhard Euler. Solutio problematis ad geometriam situs pertinentis. *textsCommentarii Academiae scientiarum imperialis Petropolitanae*, 1726.

[14] Yixing Fu, Elio J. König, Justin H. Wilson, Yang-Zhi Chou, and Jedediah H. Pixley. Magic-angle semimetals. *npj Quantum Materials*, 5(1):71, 2020.

[15] Yixing Fu, Justin H. Wilson, and J. H. Pixley. Flat topological bands and eigenstate criticality in a quasiperiodic insulator. *Physical Review B*, 104(4), jul 2021.

[16] Miguel Gonç alves, Hadi Z Olyaei, Bruno Amorim, Rubem Mondaini, Pedro Ribeiro, and Eduardo V Castro. Incommensurability-induced sub-ballistic narrow-band-states in twisted bilayer graphene. *2D Materials*, 9(1):011001, nov 2021.

[17] Miguel Gonçalves, Bruno Amorim, Eduardo V. Castro, and Pedro Ribeiro. Renormalization-group theory of 1d quasiperiodic lattice models with commensurate approximants, 2022.

[18] Miguel Gonçalves, Pedro Ribeiro, and Eduardo V. Castro. The haldane model under quenched disorder, 2018.

[19] C. W. Groth, M. Wimmer, A. R. Akhmerov, J. Tworzydło, and C. W. J. Beenakker. Theory of the topological anderson insulator. *Phys. Rev. Lett.*, 103:196805, Nov 2009.

[20] F. D. M. Haldane. Model for a quantum hall effect without landau levels: Condensed-matter realization of the "parity anomaly". *Phys. Rev. Lett.*, 61:2015–2018, Oct 1988.

[21] E. H. Hall. On a new action of the magnet on electric currents. *American Journal of Mathematics*, 2(3):287–292, 1879.

[22] M. Z. Hasan and C. L. Kane. Colloquium: Topological insulators. *Rev. Mod. Phys.*, 82:3045–3067, Nov 2010.

[23] Shinobu Hikami. Spin-orbit interaction and magnetoresistance in the two dimensional random system. *Progress of Theoretical Physics*, 63, 1980-02.

[24] Topological Insulators and Topological Superconductors. *B. Andrei Bernevig.* Princeton University Press, 2013.

[25] S M João, Mia Anđelković, Lucian Covaci, Tatiana G. Rappoport, J. M. Viana Parente Lopes, and Aires Ferreira. Kite: high-performance accurate modelling of electronic structure and response functions of large molecules, disordered crystals and heterostructures. *Royal Society Open Science*, 7, 2020.

[26] C. L. Kane and E. J. Mele. Quantum spin hall effect in graphene. *Phys. Rev. Lett.*, 95:226801, Nov 2005.

[27] Michael Schreiber Karl Heinz Hoffmann. *Computational Statistical Physics*. Springer Berlin, Heidelberg.

[28] Colin J. Kennedy, Georgios A. Siviloglou, Hirokazu Miyake, William Cody Burton, and Wolfgang Ketterle. Spin-orbit coupling and quantum spin hall effect for neutral atoms without spin flips. *Phys. Rev. Lett.*, 111:225301, Nov 2013.

[29] K. v. Klitzing, G. Dorda, and M. Pepper. New method for high-accuracy determination of the fine-structure constant based on quantized hall resistance. *Phys. Rev. Lett.*, 45:494–497, Aug 1980.

[30] Mahito Kohmoto. Topological invariant and the quantization of the hall conductance. *Annals of Physics*, 160(2):343–354, 1985.

[31] Markus König, Hartmut Buhmann, Laurens W. Molenkamp, Taylor Hughes, Chao-Xing Liu, Xiao-Liang Qi, and Shou-Cheng Zhang. The quantum spin hall effect: Theory and experiment. *Journal of the Physical Society of Japan*, 77(3):031007, 2008.

[32] J. Kosterlitz and D. Thouless. Ordering, metastability and phase transitions in two-dimensional systems. *J. Phys. C: Solid State Phys.*, 6:1181, 04 1973.

[33] B Kramer and A MacKinnon. Localization: theory and experiment. *Reports on Progress in Physics*, 56(12):1469–1564, dec 1993.

[34] Yaacov E. Kraus, Yoav Lahini, Zohar Ringel, Mor Verbin, and Oded Zilberberg. Topological states and adiabatic pumping in quasicrystals. *Physical Review Letters*, 109(10), sep 2012.

[35] Yaacov E. Kraus and Oded Zilberberg. Topological equivalence between the fibonacci quasicrystal and the harper model. *Phys. Rev. Lett.*, 109:116404, Sep 2012.

[36] S. V. Kravchenko, G. V. Kravchenko, J. E. Furneaux, V. M. Pudalov, and M. D'Iorio. Possible metal-insulator transition at b=0 in two dimensions. *Phys. Rev. B*, 50:8039–8042, Sep 1994.

[37] Markus König, Steffen Wiedmann, Christoph Brüne, Andreas Roth, Hartmut Buhmann, Laurens W. Molenkamp, Xiao-Liang Qi, and Shou-Cheng Zhang. Quantum spin hall insulator state in hgte quantum wells. *Science (New York, N.Y.)*, 318:766–70, Nov 2007.

[38] Cornelius Lanczos. An iteration method for the solution of the eigenvalue problem of the linear differential and integral operators. *Journal of Research of the National Bureau of Standards*, 1950.

[39] L. Landau. Diamagnetismus der metalle. *Zeitschrift für Physik*, 64(9):629–637, 1930.

[40] R. B. Laughlin. Levitation of extended-state bands in a strong magnetic field. *Phys. Rev. Lett.*, 52:2304–2304, Jun 1984.

[41] Jian Li, Rui-Lin Chu, J. K. Jain, and Shun-Qing Shen. Topological anderson insulator. *Phys. Rev. Lett.*, 102:136806, Apr 2009.

[42] J. M. B. Lopes dos Santos, N. M. R. Peres, and A. H. Castro Neto. Graphene bilayer with a twist: Electronic structure. *Phys. Rev. Lett.*, 99:256802, Dec 2007.

[43] J. M. B. Lopes dos Santos, N. M. R. Peres, and A. H. Castro Neto. Continuum model of the twisted graphene bilayer. *Phys. Rev. B*, 86:155449, Oct 2012.

[44] Eran Lustig, Steffen Weimann, Yonatan Plotnik, Yaakov Lumer, Miguel A. Bandres, Alexander Szameit, and Mordechai Segev. Photonic topological insulator in synthetic dimensions. *Nature*, 567:356–360, Mar 2019.

[45] Moon Jip Park, Hee Seung Kim, and SungBin Lee. Emergent localization in dodecagonal bilayer quasicrystals. *Phys. Rev. B*, 99:245401, Jun 2019.

[46] Xiao-Liang Qi and Shou-Cheng Zhang. Topological insulators and superconductors. *Rev. Mod. Phys.*, 83:1057–1110, Oct 2011.

[47] Zhenhua Qiao, Yulei Han, Lei Zhang, Ke Wang, Xinzhou Deng, Hua Jiang, Shengyuan A. Yang, Jian Wang, and Qian Niu. Anderson localization from the berry-curvature interchange in quantum anomalous hall systems. *Physical Review Letters*, 117(5), jul 2016.

[48] S. Raghu, Xiao-Liang Qi, C. Honerkamp, and Shou-Cheng Zhang. Topological mott insulators. *Phys. Rev. Lett.*, 100:156401, Apr 2008.

[49] Linda E. Reichl. *A modern course in statistical physics.* Wiley-Vch, 2016.

[50] S. Shallcross, S. Sharma, E. Kandelaki, and O. A. Pankratov. Electronic structure of turbostratic graphene. *Phys. Rev. B*, 81:165105, Apr 2010.

[51] Steven H. Simon. *The Oxford Solid State Basics / Steven H. Simon.* Oxford University Press, Oxford, first edition. edition, 2013.

[52] J. E. Socolar, T. C. Lubensky, and P. J. Steinhardt. Phonons, phasons, and dislocations in quasicrystals. *Physical review. B, Condensed matter*, 34:3345–3360, Sep 1986.

[53] Walter Steurer. Quasicrystals. a primer by c. janot. *Acta Crystallographica Section A*, 53, 07 1997.

[54] Horst L. Stormer, Daniel C. Tsui, and Arthur C. Gossard. The fractional quantum hall effect. *Rev. Mod. Phys.*, 71:S298–S305, Mar 1999.

[55] Antonio Š trkalj, Elmer V. H. Doggen, Igor V. Gornyi, and Oded Zilberberg. Many-body localization in the interpolating aubry-andré-fibonacci model. *Physical Review Research*, 3(3), sep 2021.

[56] E. Suárez Morell, J. D. Correa, P. Vargas, M. Pacheco, and Z. Barticevic. Flat bands in slightly twisted bilayer graphene: Tight-binding calculations. *Phys. Rev. B*, 82:121407, Sep 2010.

[57] D J Thouless. A relation between the density of states and range of localization for one dimensional random systems. *Journal of Physics C: Solid State Physics*, 5(1):77–81, jan 1972.

[58] G. Trambly de Laissardière, D. Mayou, and L. Magaud. Localization of dirac electrons in rotated graphene bilayers. *Nano Lett.*, 10(3):804–808, March 2010.

[59] Mor Verbin, Oded Zilberberg, Yaacov E. Kraus, Yoav Lahini, and Yaron Silberberg. Observation of topological phase transitions in photonic quasicrystals. *Phys. Rev. Lett.*, 110:076403, Feb 2013.

[60] Berry Michael Victor. Quantal phase factors accompanying adiabatic changes. *Proc. R. Soc. Lond. A*, 1984.

[61] Alexander Weiße, Gerhard Wellein, Andreas Alvermann, and Holger Fehske. The kernel polynomial method. *Rev. Mod. Phys.*, 78:275–306, Mar 2006.

[62] Wei Yao, Eryin Wang, Changhua Bao, Yiou Zhang, Kenan Zhang, Kejie Bao, Chun Kai Chan, Chaoyu Chen, Jose Avila, Maria C. Asensio, Junyi Zhu, and Shuyun Zhou. Quasicrystalline 30° twisted bilayer graphene as an incommensurate superlattice with strong interlayer coupling. *Proceedings of the National Academy of Sciences*, 115(27):6928–6933, 2018.

[63] Yi-Fu Zhang, Yun-You Yang, Yan Ju, Li Sheng, Rui Shen, Dong-Ning Sheng, and Ding-Yu Xing. Coupling-matrix approach to the chern number calculation in disordered systems. *Chinese Physics B*, 22(11):117312, nov 2013.

[64] Erhai Zhao. Topological circuits of inductors and capacitors, 10 2018.

[65] Y-X Zhu, J He, C-L Zang, Y Liang, and S-P Kou. Magnetic topological insulators at finite temperature. *Journal of Physics: Condensed Matter*, 26(17):175601, apr 2014.

A. Berry phase

We consider a basis of states that obeys

$$H\left|n\left(\overrightarrow{\mathbf{R}}\right)\right\rangle = E_n\left|n\left(\overrightarrow{\mathbf{R}}\left(0\right)\right)\right\rangle. \tag{A.1}$$

After a time t, under the adiabatic approximaton, a state that started as $\left|n\left(\overrightarrow{\mathbf{R}}\left(0\right)\right)\right\rangle$ will be in a state $\left|n\left(\overrightarrow{\mathbf{R}}\left(t\right)\right)\right\rangle$. During this time it may acquire a phase $\theta\left(t\right)$, therefore we write

$$\left|\psi\left(t\right)\right\rangle = e^{-i\theta(t)}\left|n\left(\overrightarrow{\mathbf{R}}\left(t\right)\right)\right\rangle. \tag{A.2}$$

This state must obey Schrödinger's equation

$$\begin{aligned}
\hat{H}\left|\psi\left(t\right)\right\rangle &= i\hbar\frac{d}{dt}\left|\psi\left(t\right)\right\rangle \\
E_n\left(\overrightarrow{\mathbf{R}}\left(t\right)\right)e^{-i\theta(t)}\left|n\left(\overrightarrow{\mathbf{R}}\left(t\right)\right)\right\rangle &= i\hbar\frac{d}{dt}\left[e^{-i\theta(t)}\left|n\left(\overrightarrow{\mathbf{R}}\left(t\right)\right)\right\rangle\right] \\
\frac{-i}{\hbar}E_n\left(\overrightarrow{\mathbf{R}}\left(t\right)\right)e^{-i\theta(t)}\left|n\left(\overrightarrow{\mathbf{R}}\left(t\right)\right)\right\rangle &= i\frac{d\theta}{dt}e^{-i\theta(t)}\left|n\left(\overrightarrow{\mathbf{R}}\left(t\right)\right)\right\rangle + e^{-i\theta(t)}\frac{d}{dt}\left|n\left(\overrightarrow{\mathbf{R}}\left(t\right)\right)\right\rangle \\
\frac{-i}{\hbar}E_n\left(\overrightarrow{\mathbf{R}}\left(t\right)\right)\left|n\left(\overrightarrow{\mathbf{R}}\left(t\right)\right)\right\rangle &= -i\frac{d\theta}{dt}\left|n\left(\overrightarrow{\mathbf{R}}\left(t\right)\right)\right\rangle + \frac{d}{dt}\left|n\left(\overrightarrow{\mathbf{R}}\left(t\right)\right)\right\rangle
\end{aligned}. \tag{A.3}$$

Now applying $\left\langle n\left(\overrightarrow{\mathbf{R}}\left(t\right)\right)\right|$

$$\begin{aligned}
\frac{-i}{\hbar}E_n\left(\overrightarrow{\mathbf{R}}\left(t\right)\right) &= -i\frac{d\theta}{dt} + \left\langle n\left(\overrightarrow{\mathbf{R}}\left(t\right)\right)\right|\frac{d}{dt}\left|n\left(\overrightarrow{\mathbf{R}}\left(t\right)\right)\right\rangle \\
\hbar\frac{d\theta}{dt} &= E_n\left(\overrightarrow{\mathbf{R}}\left(t\right)\right) - i\left\langle n\left(\overrightarrow{\mathbf{R}}\left(t\right)\right)\right|\frac{d}{dt}\left|n\left(\overrightarrow{\mathbf{R}}\left(t\right)\right)\right\rangle \\
\theta\left(t\right) &= \frac{1}{\hbar}\int_0^t dt' E_n\left(\overrightarrow{\mathbf{R}}\left(t'\right)\right) - i\int_0^{t'}\left\langle n\left(\overrightarrow{\mathbf{R}}\left(t'\right)\right)\right|\frac{d}{dt'}\left|n\left(\overrightarrow{\mathbf{R}}\left(t'\right)\right)\right\rangle
\end{aligned}. \tag{A.4}$$

From this we extract that the phase must obey

$$\theta\left(t\right) = \frac{1}{\hbar}\int_0^t dt' E_n\left(\overrightarrow{\mathbf{R}}\left(t'\right)\right) - i\int_0^t\left\langle n\left(\overrightarrow{\mathbf{R}}\left(t'\right)\right)\right|\frac{d}{dt'}\left|n\left(\overrightarrow{\mathbf{R}}\left(t'\right)\right)\right\rangle. \tag{A.5}$$

We define $\gamma_n \equiv i\int_0^t dt'\left\langle n\left(\overrightarrow{\mathbf{R}}\left(t'\right)\right)\right|\frac{d}{dt'}\left|n\left(\overrightarrow{\mathbf{R}}\left(t'\right)\right)\right\rangle$ as the Berry phase. We can further rewrite it as

$$\gamma_n = i \int_{\mathcal{C}} \left\langle n\left(\overrightarrow{\mathbf{R}}\right)\right| \nabla_{\overrightarrow{\mathbf{R}}} \left|n\left(\overrightarrow{\mathbf{R}}\right)\right\rangle \cdot d\overrightarrow{\mathbf{R}}, \tag{A.6}$$

where now we have an integral over the space of parameters $\left\{\overrightarrow{\mathbf{R}}\right\}$ over the circuit $\mathcal{C}$. We define $\overrightarrow{\mathcal{A}}_n\left(\overrightarrow{\mathbf{R}}\right) = i\left\langle n\left(\overrightarrow{\mathbf{R}}\right)\right| \nabla_{\overrightarrow{\mathbf{R}}} \left|n\left(\overrightarrow{\mathbf{R}}\right)\right\rangle$, the Berry connection. Now, the states of our system can be defined up to a multiplicative phase. This means that a state

$$\left|n'\left(\overrightarrow{\mathbf{R}}\left(t\right)\right)\right\rangle = e^{-i\alpha\left(\overrightarrow{\mathbf{R}}\right)} \left|n\left(\overrightarrow{\mathbf{R}}\left(t\right)\right)\right\rangle, \tag{A.7}$$

is equivalent to the state $\left|n\left(\overrightarrow{\mathbf{R}}\left(t\right)\right)\right\rangle$. We call this a gauge transformation. The introduction of this phase changes the Berry connection in the following way

$$\overrightarrow{\mathcal{A}}'_n\left(\overrightarrow{\mathbf{R}}\right) \to \overrightarrow{\mathcal{A}}_n\left(\overrightarrow{\mathbf{R}}\right) + \nabla_{\overrightarrow{\mathbf{R}}}\alpha\left(\overrightarrow{\mathbf{R}}\right). \tag{A.8}$$

In turn, the geometrical phase is altered by

$$\gamma'_n \to \gamma_n + \alpha\left(\overrightarrow{\mathbf{R}}\left(T\right)\right) - \alpha\left(\overrightarrow{\mathbf{R}}\left(0\right)\right). \tag{A.9}$$

The Berry connection $\overrightarrow{\mathcal{A}}_n\left(\overrightarrow{\mathbf{R}}\right)$ is a real quantity. If our eigenstates are normalized, then we have

$$\begin{aligned} \nabla \langle n \mid n\rangle &= 0 \\ \langle \nabla n \mid n\rangle + \langle n \mid \nabla n\rangle &= 0 \\ \langle n \mid \nabla n\rangle &= -\langle \nabla n \mid n\rangle \\ \langle n \mid \nabla n\rangle &= -\langle n \mid \nabla n\rangle^* \end{aligned}$$

Implying that $\langle n \mid \nabla n\rangle$ is purely imaginary and that $i\langle n \mid \nabla n\rangle$ is real.

B. Localization

If we consider an initial state localized at site j, $\Psi\left(t=0,j\right)=\frac{1}{L^d}\sum_{\overrightarrow{\mathbf{k}}}e^{i\overrightarrow{\mathbf{k}}\cdot\overrightarrow{\mathbf{r}}_j}$,from Schrödinger's equation, our state at time t can be written as

$$\Psi\left(t,j\right)=\frac{1}{L^d}\sum_{\overrightarrow{\mathbf{k}}}e^{i\overrightarrow{\mathbf{k}}\cdot\overrightarrow{\mathbf{r}}_j-2it\nu\sum_{i=1}^{d}\cos(k_i)}. \tag{B.1}$$

In the thermodynamic limit we can turn the summation into an integration in $\overrightarrow{\mathbf{k}}$-space. We then obtain:

$$\begin{aligned}
\Psi\left(t,j\right)&=\int_{[0,2\pi]^d}d\overrightarrow{\mathbf{k}}\,e^{i\overrightarrow{\mathbf{k}}\cdot\overrightarrow{\mathbf{r}}_j-2it\nu\sum_{i=1}^{d}\cos(k_i)}\\
\Psi\left(t,j\right)&=\prod_{l=1}^{d}\int_0^{2\pi}dk_l e^{ik_l\cdot r_l^{(j)}-2it\nu\cos(k_l)}\\
\Psi\left(t,j\right)&=\prod_{l=1}^{d}\int_0^{2\pi}dk_l e^{i(k_l+\pi/2)r_l^{(j)}+2it\nu\sin(k_l)}\\
\Psi\left(t,j\right)&=\prod_{l=1}^{d}i^{r_l^{(j)}}J_{r_l^{(j)}}\left(-2t\nu\right)
\end{aligned}. \tag{B.2}$$

Using the expansion for large argument of the Bessel function

$$J_n\left(x\right)\approx\sqrt{\frac{2}{\pi x}}\cos\left(x-\frac{\pi}{4}-\frac{n\pi}{2}\right)\quad|x|\gg1, \tag{B.3}$$

we can write

$$\left|\Psi\left(t,j\right)\right|^2\approx\frac{1}{\pi\nu}\left|\prod_{l=1}^{d}t^{-1/2}\cos\left(-2t\nu-\frac{\pi}{4}-\frac{r_l^{(j)}\pi}{2}\right)\right|\sim\left|\prod_{l=1}^{d}t^{-1/2}\right|=t^{-d} \tag{B.4}$$

C. Two-band Hamiltonian

C.1. Eigenstates and eigenvalues

We consider a two-band Hamiltonian that can be written as $H = \sum_{\overrightarrow{\mathbf{k}}} c^{\dagger}_{\overrightarrow{\mathbf{k}}} \overrightarrow{\mathbf{h}} \cdot \overrightarrow{\sigma} c_{\overrightarrow{\mathbf{k}}}$, where $\overrightarrow{\sigma} = (\sigma_x, \sigma_y, \sigma_z)$, $\overrightarrow{\mathbf{h}}\left(\overrightarrow{\mathbf{k}}\right) = \left(h_x\left(\overrightarrow{\mathbf{k}}\right), h_y\left(\overrightarrow{\mathbf{k}}\right), h_z\left(\overrightarrow{\mathbf{k}}\right)\right)$ and $c_{\overrightarrow{\mathbf{k}}}$ is a spinor. This Hamiltonian is diagonalizable by blocks where each block is assigned a wave-vector $\overrightarrow{\mathbf{k}}$. The explicit expression for each block is:

$$\overrightarrow{\mathbf{h}}\left(\overrightarrow{\mathbf{k}}\right) \cdot \overrightarrow{\sigma} = \begin{pmatrix} h_z\left(\overrightarrow{\mathbf{k}}\right) & h_x\left(\overrightarrow{\mathbf{k}}\right) - ih_y\left(\overrightarrow{\mathbf{k}}\right) \\ h_x\left(\overrightarrow{\mathbf{k}}\right) + ih_y\left(\overrightarrow{\mathbf{k}}\right) & -h_z\left(\overrightarrow{\mathbf{k}}\right) \end{pmatrix} \tag{C.1}$$

Assuming that $\left|\psi_{\overrightarrow{\mathbf{k}}}\right\rangle$ is an eigenvector of this matrix, then we can write $\overrightarrow{\mathbf{h}}\left(\overrightarrow{\mathbf{k}}\right) \cdot \overrightarrow{\sigma} \left|\psi_{\overrightarrow{\mathbf{k}}}\right\rangle = E_{\overrightarrow{\mathbf{k}}} \left|\psi_{\overrightarrow{\mathbf{k}}}\right\rangle$. It is also clear that

$$\begin{aligned} \left\langle\psi_{\overrightarrow{\mathbf{k}}}\right| \left(\overrightarrow{\mathbf{h}}\left(\overrightarrow{\mathbf{k}}\right) \cdot \overrightarrow{\sigma}\right)^{\dagger} \left(\overrightarrow{\mathbf{h}}\left(\overrightarrow{\mathbf{k}}\right) \cdot \overrightarrow{\sigma}\right) \left|\psi_{\overrightarrow{\mathbf{k}}}\right\rangle &= \left|E_{\overrightarrow{\mathbf{k}}}\right|^2 \\ \left\langle\psi_{\overrightarrow{\mathbf{k}}}\right| \left|\overrightarrow{\mathbf{h}}\left(\overrightarrow{\mathbf{k}}\right) \cdot \overrightarrow{\sigma}\right|^2 \left|\psi_{\overrightarrow{\mathbf{k}}}\right\rangle &= \left|E_{\overrightarrow{\mathbf{k}}}\right|^2, \\ \left|\overrightarrow{\mathbf{h}}\left(\overrightarrow{\mathbf{k}}\right)\right|^2 \left\langle\psi_{\overrightarrow{\mathbf{k}}}\right| |\overrightarrow{\sigma}|^2 \left|\psi_{\overrightarrow{\mathbf{k}}}\right\rangle &= \left|E_{\overrightarrow{\mathbf{k}}}\right|^2 \end{aligned} \tag{C.2}$$

however, $|\overrightarrow{\sigma}|^2 \left|\psi_{\overrightarrow{\mathbf{k}}}\right\rangle = 1$ since the eigenvectors of the Pauli matrices are 1 and -1. Therefore, the eigenvalues of each block are $E^{\pm}_{\overrightarrow{\mathbf{k}}} = \pm \left|\overrightarrow{\mathbf{h}}\left(\overrightarrow{\mathbf{k}}\right)\right|$.

We can now find the the eigenvectors by solving the matrix equation

$$\begin{pmatrix} h_z\left(\overrightarrow{\mathbf{k}}\right) & h_x\left(\overrightarrow{\mathbf{k}}\right) - ih_y\left(\overrightarrow{\mathbf{k}}\right) \\ h_x\left(\overrightarrow{\mathbf{k}}\right) + ih_y\left(\overrightarrow{\mathbf{k}}\right) & -h_z\left(\overrightarrow{\mathbf{k}}\right) \end{pmatrix} \begin{pmatrix} \psi^{\pm}_A\left(\overrightarrow{\mathbf{k}}\right) \\ \psi^{\pm}_B\left(\overrightarrow{\mathbf{k}}\right) \end{pmatrix} = \pm \left|\overrightarrow{\mathbf{h}}\left(\overrightarrow{\mathbf{k}}\right)\right| \begin{pmatrix} \psi^{\pm}_A\left(\overrightarrow{\mathbf{k}}\right) \\ \psi^{\pm}_B\left(\overrightarrow{\mathbf{k}}\right) \end{pmatrix}. \tag{C.3}$$

For the lower band (-) we find

$$\psi^{-}_A\left(\overrightarrow{\mathbf{k}}\right) = -\frac{h_x - ih_y}{h_z + \left|\overrightarrow{\mathbf{h}}\right|} \psi^{-}_B\left(\overrightarrow{\mathbf{k}}\right). \tag{C.4}$$

Imposing normalization yields

$$\left|\psi^{-}_{\overrightarrow{\mathbf{k}}}\right\rangle = \frac{1}{\sqrt{2\left|\overrightarrow{\mathbf{h}}\right|\left(\left|\overrightarrow{\mathbf{h}}\right| - h_z\right)}} \begin{pmatrix} h_z - \left|\overrightarrow{\mathbf{h}}\right| \\ h_x + ih_y \end{pmatrix}. \tag{C.5}$$

We do the same for the upper band (+) and obtain

$$\left|\psi^{+}_{\overrightarrow{\mathbf{k}}}\right\rangle = \frac{1}{\sqrt{2\left|\overrightarrow{\mathbf{h}}\right|\left(\left|\overrightarrow{\mathbf{h}}\right| - h_z\right)}} \begin{pmatrix} h_z + \left|\overrightarrow{\mathbf{h}}\right| \\ h_x + ih_y \end{pmatrix}. \tag{C.6}$$

Alternatively, we could write our vector $\overrightarrow{\mathbf{h}}$ in spherical coordinates as $\overrightarrow{\mathbf{h}} = (h, \theta, \phi)$ making the transformations [5]

$$\begin{aligned} h &= h_x^2 + h_y^2 + h_z^2 \\ \theta &= \arctan\left(\frac{h_y}{h_x}\right). \\ \phi &= \arccos\left(\frac{h_z}{h}\right) \end{aligned} \tag{C.7}$$

The new Hamiltonian becomes

$$\overrightarrow{\mathbf{h}} \cdot \overrightarrow{\sigma} = h \begin{pmatrix} \cos(\phi) & \sin(\phi)\, e^{-i\theta} \\ \sin(\phi)\, e^{i\theta} & -\cos(\phi) \end{pmatrix}. \tag{C.8}$$

We can now calculate the wavefunctions in these new coordinates and, using a few trigonometric relations, obtain

$$\left|\psi^{-}\right\rangle = \begin{pmatrix} \sin(\phi/2) \\ -e^{i\theta}\cos(\phi/2) \end{pmatrix} \quad \left|\psi^{+}\right\rangle = \begin{pmatrix} \cos(\phi/2) \\ e^{i\theta}\sin(\phi/2) \end{pmatrix}. \tag{C.9}$$

C.2. Berry connection

The Berry connection for the lower band can be written as $\overrightarrow{\mathcal{A}}^{-} = i\left\langle\psi^{-}\right| \nabla_{\overrightarrow{\mathbf{R}}} \left|\psi^{-}\right\rangle$. It is convenient to use the wavefunctions written as C.9 and plug them into the expression for $\overrightarrow{\mathcal{A}}$

$$\begin{aligned} \overrightarrow{\mathcal{A}}^{-} &= i \begin{pmatrix} \sin(\phi/2) & -e^{-i\theta}\cos(\phi/2) \end{pmatrix} \nabla_{R_\mu} \begin{pmatrix} \sin(\phi/2) \\ -e^{i\theta}\cos(\phi/2) \end{pmatrix} \\ &= i \begin{pmatrix} \sin(\phi/2) & -e^{-i\theta}\cos(\phi/2) \end{pmatrix} \begin{pmatrix} \frac{1}{2}\cos(\phi/2)\,\partial_{R_\mu}\phi \\ \frac{1}{2}\sin(\phi/2)\, e^{i\theta}\partial_{R_\mu}\phi - i\cos(\phi/2)\,\partial_{R_\mu}\theta \end{pmatrix} \\ &= -\cos^2(\phi/2)\,\partial_{R_\mu}\theta \end{aligned} \tag{C.10}$$

The space of parameters upon which depends our state $|\psi\rangle$ is the space of $\overrightarrow{\mathbf{h}}$. Using the

formula for the gradient in spherical coordinates, we obtain a single non-vanishing component of the Berry connection, which is given by

$$\begin{aligned}\overrightarrow{\mathcal{A}} &= -\frac{\cos^2(\phi/2)}{h\sin(\phi)}\hat{\theta} \\ \overrightarrow{\mathcal{A}} &= -\frac{1}{2h}\frac{1+\cos(\phi)}{\sin(\phi)}\hat{\theta}. \\ \overrightarrow{\mathcal{A}} &= -\frac{1}{2h}\cot(\phi/2)\,\hat{\theta}\end{aligned} \tag{C.11}$$

The Berry phase will now be given by $\overrightarrow{\mathbf{\Omega}} = \nabla_{\overrightarrow{\mathbf{h}}} \times \overrightarrow{\mathcal{A}}$, hence

$$\begin{aligned}\overrightarrow{\mathbf{\Omega}} &= \frac{1}{h\sin(\phi)}\frac{\partial}{\partial\phi}\left(-\frac{1}{2h}\cot(\phi/2)\sin(\phi)\right)\hat{h} \\ \overrightarrow{\mathbf{\Omega}} &= -\frac{1}{2h^2}\frac{1}{\sin(\phi)}\frac{\partial}{\partial\phi}(1+\cos(\phi))\,\hat{h} \\ \overrightarrow{\mathbf{\Omega}} &= \frac{1}{2h^2}\hat{h}\end{aligned} \quad . \tag{C.12}$$

Using 1.6 we can express the Berry phase as

$$\begin{aligned}\gamma &= \int_{\text{h-space}} \overrightarrow{\mathbf{\Omega}} \cdot \overrightarrow{\mathbf{dS}} \\ \gamma &= \int_{\text{h-space}} \frac{\overrightarrow{\mathbf{h}}}{2h^3} \cdot \overrightarrow{\mathbf{dS}} \\ \gamma &= \frac{1}{2}\int \frac{h^2\sin(\phi)}{h^3}\overrightarrow{\mathbf{h}} \cdot \hat{\mathbf{h}} d\phi d\theta \\ \gamma &= \frac{1}{2}\int d\phi d\theta \sin(\phi)\end{aligned} \quad , \tag{C.13}$$

where we chose to calculate the flux through the surface of constant h. This integral can be written as

$$\frac{1}{2}\int d\phi d\theta \sin(\phi) = \frac{1}{2}\int d\phi d\theta \frac{\partial\hat{\mathbf{h}}}{\partial\phi} \times \frac{\partial\hat{\mathbf{h}}}{\partial\theta} \cdot \hat{\mathbf{h}} \tag{C.14}$$

C.3. Chern number for the Haldane model

We showed in 2.1 that the Cher number for the Haldane model could be written as

$$C = -\frac{1}{2\pi}\int_{\partial S} \nabla_{\overrightarrow{\mathbf{q}}}\theta(\overrightarrow{\mathbf{q}}) \cdot d\overrightarrow{\mathbf{q}}, \tag{C.15}$$

with $e^{i\theta(\overrightarrow{\mathbf{q}})} = \frac{\hbar v_F(m+\Sigma_\nu+|h_\nu|)|(\nu q_x - iq_y)|}{|m+\Sigma_\nu+|h_\nu||\hbar v_F(\nu q_x - iq_y)}$. This expression can be simplified to

$$e^{i\theta(\overrightarrow{\mathbf{q}})} = \frac{|(\nu q_x - iq_y)|}{\nu q_x - iq_y} = -\frac{|\overrightarrow{\mathbf{q}}e^{-i\nu\varphi}|}{|\overrightarrow{\mathbf{q}}|\,e^{-i\nu\varphi}} = -e^{i\nu\varphi}. \tag{C.16}$$

By insert this expression into 2.19 and considering ∂S a small circle of radius q around the K point, we obtain

$$C = -\frac{1}{2\pi}\int_0^{2\pi} q d\varphi \left(-\frac{1}{q}\partial_\varphi \varphi\right) = 1. \tag{C.17}$$

D. KPM

D.1. Chebyshev polynomials

The Chebyshev polynomials of the first kind are defined in the following way

$$T_n(x) = \cos(n \arccos(x)), \tag{D.1}$$

and are therefore only defined in the domain $]-1,1[$.

The first polynomials can be calculated by using a few trigonometric identities:

$$\begin{aligned} T_0(x) &= 1 \\ T_1(x) &= x \\ T_2(x) &= 2x^2 - 1 \\ &\vdots \end{aligned} \tag{D.2}$$

From

$$\begin{aligned} &T_{n-1}(\cos(\theta)) + T_{n+1}(\cos(\theta)) = \cos((n-1)\theta) + \cos((n+1)\theta) \\ &T_{n-1}(\cos(\theta)) + T_{n+1}(\cos(\theta)) = \cos(n\theta)\cos(\theta) + \sin(n\theta)\sin(\theta) + \cos(n\theta)\cos(\theta) - \sin(n\theta)\sin(\theta) \\ &T_{n-1}(\cos(\theta)) + T_{n+1}(\cos(\theta)) = 2\cos(n\theta)\cos(\theta) \\ &T_{n-1}(\cos(\theta)) + T_{n+1}(\cos(\theta)) = 2T_n(\cos(\theta))\cos(\theta) \end{aligned}, \tag{D.3}$$

we obtain the recurrence relation

$$T_{n+1}(x) = 2xT_n(x) - T_{n-1}(x). \tag{D.4}$$

D.2. Coefficients of DoS

From the orthogonality relation of the cosine function

$$\int_0^\pi d\theta \cos(n\theta)\cos(m\theta) = \frac{\pi}{2}\delta_{nm}(1 + \delta_{n,0}), \tag{D.5}$$

we obtain for the Chebyshev polynomials

$$\begin{aligned} & \frac{2}{\pi}\int_{-1}^{1}\frac{dx}{\sqrt{1-x^2}}T_n(x)\,T_m(x)\,dx \\ \iff & \frac{2}{\pi}\int_{-1}^{1}\frac{dx}{\sqrt{1-x^2}}\cos\left(m\arccos(x)\right)dx \\ \iff & \frac{2}{\pi}\int_{\pi}^{0}-du\cos\left(n\arccos(x)\right)\cos\left(m\arccos(x)\right)dx \\ \iff & \frac{2}{\pi}\int_{0}^{\pi}du\cos\left(n\arccos(x)\right)\cos\left(m\arccos(x)\right)dx \\ \iff & \delta_{nm}\left(1+\delta_{n,0}\right) \end{aligned} \tag{D.6}$$

This orthogonality relation is what allows us expand the Dirac delta function as:

$$\delta(x-\varepsilon)=\sum_{n=0}^{\infty}a_n(\varepsilon)\,T_n(x)\,. \tag{D.7}$$

Since we can write the coefficients as

$$\frac{2}{\pi}\int_{-1}^{1}\frac{dx}{\sqrt{1-x^2}}T_n(x)\,\delta(x-\varepsilon)=\sum_{m=0}^{\infty}\frac{2}{\pi}\int_{-1}^{1}\frac{dx}{\sqrt{1-x^2}}T_n(x)\,a_m(\varepsilon)\,T_m(x)=a_n(\varepsilon)\left(1+\delta_{n,0}\right)\quad, \tag{D.8}$$

and so

$$a_n(\varepsilon)=\frac{2}{\pi}\int_{-1}^{1}\frac{dx}{\sqrt{1-x^2}}T_n(x)\,\delta(x-\varepsilon)=\frac{2}{\left(1+\delta_{n,0}\right)\pi}\frac{T_n(\varepsilon)}{\sqrt{1-\varepsilon^2}}. \tag{D.9}$$

Combining this result with equation D.7 we obtain the following expansion of the Dirac delta function in terms of Chebyshev polynomials:

$$\begin{aligned} \delta(x-\varepsilon) &= \sum_{n=0}^{\infty}a_n(\varepsilon)\,T_n(x) \\ \delta(x-\varepsilon) &= \frac{2}{\pi\sqrt{1-\varepsilon^2}}\sum_{n=0}^{\infty}\frac{T_n(\varepsilon)}{\left(1+\delta_{n,0}\right)}T_n(x) \end{aligned}\quad. \tag{D.10}$$